Doctoral Dissertation (Shinshu University)

Novel reconstruction algorithms for metal artifact reduction in X-ray CT imaging

March 2016

Department of Bioscience and Textile Technology
Interdisciplinary Graduate School of Science and Technology

Toru Kano

Table of contents

Chapter 1

Introduction

Chapter 1: Introduction

1.1 Background

In 1972, Godfrey Hounsfield developed a technology called X-ray Computed tomography (X-ray CT) [1], that is based on a theory propounded by Allan MacLeod Cormack [2][3]. X-ray CT can generate cross-sectional images of an object, and it is said that this technology is the most important invention since 1895 when Wilhelm Conrad Röntgen found X-ray [4].

X-ray CT has spread rapidly in the field of diagnosis and industry, and brought significant benefits to us, however, many technical challenges such as a wide variety of artifacts remain. Artifacts are caused by imperfections of apparatus or human factors, and they deteriorate CT images. The artifacts include metal artifacts caused by metals, motion artifacts caused by movements of subjects, and truncation artifacts caused by limits of projection ranges. Particularly, the metal artifact have become one of the biggest problems in X-ray CT imaging. When metal objects are included in a cross-section, they make strong radial noises around their own, and make shadows between metals. Unfortunately, nowadays there are a large variety of cases of metal artifact generation, such as patients with hip implants, artifical knee joints, dental fillings, bone screws, aneurysm coils, stents, pacemaker, and all other metallic products. Notably, surgical joint replacement of hips and knees is rapidly increasing. In the US, the number of hip replacement was 332,000, and knee replacement was 719,000 per year in 2015 [5], while the number was 225,900 and 431,485, respectively, in 2004 [6]. Furthermore, the demands for total hip and knee arthroplasties are projected to increase to 572,000 and 3.48 million, respectively, by 2030 [7].

As examples of metal artifact generation, a cross-sectional image of; a human head with metallic tooth implants is shown in Fig. 1.1(a), an electronic circuit with embedded metals is shown in Fig. 1.1(b). Since the metal regions and its peripheries are unclear, it is not possible to diagnose and inspect them accurately. If these metal artifacts can be reduced,

we can readily observe patient bodies with metallic implants, and inspect metallic products. Such a technology will pay us huge dividends. There have been many attempts to ameliorate this problem, but an optimal solution has yet to be found.

In this study, we propose novel metal artifact reduction algorithms to provide more superior diagnose/inspection techniques to medical/industrial fields.

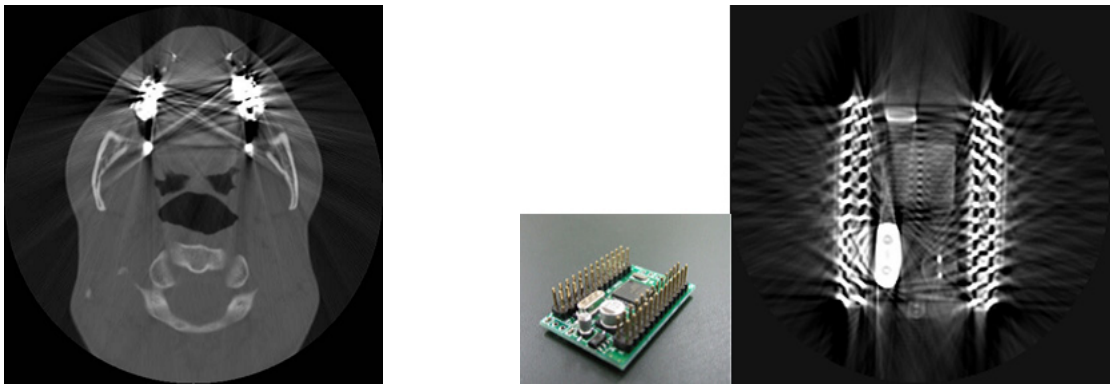

(a) (b)

Fig. 1.1 Examples of metal artifact generation; (a) a human head with metallic tooth implants, (b) an electronic circuit with embedded metals.

1.2 Survey of conventional researches

Existing researches related to metal artifact reduction are classified into hardware improvement or software improvements.

1.2.1 Hardware improvements

Hardware improvements to reduce metal artifacts include use of high energy radiations, use of monochromatic X-ray, and refinements of scans.

By using high energy radiations, metal artifacts will be drastically reduced. However, since high energy radiations are little absorbed by non-metals such as resins or living tissues, the contrast resolution of the reconstruction image is significantly reduced. Also, from a viewpoint of radiation exposure, it is not practical in medical fields.

If you could make a monochromatic X-ray, all metal artifacts will theoretically disappear. However, generating a monochromatic X-ray is accompanied by an extreme decrease in X-ray intensity, it is difficult to use for CT scanning. Enough monochromatic X-rays could be generated by using synchrotron radiation facility, but it is unrealistic in actual medical and industry fields [8].

As a way of refinements of scans, it has been considered how to place subjects. If you could place the subject while minimizing the distance that X-rays are passed through metals, metal artifacts would be reduced. For example, when scanning an integrated circuit, the general reconstruction result is shown in Fig. 1.2. We see that metal artifacts are generated, and the image is unclear. On the other hand, when you scanned it from an oblique direction, the X-ray path length of metal regions would decrease, and metal artifacts would also be reduced as shown in Fig. 1.3. Although this is an easy way to reduce metal artifact, there is a need for an environment that can be placed subjects freely, and such scans from an oblique direction reduce resolutions of images.

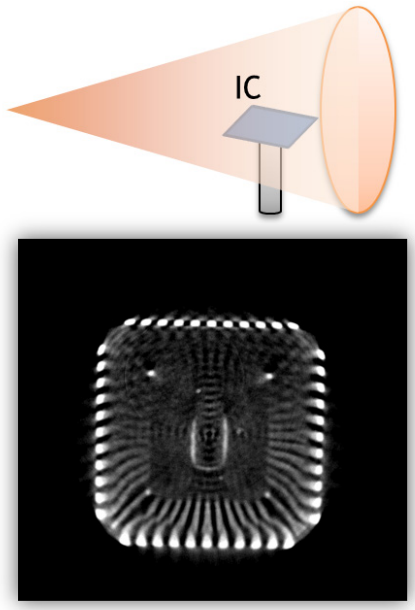

Fig. 1.2: Normal projection result.

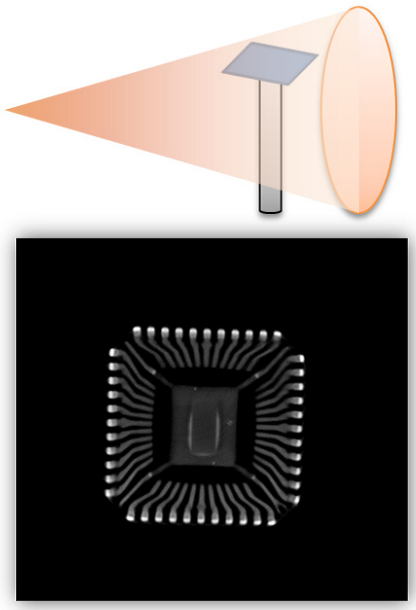

Fig. 1.3: Improved projection result.

1.2.2 Software improvements

Software improvements include an remediation of projection data or reconstruction algorithms. These methods have advantages that can readily apply to widespread X-ray CT, and are inexpensive.

One of the first software approach to reduce metal artifacts was proposed by W.A. Kalender et al [9]. This method is based on linear interpolations to metal regions on projection data. Zhao et al. applied a weighting using wavelet processing in the field of view [10], Zhang et al. modified metal regions by projection data from two directions [11], M. Yazdi et at. interpolated missing projections in raw CT data using unaffected projections [12], M. Abdoli et al. also corrected projection data using weighted virtual sonograms [13], and Koseki et al. applied interpolations to invalid portions on projection data [14]. Although other modifications to projection data have been performed, these are limited to application to simple shapes, or the effects of metal artifact reduction are insufficient.

As a CT imaging technique, we can also use iterative reconstruction instead of back projections that are widely used in CT (details are described in Chapter 2). Man et al. and Wang et al. tried to modify calculations in iterative reconstruction [15] [16]. However, metal

artifact reduction methods based on iterative reconstruction don't indicate sufficient results, and it requires a huge computation time compared to FBP. For these reasons, iterative reconstruction is not a common technique in CT.

Alvarez et al. noted that absorptions of X-rays by materials depend on the energy spectrum of the incident X-ray, and proposed a reconstruction algorithm based on projection data collected using two different energies [17]. This way is called Dual Energy (DE) methods, and many studies related to DE methods have been performed [18] [19]. DE methods have applied to various artifacts reduction, however, they requires hardware modifications. Furthermore, since DE methods require twice scans, there remain some problems about robustness and dosage.

1.3 The composition of this thesis

In Chapter 1, background, purpose of this study, and overview of existing researches were described.

In Chapter 2, principles of X-ray CT, reconstruction algorithms, and causes of metal artifacts are explained for understanding this study.

In Chapter 3, the simulation software that we developed is introduced. Then the validity of the simulation is confirmed by comparing actual CT data and simulation data.

In Chapter 4, we focused on shape characteristics of projection data, and proposed a metal artifact reduction based on the feature characteristics of sinograms composed of sine curves. The proposed method is applied to actual CT data and simulation data, then the performance is confirmed.

In Chapter 5, a novel metal artifact reduction method based on iterative reconstruction is proposed to solve a problem of the method mentioned in Chapter 4. The method is applied to CT data and simulation data while comparing to the method proposed in Chapter 4, and the superiority is evaluated.

In Chapter 6, our proposed algorithms are extended to three-dimensional one so as to widely disseminate our superior technology. By formulating three-dimensional reconstruction calculations, the theory of metal artifact reduction for cone beam data is established. Validation is performed using a three-dimensional numerical phantom, and the availability is demonstrated.

In Chapter 7, summary and future plans of this study are described.

Chapter 2

Principles of X-ray CT

Chapter 2: Principle of X-ray CT

In this chapter, principles of X-ray CT are described for understanding this study.

2.1 Physics of X-ray

2.1.1 Generation of X-ray

An X-ray is an electromagnetic wave due to electronic transitions, and the Energy of the X-ray E[keV] is given by:

$$E = \frac{hc}{\lambda} \approx \frac{12.398}{\lambda}, \tag{2.1}$$

where h is Plank's constant, c is the light speed, and λ is the wavelength of the X-ray. In order to generate X-rays and x-irradiate an object, an X-ray tube is built into the X-ray CT. The X-ray tube is an X-ray generator, that is typically composed of a filament, a target material, and a beryllium window. By applying a high voltage to the filament, thermal electrons are emitted at high speed, and by hitting the electrons against the target material, X-rays are generated. The beryllium window has a role of an X-ray takeoff port.

2.1.2 X-ray absorption

When irradiating X-rays to an object, a part of X-rays will be absorbed by the object, and other parts will pass through the object as transmission X-rays. All X-ray CT use the transmission X-rays in the reconstruction calculation, and for understanding the principles deeply, there is need to know the main factors of absorption, such as the photoelectric effect and X-ray scattering.

Photoelectric effect

The photoelectric effect is a phenomenon that electron in atoms are discharged as photoelectrons due to absorbed X-ray. The atoms, which discharged photoelectrons, become unstable

excited state. In order to stabilize, the atoms choose either one of two ways; generating of X-ray fluorescence or Auger electron. Generally, the higher the atomic number, the higher the rate of generating X-ray fluorescence.

X-ray scattering

X-rays that were not absorbed by photoelectric effect will be discharged as scattered rays. There are two types of X-ray scattering; Compton scattering and Rayleigh scattering. Compton scattering is the inelastic scattering caused by the absorption of the energy, and the wavelength is longer (the energy is smaller) than the incident X-ray. On the other hand, Rayleigh scattering is the elastic scattering, and the direction is changed while the wavelength (energy) is constant.

2.1.3 X-ray attenuation coefficients

The Beer-Lambert law describes the attenuation of X-rays passing through an object,

$$I = I_0 \exp(-\mu t), \tag{2.2}$$

where I_{in} and I_{out} are the incident and transmitted X-ray intensities, respectively, μ denotes

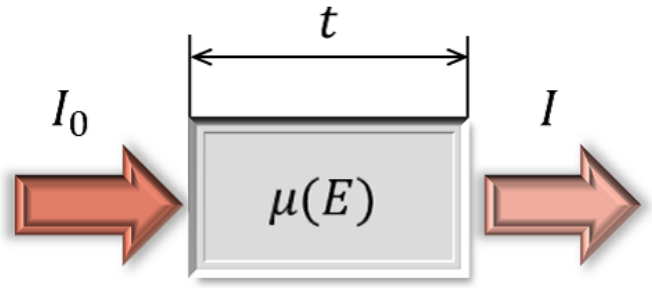

Fig. 2.1: X-ray absorption.

the material-specific X-ray attenuation coefficient, and t is the path length. The X-ray attenuation coefficient μ is the parameter, which indicates the strength of X-ray absorption, and is described as:

$$\mu = \mu_M \rho, \tag{2.3}$$

where μ_M is the X-ray mass absorption coefficient, and ρ is the density of the object. Since the mass absorption coefficient has the additive property, a mass absorption coefficient of an object is able to be calculated by summing values that mass absorption coefficients of each component element multiply their weight fraction.

$$\mu_M = \sum_i \mu_{M_i} w_i. \tag{2.4}$$

Mass absorption coefficients for each energy and each element are given in the literature [23].

From Eqn. (2.2) we define the projection data p, which is commonly used for reconstruction calculation in CT, as:

$$p = -\ln \frac{I}{I_0} = \mu t \tag{2.5}$$

We see that p is linear with respect to an object thickness t when the object is homogeneous (Note that this is only true for monochromatic X-rays). When the object is not homogeneous, the projection data p is able to be defined as:

$$p = -\ln \frac{I}{I_0} = \int_{-\infty}^{\infty} \mu(s) ds, \tag{2.6}$$

where $\mu(s)$ is X-ray attenuation coefficient at the position s. In order to calculate the X-ray attenuation coefficient at the position s, a large number of simultaneous equations are required. In reconstruction calculation of X-ray CT, X-ray attenuation coefficients at any positions are calculated by collecting projection data from many different directions, then gray scale colors are allocated depending on the attenuation coefficient values. That is, reconstruction images mean distributions of X-ray attenuation coefficients of the objects.

2.2 Image reconstruction

Image reconstruction algorithms are divided into two major classifications: back projection methods (analytical methods) and iterative reconstructions (algebraic methods). Both of these methods are able to boil down to solving huge linear simultaneous equations. In the followings, forward projection, back projection methods and iterative reconstructions are described in order.

2.3 Forward projection

At first in X-ray CT, X-rays are irradiated to an object from many different directions, and many projection data are collected. This operation is generally called forward projection (FP) or CT scans. The forward projection from one direction is defined as the following equation:

$$I_{\text{in}}(X,\theta) = I_{\text{out}} \exp\left(-\int_{-\infty}^{\infty} \mu(x,y)dY\right), \tag{2.7}$$

where $\mu(x,y)$ is a distribution of two dimensional X-ray attenuation coefficients, and X-Y coordinate system is obtained by rotating x-y coordinate system θ degrees. Also, because I_{in} is already known, projection data p is able to be expressed like the following:

$$p(X,\theta) = \int_{-\infty}^{\infty} \mu(x,y)dY. \tag{2.8}$$

Eqn. 2.8 denotes a line integration form along Y-axis, and this transformation is referred to as the Radon transform.

The forward projection calculation is illustrated in the following using a simple model. Fig. 2.2 is a virtual cross sectional image that has an object in center of it. Such virtual cross sectional images are called numerical phantoms. One parallel beam from one direction is equivalent to integrating the linear pixel values along the beam. In this numerical phantom, we see that rows of projection data from any directions are the same as shown in Fig. 2.2.

2.4 Back projection

In this section, back projection methods, that are the most commonly used for CT, are described.

2.4.1 Simple back projection

Simple back projection (SBP) is an operation of adding projection data collected by forward projection to an empty image in a linear fashion on computers. If there are projection data for a half rotation, $\mu_{\text{SBP}}(x,y)$, which is a reconstruction image created by simple back

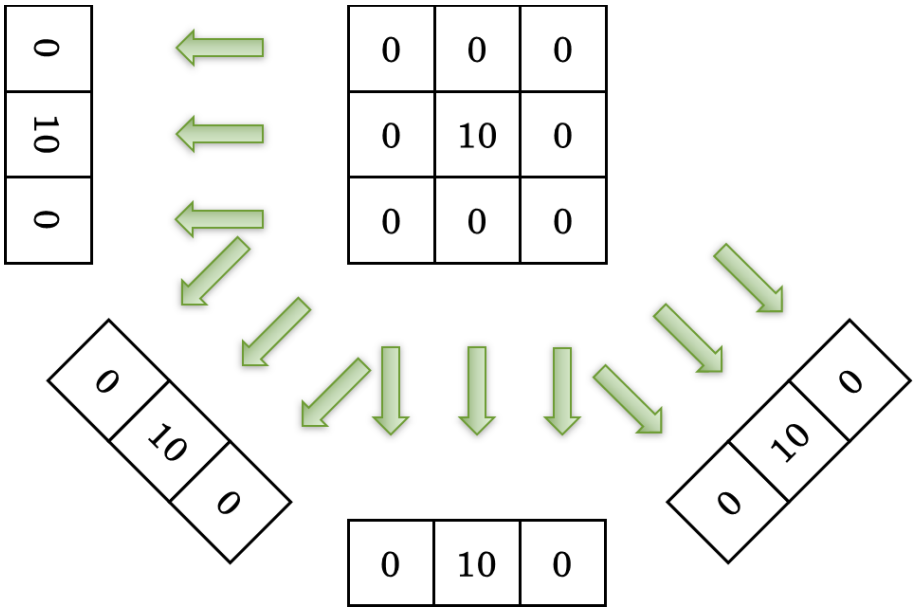

Fig. 2.2: Forward projection calculation.

projection, is defined as the following integral equation:

$$\mu_{\mathrm{SBP}}(x, y) = \frac{1}{\pi} \int_0^{\pi} p(X, \theta) d\theta. \tag{2.9}$$

This equation means that a pixel value at the point (x, y) is obtained by adding beam values that through the point from all directions. Tracking back the forward projection process, that is, adding the projection data to an empty image along projection directions, is the simple back projection. This operation is illustrated in Fig. 2.3, assuming to apply to the projection data of Fig. 2.2. Here, the projection data obtained by forward projection is firstly divided by the number of projection directions, then simple back projection is performed to an empty image on computers.

As shown in Fig. 2.3, projection data are added to all pixels that the beam passes. However, this result shows that the pixels, which was originally zero, became 2.5. In fact, it's known that simple back projection makes blurred reconstruction images as seen above.

It was illustrated by using the 3×3 pixels numerical phantom, but consider the cases that the image resolution is higher, and the number of projection directions is larger than this. In such cases, projection data like delta functions draw spoke-shaped data on the reconstruction image for each direction (Fig. 2.4). The density of this spokes is inversely proportional to

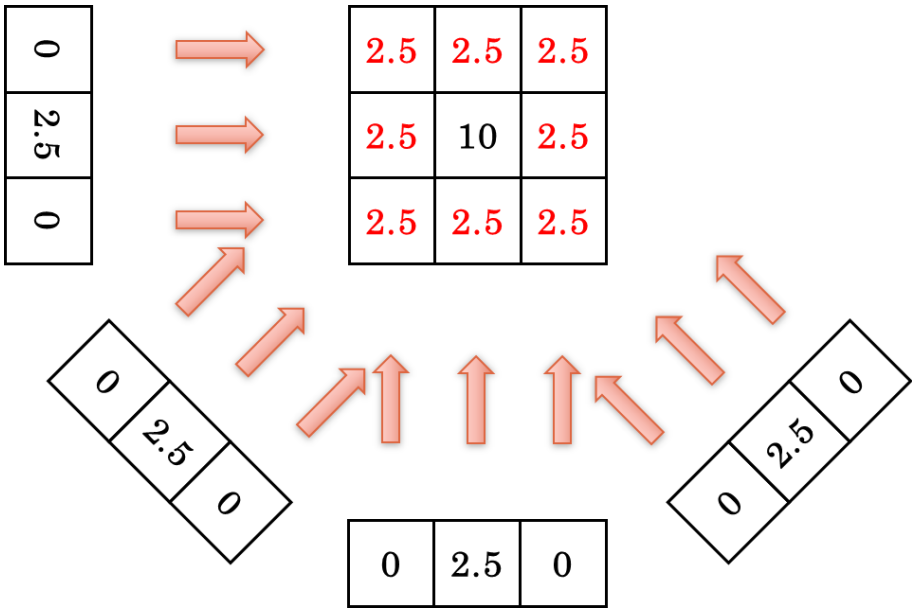

Fig. 2.3: Simple back projection.

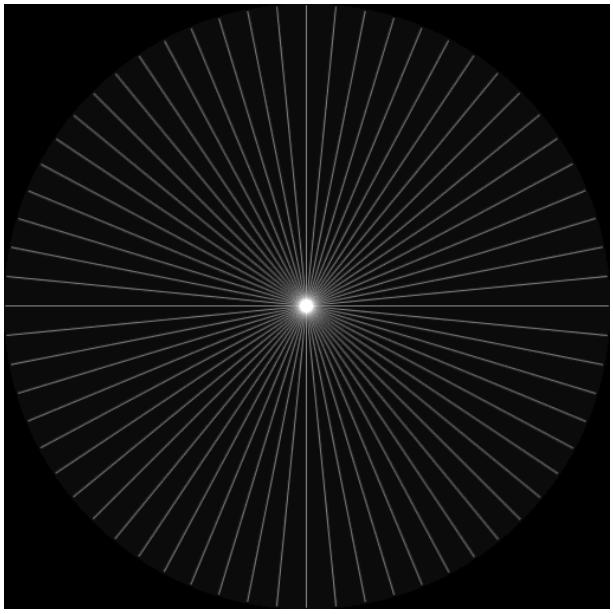

Fig. 2.4: The simple back projection result for one pixel data.

the distance from the point of the center, and the continuous change in the density makes blurred reconstruction images. The mathematical behavior of this blurring actually is able to be calculated, so it is also able to eliminate it. The methods are described below.

2.4.2 Convolution back projection

Convolution back projection is a method of applying an operation, which corresponds to corrections for blurring caused by back projection, to projection data in advance. To be more specific, by convolving projection data and a correction function h, corrected projection data $\hat{p}$ are generated and they are used for back projection.

$$\hat{p}(r,\theta) = p(r,\theta) * h(r) = \int_{-\infty}^{\infty} h(r-r')p(r',\theta)dt\prime \tag{2.10}$$

The correction function h is called convolution function, and the basic shape is something like the following: the center indicates positive value like a delta function, the others indicate negative values and approach asymptotically to zero, and the integral value of the waveform is zero. This is a functional form of a deconvolution that can correct extended blurs. As actual examples, the convolution function proposed by Ramachandran and Lakshminaraynan is shown in Eqn.2.11 and the function proposed by Shepp and Logan is shown in Eqn.2.12.

$$h(r) = h(n\cdot\Delta r) = \begin{cases} -\dfrac{1}{2}\dfrac{1}{\pi^2\cdot\Delta r^2\cdot n^2} & (n=\text{odd}) \\ 0 & (n=\text{even}) \end{cases} \tag{2.11}$$

$$h(r) = h(n\cdot\Delta r) = -\frac{4}{\pi}\frac{1}{\Delta r^2}\frac{1}{4n^2-1} \tag{2.12}$$

The convolution back projection result by using the convolution function Eqn.2.12 to the projection data of Fig. 2.2 is shown in Fig. 2.5. We see that the projection data became pointed shapes by convoluting, and the back projection result shows the ideal image whose edges are emphasized. This is because the blurs caused by back projection and the pointed shape caused by convolution cancel out each other.

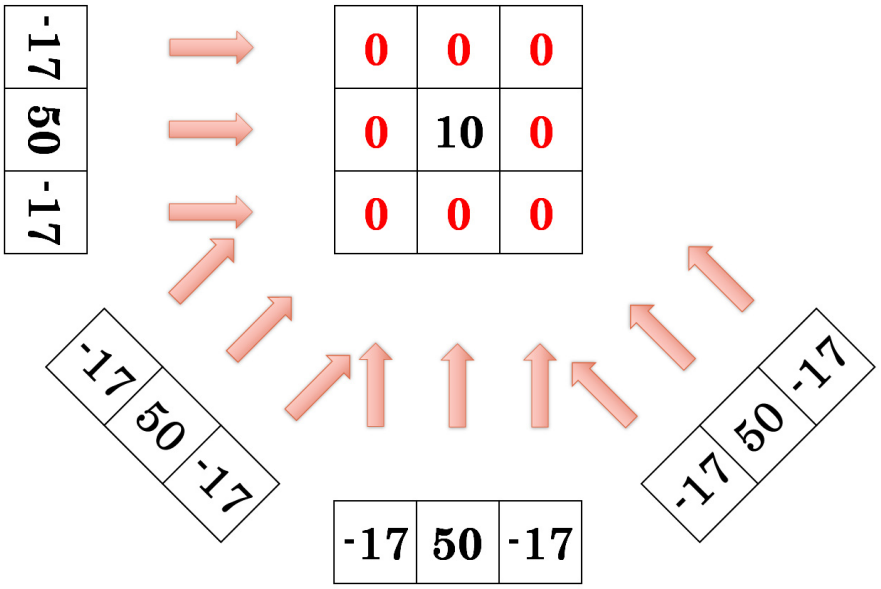

Fig. 2.5: Convolution back projection.

2.4.3 Two-dimensional Fourier transform method

Consider the relationship between projection data in a real space and projection data in a frequency space. When X-Y coordinate system is defined as x-y coordinate system rotated θ degrees, the detector become parallel to the X axis, and projection data $p(X, \theta)$ is expressed as follows:

$$\begin{aligned} p(X,\theta) &= \int_{-\infty}^{\infty} \mu(x,y)ds \\ &= \int_{-\infty}^{\infty} \mu(X\cos\theta - Y\sin\theta, X\sin\theta + Y\cos\theta)dY. \end{aligned} \tag{2.13}$$

Also, when $M(\xi, \eta)$ is defined as two dimensional Fourier transform of X-ray attenuation coefficients $\mu(x, y)$, the relationship can be written as:

$$M(\xi,\eta) = \int_{-\infty}^{\infty}\int_{-\infty}^{\infty} \mu(x,y)e^{-i(\xi x+\eta y)}dxdy \tag{2.14}$$

$$\mu(x,y) = \frac{1}{4\pi^2}\int_{-\infty}^{\infty}\int_{-\infty}^{\infty} M(\xi,\eta)e^{i(\xi x+\eta y)}d\xi d\eta. \tag{2.15}$$

Then, consider the conversion from Cartesian (x, y) to polar coordinates (R, θ) by using the following equations:

$$\begin{aligned} \xi &= R\cos\theta \\ \eta &= R\sin\theta. \end{aligned} \tag{2.16}$$

When these equations substitute to Eqn.2.14, it can be convert to the following:

$$\begin{aligned} M(\xi,\eta) &= M(R\cos\theta, R\sin\theta) \\ &= \int_{-\infty}^{\infty}\int_{-\infty}^{\infty}\mu(x,y)e^{-iR(x\cos\theta+y\sin\theta)}dxdy \\ &= \int_{-\infty}^{\infty}\int_{-\infty}^{\infty}\mu(x,y)e^{-iRX}dXdY \\ &= \int_{-\infty}^{\infty}\left[\int_{-\infty}^{\infty}\mu(x,y)dY\right]e^{-iRX}dX \\ &= \int_{-\infty}^{\infty}p(X,\theta)e^{-iRX}dX \end{aligned} \tag{2.17}$$

Eqn.2.17 represents that a one-dimensional Fourier transform of projection data $p(X, \theta)$ corresponds to a line with a slope θ passing through the center of a two-dimensional Fourier plane $M(\xi, \eta)$, and this property is known as the projection-slice theorem. Also, by collecting one-dimensional Fourier transforms of projection data from many different directions, a two-dimensional Fourier plane $M(\xi, \eta)$ is able to be filled. By applying two-dimensional Fourier inverse transform to $M(\xi, \eta)$, a X-ray attenuation coefficients distribution can be generated, and the relationship is expressed as the following:

$$\begin{aligned} \mu(x,y) &= \int_0^{\pi}\mathcal{F}^{-1}\left[M(\xi,\eta)\right]d\theta \\ &= \int_0^{\pi}\mathcal{F}^{-1}\left[\mathcal{F}[p(X,\theta)]\right]d\theta. \end{aligned} \tag{2.18}$$

This simple and beautiful way is called the two-dimensional Fourier transform method.

2.4.4 Filtered back projection

In the two-dimensional Fourier translation, one-dimensional Fourier transforms of projection data $p(X, \theta)$ will be arranged on a two-dimensional Fourier plane $M(\xi, \eta)$, but the density of the arranged lines won't be constant. In fact, the density is inversely proportional to the distance R from the center on the two-dimensional Fourier plane, and it will be maximized at the center. In order to reconstruct accurate images, it's necessary to consider the density difference between the high frequency region and the low frequency region on the two-dimensional Fourier plane. Otherwise, the reconstruction image will be a blurred one just like a simple back projection result.

The most common method to solve this problem is to use a filter to a one-dimensional Fourier transform of projection data. The filter is defined as a filter function $H(R)$, which is depending on the distance R from the center on the two-dimensional Fourier plane. The filter function can emphasize high frequency regions of a two-dimensional Fourier plane, and balance densities of high frequency and low frequency. Such reconstruction methods that use a filter function are called filtered back projection (FBP), and the equation is expressed as the following:

$$\mu(x, y) = \int_0^{\pi} \mathcal{F}^{-1} \left[\mathcal{F}[p(X, \theta) \times H(R)] \right] d\theta. \tag{2.19}$$

For filtered back projection, various filter functions $H(R)$ have been proposed. R-L filter function proposed by Ramachandran and Lakshminaraynan is defined as:

$$H(R) = \begin{cases} |R| & |R| \leq W \\ 0 & |R| > W, \end{cases} \tag{2.20}$$

where W means a maximum sampling frequency. In a low frequency region, a weighting proportional to a distance from a center is needed to reduce huge blurs. On the other hand, in a high frequency region, sharp images or low noise images are able to be reconstructed by changing a behavior of a filter function in a high frequency region. S-L filter function

proposed by Shepp and Logan is defined as:

$$H(R) = \begin{cases} \dfrac{2W}{\pi}\left|\sin\left(\dfrac{\pi R}{2W}\right)\right| & |R| \leq W \\ 0 & |R| > W. \end{cases} \tag{2.21}$$

Since S-L filter function suppressed a high frequency region, low noise images are reconstructed. In this study, we mainly use S-L filter function in reconstruction calculations.

2.5 Iterative reconstruction

Iterative reconstruction is reconstruction methods that use iterative calculations. The block diagram of iterative reconstruction is shown in Fig. 2.6, and the procedure is as follows:

1. Prepare an initial image $\mu'(x, y)$. Generally, a uniform distribution image is used.

2. Perform forward projection to $\mu'(x, y)$ on a computer. As a result, projection data $p'(X, \theta)$ is generated.

3. Compare the differences or the ratios between $p'(X, \theta)$ and actual projection data $p(X, \theta)$, then feed back them to the initial image.

4. Repeat the step 2-3 until the feedback amount is sufficiently small.

Various iterative reconstruction techniques have been proposed, and early X-ray CT had actually used iterative reconstruction. However, iterative calculations require an enormous amount of time compared to back projection algorithms. Therefore, iterative reconstruction was no longer used in X-ray CT since fast and good techniques such as filtered back projection appeared. On the other hand, iterative reconstruction is known as techniques that enable reduction in pixel noise and artifacts, and is effective when the number of projections is small. For these reason, iterative reconstruction has been used for PET (Positron Emission Tomography) and SPECT (Single Photon Emission Tomography).

In this study, we also focused on iterative reconstruction to reduce metal artifacts, and typical iterative reconstruction algorithms are introduced in this section.

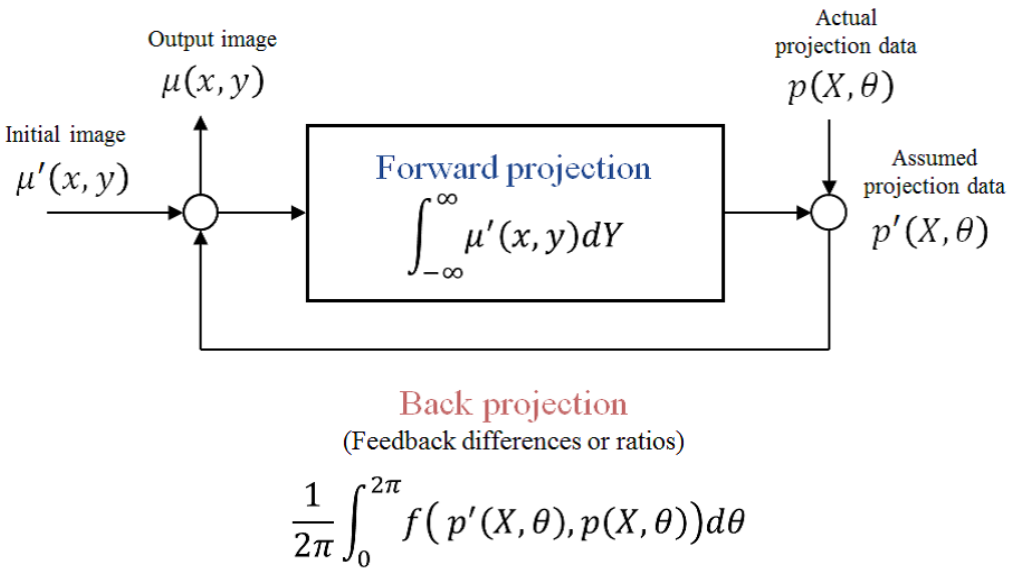

Fig. 2.6: Iterative reconstruction model.

2.5.1 SIRT

SIRT (Simultaneous Reconstruction Technique) is one of the most simple algorithms in iterative reconstruction [20], and the overview can be seen in Fig. 2.6. When a image that was repeated k times is $\mu(x,y)^{(k)}$, a image that was repeated $k+1$ times is $\mu(x,y)^{(k+1)}$, and differences are used as the feedback, the relationship is expressed as follows:

$$\begin{aligned}\mu(x,y)^{(k+1)} &= \mu(x,y)^{(k)} + \frac{1}{2\pi}\int_0^{2\pi}\{p(X,\theta)-p'(X,\theta)\}\,d\theta. \\ &= \mu(x,y)^{(k)} + \frac{1}{2\pi}\int_0^{2\pi}\left\{p(X,\theta)-\int_{-\infty}^{\infty}\mu(x,y)^{(k)}dY\right\}d\theta. \end{aligned} \tag{2.22}$$

When ratios are used as the feedback, the relationship will be:

$$\begin{aligned}\mu(x,y)^{(k+1)} &= \mu(x,y)^{(k)} \times \frac{1}{2\pi}\int_0^{2\pi}\left\{\frac{p(X,\theta)}{p'(X,\theta)}\right\}d\theta \\ &= \mu(x,y)^{(k)} \times \frac{1}{2\pi}\int_0^{2\pi}\left\{\frac{p(X,\theta)}{\int_{-\infty}^{\infty}\mu(x,y)^{(k)}dY}\right\}d\theta. \end{aligned} \tag{2.23}$$

This equation is often rewritten by using coefficient matrix.

$$\lambda_j^{k+1} = \frac{\lambda_j^k}{\sum_{i=1}^{I} C_{ij}} \sum_{i=1}^{I} \frac{y_i C_{ij}}{\sum_{m=1}^{J} C_{im}\lambda_m^k}. \tag{2.24}$$

2.5.2 ART

ART (Algebraic Reconstruction Technique) is similar to SIRT, but the iterative procedure is different [22]. In ART, iterative calculations are performed for each angle, while the calculations are performed at a time in SIRT. When differences are used as the feedback, the repetitive equation of ART is expressed as follows:

$$\begin{aligned} \mu(x,y)^{(k+1)} &= \mu(x,y)^{(k)} + \{p(X,\theta_k) - p'(X,\theta_k)\}\, d\theta \\ &= \mu(x,y)^{(k)} + \left\{ p(X,\theta_k) - \int_{-\infty}^{\infty} \mu(x,y)^{(k)} dY \right\} d\theta. \end{aligned} \tag{2.25}$$

where $theta_k$ means an specific angle, and this equation shows an iterative calculation from only one direction $theta_k$. When ratios are used as the feedback, the relationship will be:

$$\begin{aligned} \mu(x,y)^{(k+1)} &= \mu(x,y)^{(k)} \times \left\{ \frac{p(X,\theta_k)}{p'(X,\theta_k)} \right\} d\theta \\ &= \mu(x,y)^{(k)} \times \left\{ \frac{p(X,\theta_k)}{\int_{-\infty}^{\infty} \mu(x,y)^{(k)} dY} \right\} d\theta. \end{aligned} \tag{2.26}$$

Since the number of image updates in ART is greater than it in SIRT, the convergence speed of $\mu(x,y)$ will become faster by using ART. However, ART also increases a possibility that $\mu(x,y)$ diverge in the process of iterative calculations.

2.5.3 Introduction of coefficient matrix

When dealing with digital data, coordinates of pixels that are given in projection calculations will not indicate integer values in almost all cases. Therefore, it is necessary to interpolate the value by using several pixel values. In this study, we have adopted a method that uses coefficient matrix to perform the interpolation calculation. The coefficient matrix is composed of pixel detection probabilities that indicate projection areas of square pixels. When the coefficient matrix is defined as $C(x_j, y_i, X_n, \theta_m)$, the equation of forward projection calculation becomes:

$$p(X_n,\theta_m) = \sum_{i=i}^{N} \sum_{j=1}^{N} C(x_j, y_i, X_n, \theta_m)\mu(x_j, y_i), \tag{2.27}$$

the equation of back projection calculation becomes:

$$g(x_j.y_i) = \frac{1}{\sum_{n=i}^{N_p}\sum_{m=1}^{N} C(x_j, y_i, X_n, \theta_m)} \sum_{n=i}^{N_p}\sum_{m=1}^{N} C(x_j, y_i, X_n, \theta_m) p(X_n, \theta_m), \tag{2.28}$$

where N means image width, height, and detector width, and N_p means the number of projections. In most cases, X-ray attenuation coefficients $\mu(x, y)$ is rewritten λ_j, and projection data $p(X, \theta)$ is rewritten y_i, by reducing a dimension as shown below:

$$y_i = \sum_{j=i}^{J} C_{ij}\lambda_j, \quad \lambda'_j = \frac{1}{\sum_{i=1}^{I} C_{ij}} \sum_{i=1}^{I} y_i C_{ij}. \tag{2.29}$$

Since coefficient matrix for CT requires a pixel coordinate and three detection probabilities for each pixel, the order of essential memory on computers become $O(4N^2N_p)$. In order to perform interpolation calculations promptly especially in iterative reconstruction, it's very important to prepare coefficient matrix. In forward and back projection calculations of this study, we basically used coefficient matrix.

2.6 Technologies that relate to image reconstruction

In the previous sections, the reconstruction algorithms, which are the core technologies in X-ray CT, were explained. In this section, other technologies that relate to image reconstruction in X-ray CT, such as "fan/parallel conversion," "air calibration," "rotation axis calibration" and "window adjustment" are explained.

2.6.1 Fan/parallel conversion

In the above projection calculations assumed a parallel beam X-ray. However, in actual fields, almost all X-ray CT use a fan beam X-ray or a cone beam X-ray as the X-ray source. In fact, the X-ray CT, which was used in this study, also uses a cone beam X-ray for generating three-dimensional reconstruction data. In order to reconstruct the cone beam data, a dedicated algorithm such as Feldkamp method is needed. Therefore, we firstly used

two-dimensional center data of cone beam data, and regarded them as fan beam data. Since fan beam data can be converted to parallel beam data mathematically, projection algorithms can be simplified. This operation is called fan/parallel conversion.

2.6.2 Air calibration

In actual projection environments, sensitivities of each detector could be different. Furthermore, when the X-ray is fan beam or cone beam, the distance from the X-ray source to the detectors depend on the detector positions. These facts make ring-shaped artifacts on reconstruction images. In order to resolve this problem, air calibration usually is used before reconstruction calculations. As the preparation, you have to collect air data and dark data. Air data means detection intensities in a state that objects are not placed in the path of the X-ray, while dark data means detection intensities in a state that X-rays are not generating. By using these data, projection data are calibrated.

2.6.3 Rotation axis calibration

In ideal scans, the rotation axis is on a line that connects the X-ray source and the center of the detector. However, the rotation axis could be shifted slightly in actual scans, and the fact makes blurred images. Thus, it is necessary to calculate the amount of shift, and modify the rotation axis. For calculating the amount of shift, you only have to make a comparison between projection data from an direction and from an opposite direction.

2.6.4 Window adjustment

Generally, an window level adjustment and an window width adjustment is performed to reconstructed images. The windows level means a median value of a CT image, and the windows width means value width that are displayed. This operation allows to adjust contrast on CT images.

2.7 A scan of an experimental sample

In this section, a scan result of an experimental sample is shown as an example. All CT scans in this study were performed using the micro-focus X-ray CT (ScanXmate-A130SS940) manufactured by Comscantecno Co., Ltd. (Fig. 2.7).

Fig. 2.7: Microfocus X-ray CT.

We prepared the resin experimental sample A (Fig. 2.8), in which four copper poles are embedded. The projection conditions are shown in Table. 2.1, and the FBP result is shown in Fig. 2.9. We can see that metal artifacts are generated around metal poles, and this is an inaccurate cross-sectional image.

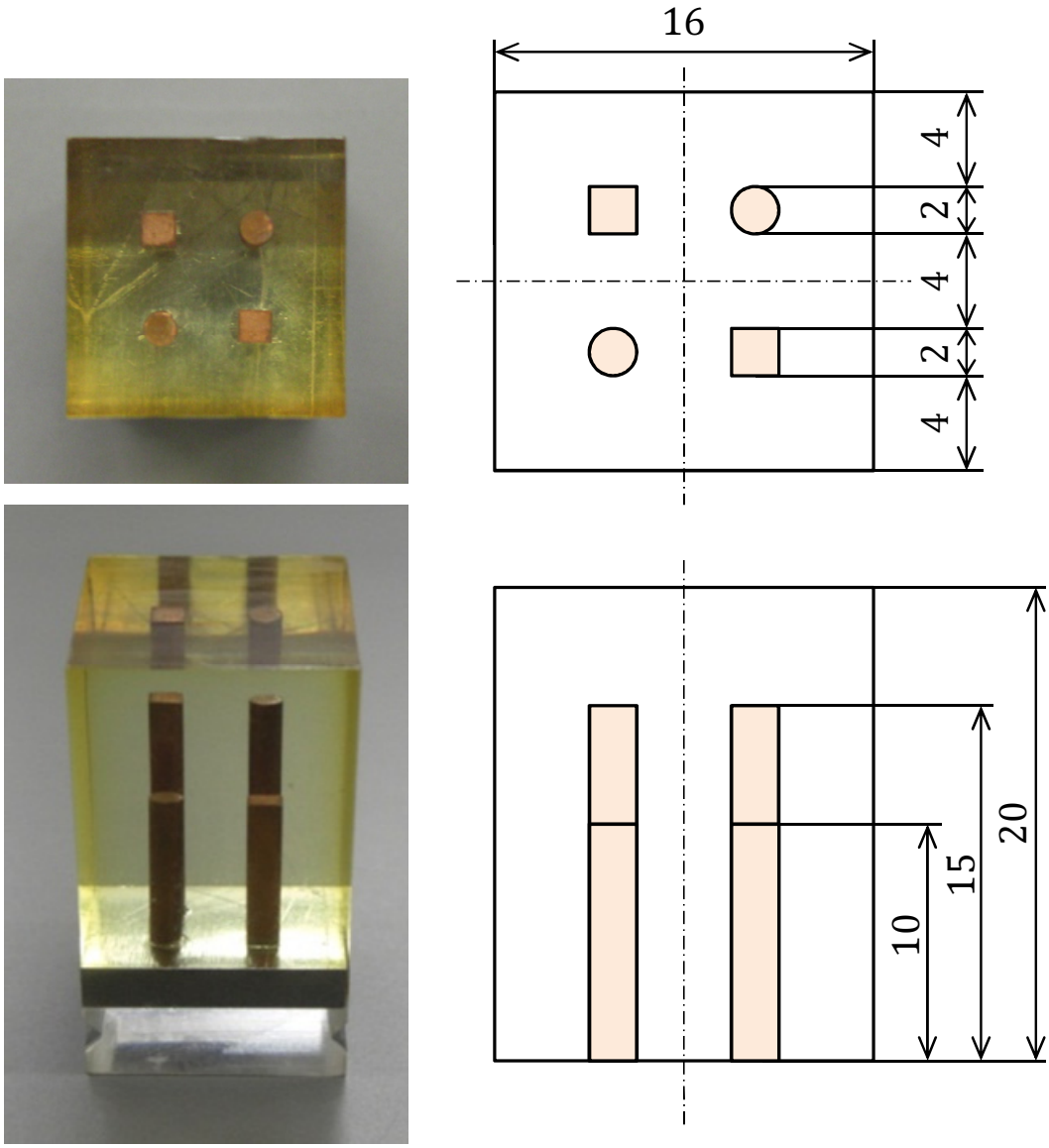

Fig. 2.8: The experimental sample A.

Table 2.1: Projection conditions of the experimental sample A.

Component materials	Resin, iron
Number of metallic objects	4
X-ray tube voltage [kV]	81
X-ray tube current [μA]	53
Number of pixels	512×512
Field of view [mm]	ϕ 24.0
Number of projections	800
Each projection time [s]	0.53

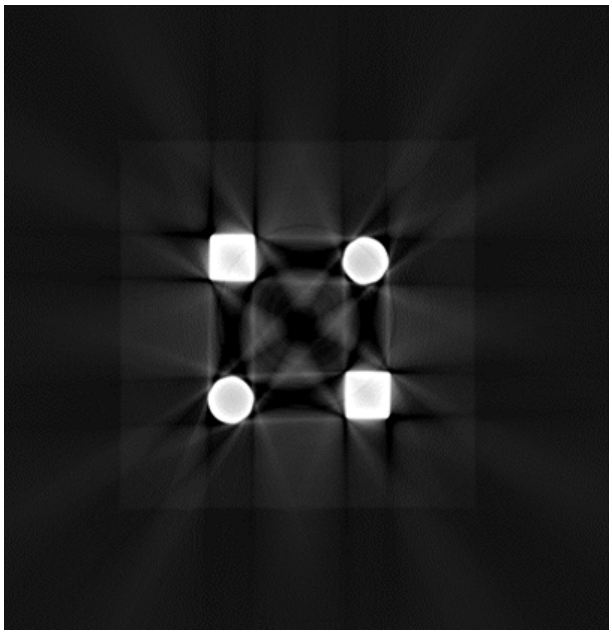

Fig. 2.9: The FBP result of the experimental sample A.

2.8 Causes of metal artifacts

In the previous sections, the principles of X-ray CT and reconstruction algorithms were described, and the example of metal artifacts was shown. In this section, causes of metal artifacts are revealed.

The main causes of metal artifacts are roughly divided into two: a lack of an X-ray intensity and a influence of an X-ray energy spectrum.

2.8.1 Lack of an X-ray intensity

Since metals absorb X-rays extremely, when the X-ray passes through a metal bulk, the X-ray intensity will be significantly reduced. If detectors can't detect the weakened X-ray, or the intensity is indistinguishable from noises, projection data will be invalid and it will be impossible to reconstruct a cross-sectional image of metal regions. Therefore, as a prerequisite in this thesis, we assume that X-rays can be sufficiently detected.

2.8.2 Influence of an X-ray energy spectrum

Even if enough X-rays can be detected, metal artifacts are generated. Since X-ray attenuation coefficients of materials depend on energies of the incident X-ray, Eqn. 2.2 is approved only if the incident X-ray has a single energy like Fig. 2.10. However, X-rays used in actual fields are continuous X-rays that has continuous energy distribution like Fig. 2.11. In such a case, Eqn. 2.2 is rewritten using an integrable system as follows:

$$I_{\text{out}} = \int_E I_{\text{in}}(E) \times \exp\left(-\mu(E) \times t\right) dE. \tag{2.30}$$

Also, the incident X-ray intensity also rewritten as:

$$I_{\text{in}} = \int_E I_{\text{in}}(E) dE. \tag{2.31}$$

Therefore, projection data p becomes:

$$p = -\ln \frac{I_{\text{out}}}{I_{\text{in}}} = -\ln \left(\frac{\displaystyle\int_E I_{\text{in}}(E) \times \exp\left(-\mu(E) \times t\right) dE}{\displaystyle\int_E I_{\text{in}}(E) dE} \right). \tag{2.32}$$

This equation means that p is non-linear with respect to an object thickness t. Although we should perform reconstruction calculations using Eqn. 2.5, we actually have used Eqn. 2.32, because it is difficult in current technologies to get X-ray intensities for each energy. This fact implies that continuous X-rays are regarded as monochromatic X-rays. Such an assumption could cause discrepancies in reconstruction calculations, however, if the objects are human bodies or resins, the influences of the discrepancies can be ignored, because X-ray attenuation coefficients of non-metals don't depend on X-ray energies much. Conversely, X-ray attenuation coefficients of metals highly depend on X-ray energies, and continuous X-rays that passed through metals are concentrated in the high energy side (which is called beam hardening). Therefore, if the objects include metals, the linearity of projection will be impaired, and the influences of the discrepancies will become huge. This discrepancies of calculation is the major cause of metal artifacts. As examples, properties of projection data are shown in Fig. 2.12

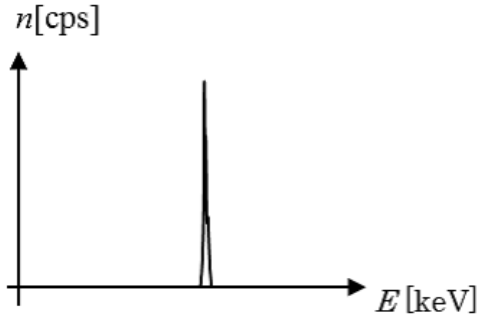

Fig. 2.10: A monochromatic X-ray spectrum.

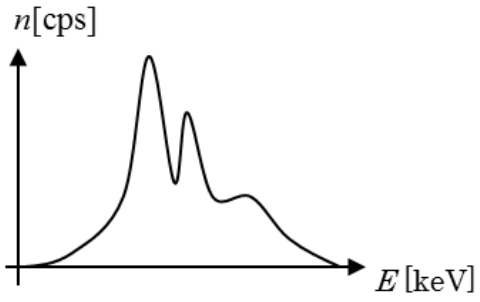

Fig. 2.11: A continuous X-ray spectrum.

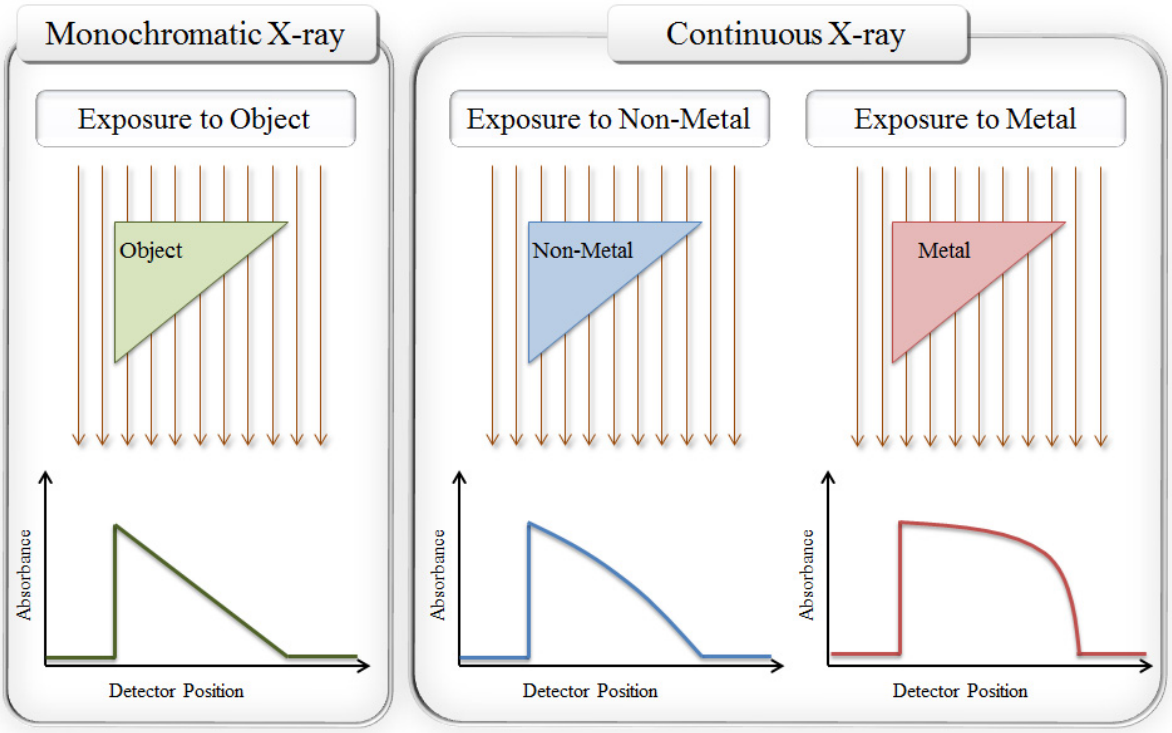

Fig. 2.12: Comparison of projection data.

Chapter 3

Simulation of X-ray CT

Chapter 3: Simulation of X-ray CT

To understand deeply X-ray CT, and to determine the efficacy of our reconstruction algorithm, we developed X-ray CT simulation software (Fig. 3.1) using Java. The development environment is shown in the following:

- Language :Java
- Platform :Java SE/JDK 8 update 45
- Java IDE :NetBeans IDE 8.0.2

This software can inputs/outputs CT data, and computes conventional reconstruction images, as well as images using our reconstruction algorithm. In this chapter, knowledges and processes based on CT simulation are described.

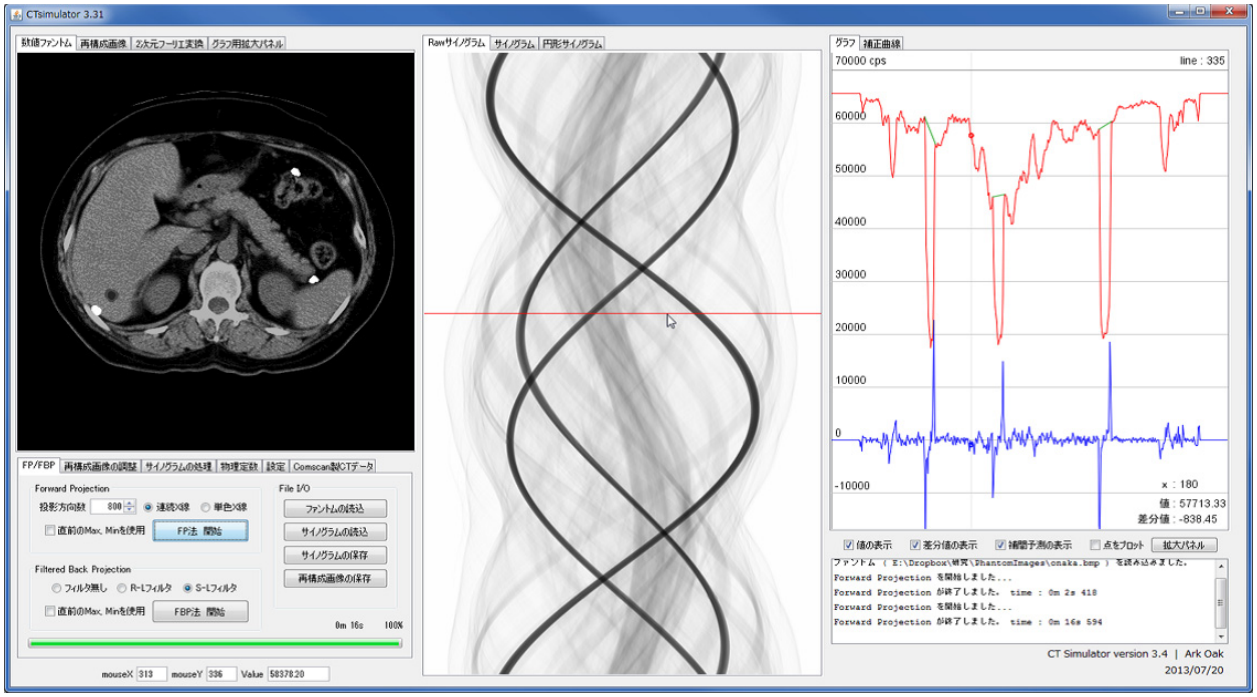

Fig. 3.1: The X-ray CT simulation software.

3.1 Numerical phantom

A numerical phantom is used as a virtual cross-sectional image in X-ray projection simulation. Numerical phantoms in this study are represented by bitmap images of 256 level gray scale. Fig. 3.2 shows an example of numerical phantom, which assumes the experimental sample A(Fig. 2.8). Forward projection calculations can be possible by associating colors (image density) of the phantom with X-ray attenuation coefficients. Typical X-ray attenuation coefficients that are used in this study are shown in Table. 3.1.

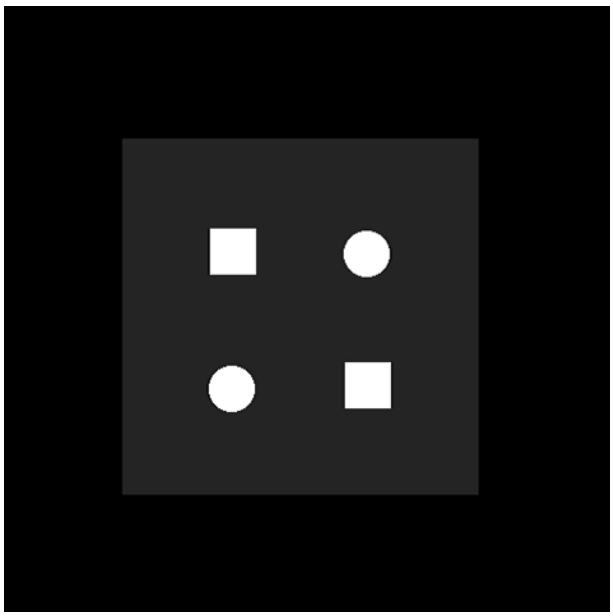

Fig. 3.2: The numerical phantom assuming the experimental sample A.

Table 3.1: X-ray attenuation coefficients.

Energy[keV]	10	20	30	40	50	60	80	100
Resin	0.39948	0.06800	0.03608	0.02797	0.02468	0.02290	0.01953	0.01733
Soft tissue	0.48690	0.074530	0.034300	0.024320	0.020480	0.018520	0.016480	0.01531
Hard tissue	0.81150	0.12420	0.057170	0.040530	0.034130	0.030870	0.027470	0.025520
Bone	4.4191	0.62016	0.20631	0.10315	0.065750	0.048790	0.034550	0.028753
Aluminium	7.8930	1.0397	0.33444	0.16331	0.10213	0.074691	0.051890	0.042737
Silicon	10.375	1.3886	0.43739	0.20435	0.12107	0.083897	0.053510	0.041814
Calcium	14.479	2.0243	0.63240	0.28365	0.15795	0.10196	0.056668	0.039851
Scandium	29.707	4.2059	1.3161	0.58775	0.32447	0.20692	0.11203	0.076923
Titanium	49.881	7.1420	2.2404	0.99763	0.54658	0.34520	0.18258	0.12261
Vanadium	73.080	10.608	3.3384	1.4832	0.80820	0.50628	0.26226	0.17262
Chromium	99.653	14.653	4.6260	2.0535	1.1145	0.69304	0.35267	0.22764
Manganese	107.80	16.041	5.0844	2.2563	1.2204	0.75472	0.37779	0.23973
Iron	134.33	20.220	6.4378	2.8575	1.5417	0.94882	0.46866	0.29268
Cobalt	163.85	24.947	7.9762	3.5431	1.9082	1.1695	0.57085	0.35146
Nickel	186.18	28.684	9.2109	4.0977	2.2038	1.3469	0.65082	0.39552
Copper	193.45	30.276	9.7843	4.3564	2.3412	1.4273	0.68365	0.41073
Lead	148.23	98.019	34.413	16.299	9.1265	5.6988	2.7456	6.2981

3.2 Forward projection

When a numerical phantom is given, forward projection calculations can be performed by using Eqn. 2.5 or Eqn. 2.32. In our X-ray CT simulation, parallel beam projections are performed from many different direction surrounding the phantom, and projection data are collected. We can use Eqn. 2.5 in case the incident X-rays are monochromatic X-rays. However, we have to use Eqn. 2.32 on condition that the incident X-rays are continuous X-rays.

3.3 Sinogram

After forward projection calculations, aligned projection data called sinogram is generated as well as actual scans. By introducing the sinogram, many projection data can be unified in one image data. Also, one sinogram allows us to reconstruct one cross-sectional image.

3.4 Back projection

When a sinogram is given, back projection calculations described in Chapter 2 can be performed. In this thesis, we chose the FBP method that uses a S-L filter as a conventional reconstruction method for comparison with new algorithms.

3.5 Simulation experiments

3.5.1 Irradiation of monochromatic X-rays

We irradiated the phantom of Fig. 3.2 with monochromatic X-rays from 800 directions on our simulation software. The generated sinogram is shown in Fig. 3.3(a), and the reconstruction result by FBP is shown in Fig. 3.3(b). There are almost no artifacts on this reconstruction image. This result shows that the forward projection and back projection calculations were performed accurately, and no metal artifacts are generated when using monochromatic X-rays. However, this reconstruction image has some artifacts around metals. This artifact is due to the number of projections, and the details are described in appendix A.

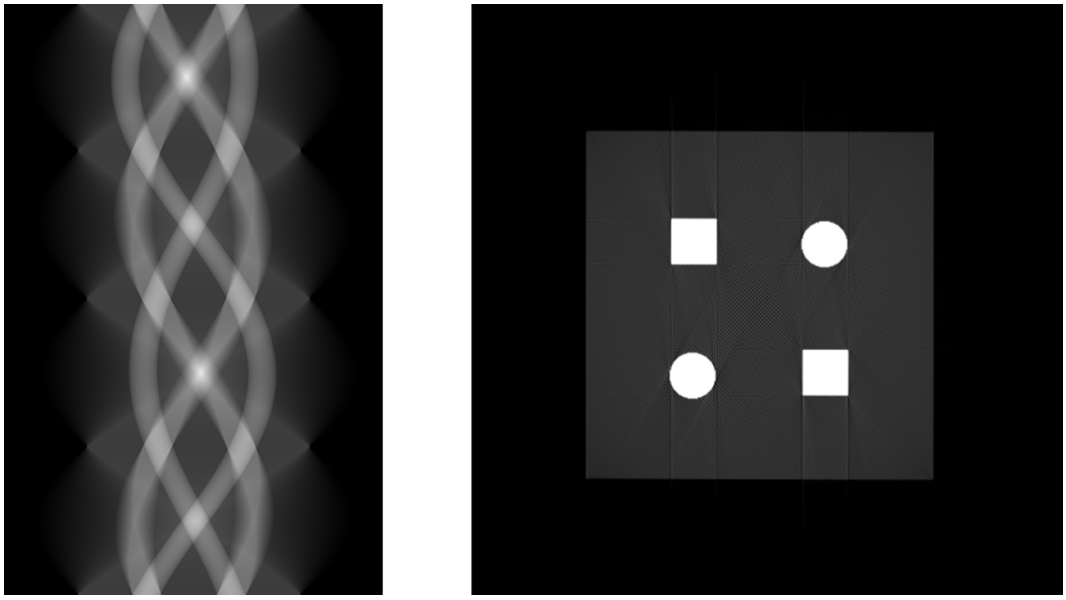

(a) (b)

Fig. 3.3 Simulation of monochromatic X-ray. (a) is the sinogram, and (b) is the FBP result.

3.5.2 Discretization of continuous X-rays

In order to reproduce metal artifact on simulations, forward projection calculations using continuous X-rays that assume actual scan environments are necessary. However, it is difficult to get X-ray intensities for each energy of continuous X-rays using current technologies.

The discrete X-ray distribution used in this thesis is shown in Fig. 3.4. This distribution is given by a spectrum at the tube voltage 130 kV that are obtained using a spectrum analyzer (AMPTEX Inc. : XR-100T-CdTe). Thus, assuming continuous X-rays, we defined discrete X-rays composed of eight type energies (10, 20, 30, 40, 50, 60, 80, 100 keV), which are corresponding to Table 3.1. The most important thing to generate discrepancies that cause metal artifacts is to irradiate object with low energy X-rays and high energy X-rays simultaneously, so it's thought that such a rough discretization is also sufficient.

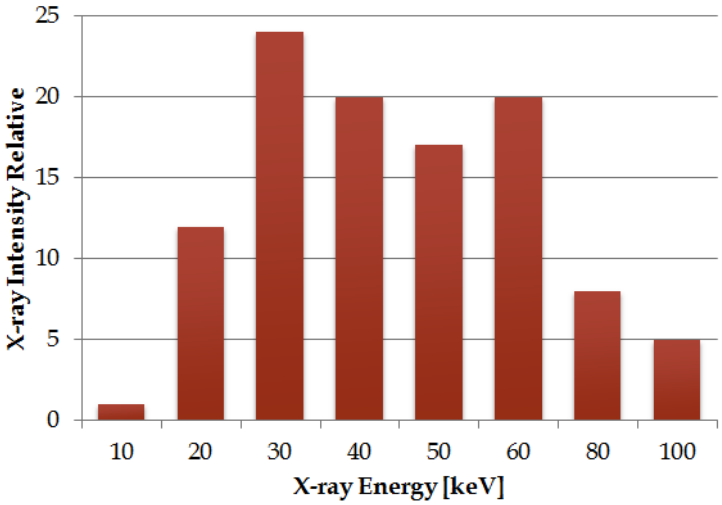

Fig. 3.4: Discrete X-ray energy.

3.5.3 Irradiation of discrete X-rays

X-ray intensities that are read by detectors depend on the energy of the photon, and the continuous X-ray can be considered as a collection of photons with different energies. When continuous X-rays are assumed to be N type energies, intensities that are read by detectors can be described as follows:

$$\begin{aligned} [\text{Intensity}] &= \sum_{i=1}^{N} [\text{Energy}] \times [\text{Number of photoms}] \\ &= \sum_{i=1}^{N} E_i n_i. \end{aligned} \tag{3.1}$$

And a transmitted X-ray intensity is:

$$I = \sum_{i=1}^{N} E_i n_i \exp\left(-\int \mu(E_i) dy\right). \tag{3.2}$$

Projection data p becomes:

$$p = -\ln \frac{I}{I_0} = -\ln \left(\frac{\sum_{i=1}^{N} E_i n_i \exp\left(-\int_E \mu(E_i) dy\right)}{\sum_{i=1}^{N} E_i n_i} \right). \tag{3.3}$$

In our forward projection simulations with discrete X-rays, Eqn. 3.3 is mainly used.

We irradiated the phantom of Fig. 3.2 with discrete X-rays from 800 directions on our simulation software. The generated sinogram is shown in Fig. 3.5(a), and the reconstruction result by FBP is shown in Fig. 3.5(b). Comparing Fig. 3.5(b) with the actual data Fig. 2.9, both images have the similar metal artifacts from metal portions, and it can be said that these are the same qualitatively. This result indicates that causes of metal artifacts are energy dependence of X-ray attenuation coefficients, and our simulation is valid.

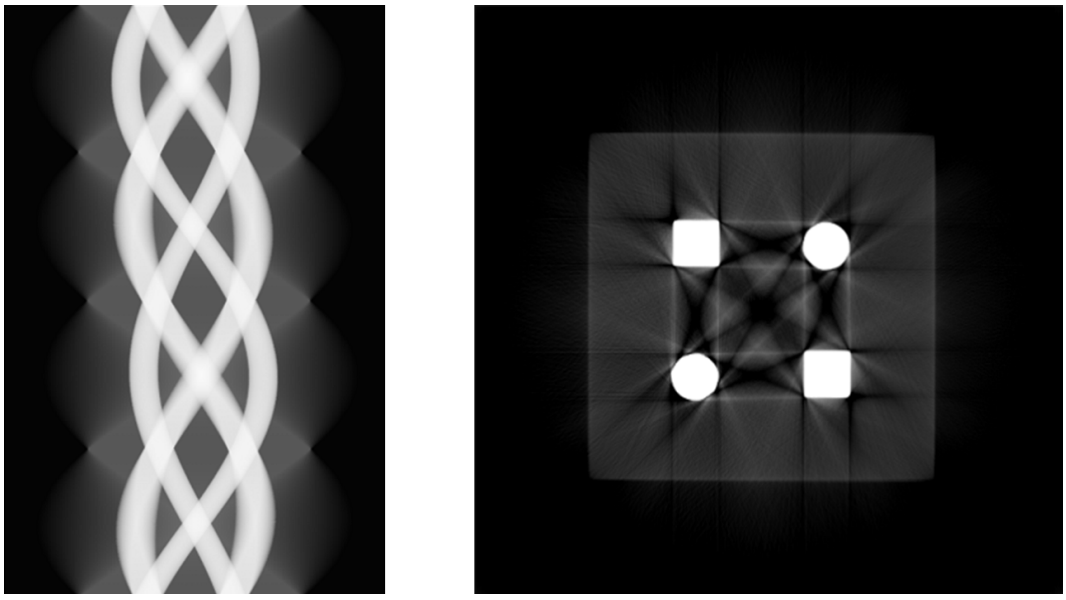

(a) (b)

Fig. 3.5: Simulation of continuous X-ray. (a) is the sinogram, and (b) is the FBP result.

3.6 Image evaluation methods

In actual fields, it is sometimes thought that qualitative evaluations are sufficient as image evaluations. This study performs not only such qualitative evaluations, but also quantitative evaluations for verifying effects of metal artifact reduction. This section describes quantitative evaluation methods that are used in this study.

3.6.1 RMSE

RMSE (Root mean square error) is widely used as a quantitative image evaluation method. This evaluation is based on the difference between an original image and an output image, and defined as:

$$\mathrm{RMSE} = \sqrt{\frac{\sum_y \sum_x \{\mu_0(x,y) - \mu(x,y)\}^2}{\mathrm{WIDTH} \times \mathrm{HEIGHT}}}, \tag{3.4}$$

where μ_0 is the original image, μ is the output image, WIDHT and HEIGHT are the image width and the image height respectively. When the two images are completely the same, the value of RMSE becomes 0. Also, since we defined that image densities are represented 256 level grayscale ($0 \leq \mu \leq 255$), the maximum value of RMSE is theoretically 255.

3.6.2 SSIM

In the RMSE, there is a possibility that the values and the qualitative evaluation are different. For example, if an image is slightly different in whole from an original image, we will regard it as a high quality result, but the RMSE value will indicate high value. On the other hand, if an image is significantly different in a local part from an original image, we will think that the image is deteriorated, but the RMSE value will indicate small value. In order to represent numbers that are closer to human senses than the case of RMSE, Wang et al. proposed a new quantitative evaluation method called SSIM (Structural similarity) [21]. It has been confirmed there is a high correlation between the SSIM and human senses. The SSIM is defined as:

$$\mathrm{SSIM}(x,y) = \frac{(2\mu_x\mu_y + c_1)(2\sigma_{xy} + c_2)}{(\mu_x^2 + \mu_y^2 + c_1)(\sigma_x^2 + \sigma_y^2 + c_2)}, \tag{3.5}$$

where μ is the average, σ is the variance, and c is the variable to stabilize the division with weak denominator. When the image densities are represented 256 level grayscale ($0 \leq \mu \leq 255$), typically c_1 and c_2 are $(0.01 \times 255)^2$ and $(0.03 \times 255)^2$, respectively. The SSIM values are expressed between 0 and 1, and it implies that the image quality is higher as the value approaches to 1. In this evaluation index, by using averages, variances, and a covariance, it has allowed the representation of the local value differences. Generally, when the SSIM value exceeds 0.95, the image is considered as high quality. Furthermore, when the SSIM value exceed 0.98, it is difficult to distinguish the image from the original one.

3.6.3 SLP

Although RMSE and SSIM are useful quantitative evaluation methods, since these evaluations require an original image, they can't be used for actual CT images. Therefore, we propose a new quantitative evaluation method based on two-dimensional Fourier transform for actual CT images. If there is a quantitative indicator of the amount of generated artifacts, it could be possible to estimate various parameters in CT imaging environments.

In the new evaluation, two-dimensional Fourier transform is firstly performed. Then the sum of low frequency power spectrum (SLP) is calculated:

$$\mathrm{SLP}(F) = \int\int_C \mathrm{Re}(F(u,v))^2 + \mathrm{Im}(F(u,v))^2 du dv. \tag{3.6}$$

$$F(u,v) = \int_{-\infty}^{\infty}\int_{-\infty}^{\infty} f(x,y)\exp(-i2\pi(ux+vy))dxdy, \tag{3.7}$$

where $f(x,y)$ is an output image, $F(u,v)$ is the result of two-dimensional Fourier transform, and C represents the low frequency region. In this study, we defined that the low frequency region is a circular area with a radius of 1/20 of the image in the two-dimensional Fourier transform result.

To explain the theory of SLP, we prepared a numerical phantom shown in Fig. 3.6(a) assuming the experimental sample B(Fig 4.8). We gave the iron property as the X-ray attenuation coefficient of metal, and performed the forward projection calculation from 512 directions. The FBP result using monochromatic X-rays is shown in Fig. 3.6(b), and the

FBP result using discrete X-rays is shown in Fig. 3.6(c). We see that there are almost no artifacts on Fig. 3.6(b), while terrible artifacts are generated on Fig. 3.6(c). Refer to Fig. 3.7. Fig. 3.7(a) is the line profile of the center of Fig. 3.6(b) ($A - A'$), and Fig. 3.7(b) is the line profile of the center of Fig. 3.6(c) ($B - B'$). In Fig. 3.7(b), overshoots of pixel values were occurred between metal regions, and this reduced the contrast of non-metal regions. As the result, the boundary between resin regions and air regions became blurred. The Fourier transform results of these line profiles are shown in Fig. 3.8. The low frequency region of Fig. 3.8(a) seems to be larger than one of Fig. 3.8(b). This result implies that overshoots of pixel values caused by metals decrease the power spectrum of the low frequency region. The reason is considered that the overshoots raise entire values and it makes difficult to reproduce signals by using low frequency components.

From the above facts, SLP(F), which indicates the sum of low frequency power spectrum, will increase as metal artifacts are reduced. To verify this property, we repeatedly conducted simulation experiments using Fig. 3.6(a) while changing the X-ray attenuation coefficient of metals, and performed an analysis of correlation between SLP and RMSE. Fig. 3.9 is the simulation results: Fig. 3.6(a) is using the magnesium property, Fig. 3.6(b) is using the aluminum property, Fig. 3.6(c) is using the calcium property, and Fig. 3.6(d) is using the titanium property. It can be confirmed that the amount of metal artifact generation increase as the atomic number increases. The relationship between RMSE and SLP for these FBP images is shown in Fig. 3.10. The determination coefficient in this correlation analysis shows a very high value as $R^2 = 0.9328$, and this means that there is a strong correlation between SLP and RMSE. That is, SLP is valid as a image evaluation method of the amount of metal artifacts generation.

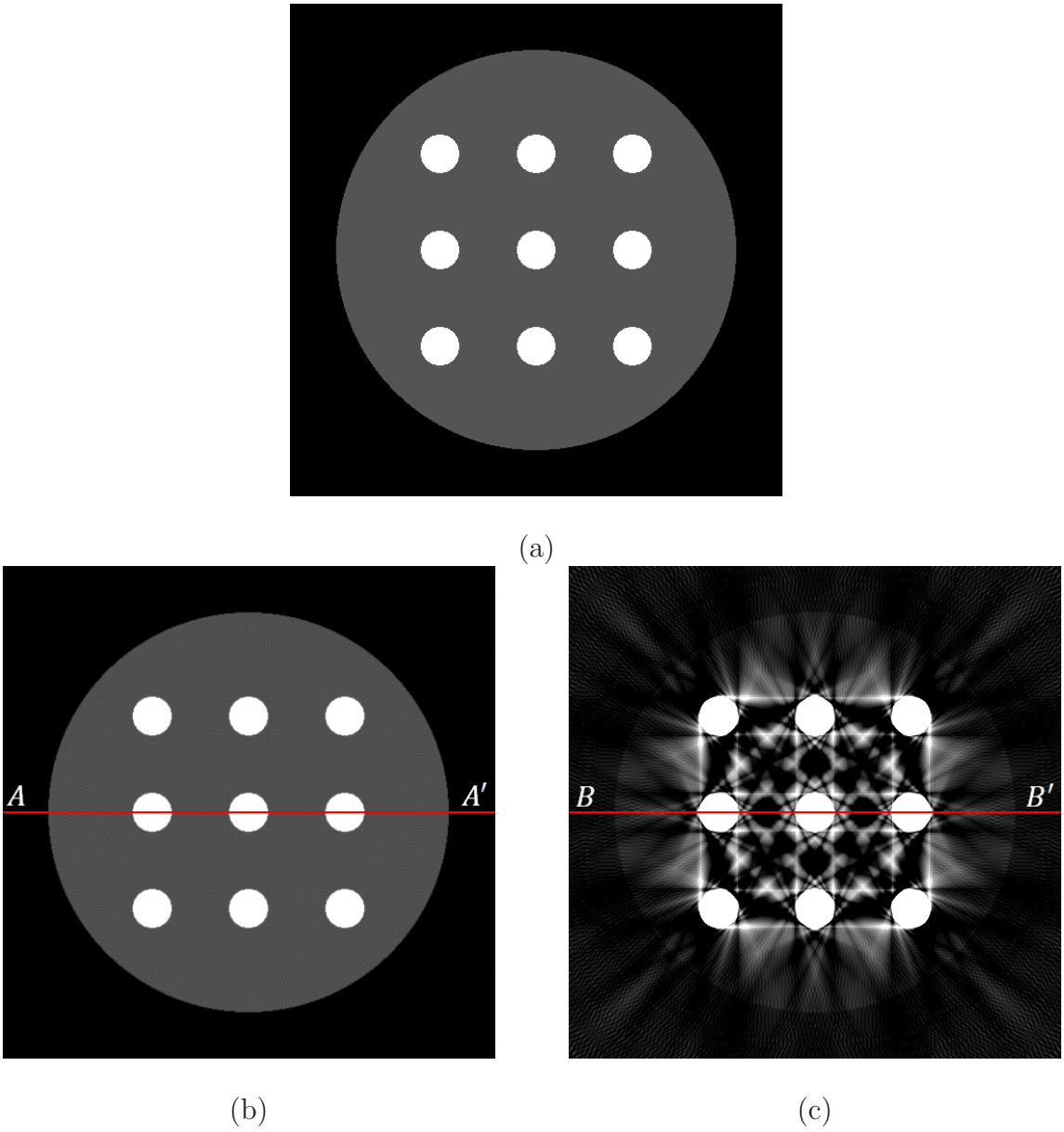

(a)

(b)

(c)

Simulation conditions	
Component materials	Resin, iron
Number of metallic objects	9
Number of pixels	512×512
Field of view [mm]	ϕ 30.7
Number of projections	512

Fig. 3.6 An X-ray CT simulation example. (a) is the numerical phantom composed of resin and metals; FBP results using (b) monochromatic X-rays , (c) discrete X-rays.

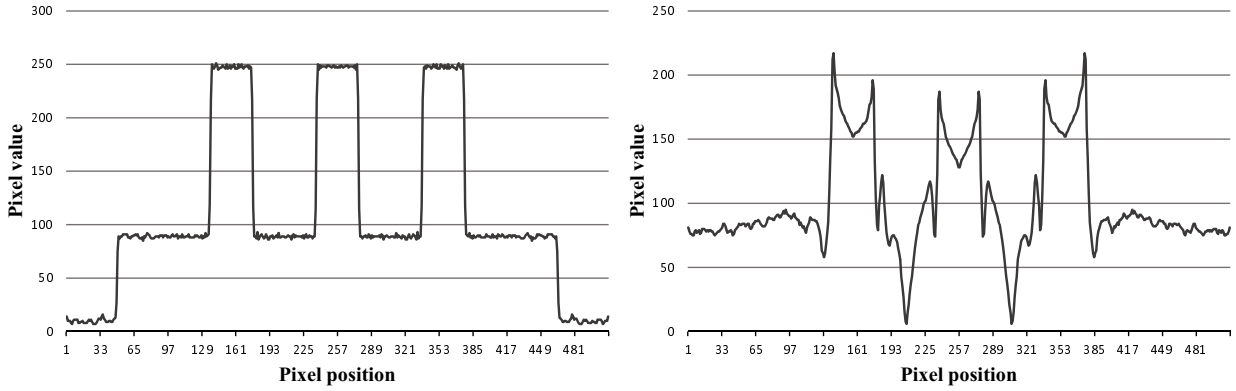

(a) $A - A'$ (b) $B - B'$

Fig. 3.7: Profiles of FBP results.

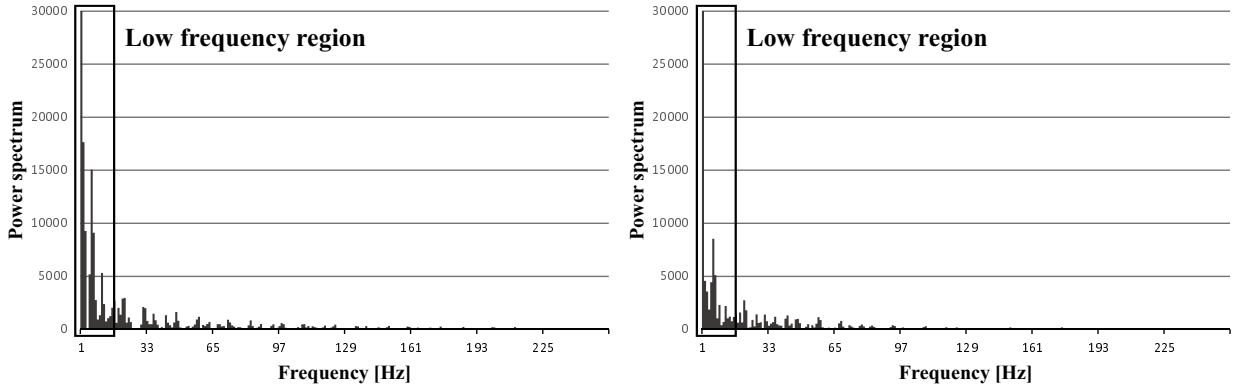

(a) $A - A'$ (b) $B - B'$

Fig. 3.8: Fourier translation results.

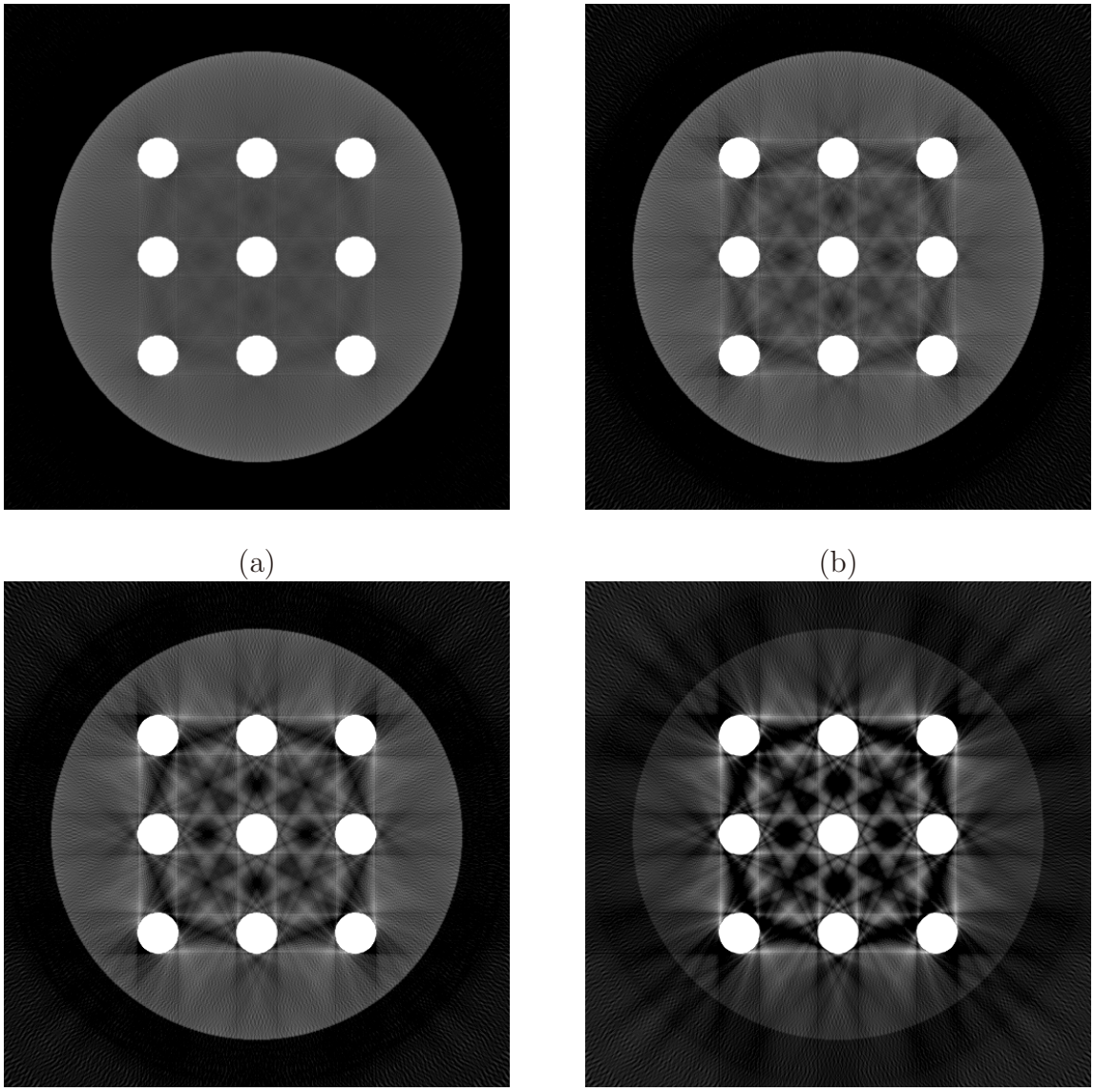

(a) (b)

(c) (d)

Fig. 3.9 The FBP results from the simulation using the X-ray attenuation coefficients of (a) magnesium, (b) aluminum, (c) calcium, (d) titanium.

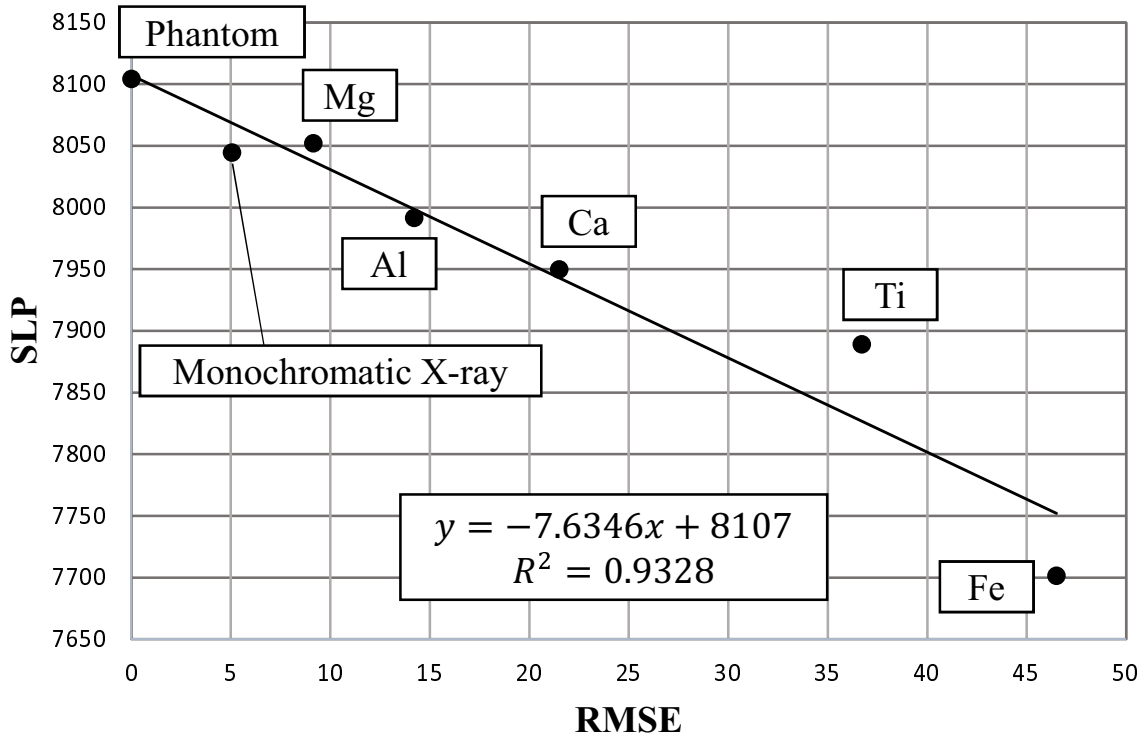

Fig. 3.10: The correlation analysis between SLP and RMSE.

Chapter 4

Metal artifact reuction based on sine curves

Chapter 4: Metal artifact reuction based on sine curves

In this chapter, we propose a metal artifact reduction method that is based on a nature of a sinogram.

4.1 Metal artifact reduction method 1 (MAR1)

4.1.1 Sinogram analysis

A sinogram consists of the aligned projection data in a specific X-ray cross section. Forward projection is performed while the X-ray source (or an object) rotates around a specific axis, tracing out a sine curve of period 2π for each object/feature. A discrepancy of projection data on a sinogram can be observed prominently at an intersection of metal sine curves. To correct the discrepancy, we focused on shape features of sine curves on sinograms, and propose a new algorithm that can reconstruct a metal region and a non-metal region individually. Fig. 4.1 shows the conceptual diagram of the proposed algorithm. The details of the algorithm are described below.

4.1.2 Sine curve extraction

We first extract sine curves from the sinograms. Each point with coordinates (x, y) on a cross-sectional image has an associated sine curve. However, the value along each sine curve is not constant because of their superposition. Our algorithm extracts sine curves according to the continuity of their values. When a polar coordinate system (r, ϕ) is defined as $x = r\cos\phi,\ y = r\sin\phi$, values along a sine curve $f(\theta)$ drawn by a point on a cross-sectional image are expressed as follows:

$$f(\theta) = r\sin(\theta + \phi) = \sqrt{x^2 + y^2}\sin\left(\mathrm{atan}\frac{y}{x} + \theta\right), \tag{4.1}$$

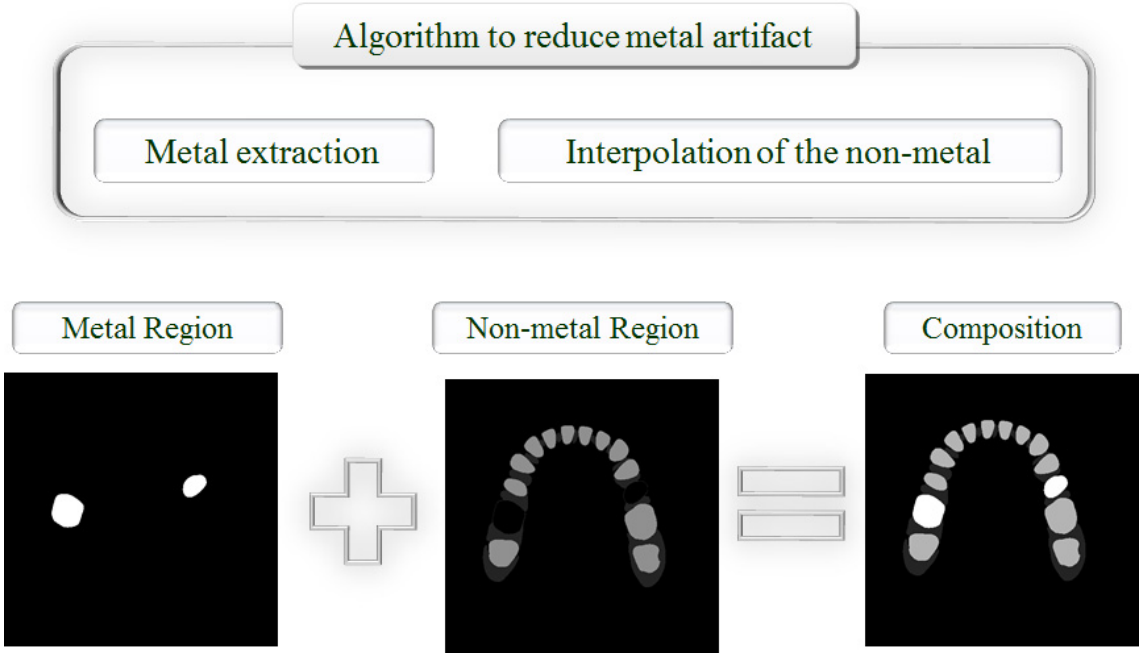

Fig. 4.1: A conceptual diagram of the proposed algorithm.

where θ is the angular coordinate of the sinogram corresponding to the projection angle. Given the number of projection p, θ becomes:

$$\theta = 2\pi i/p \quad (i = 0, ..., p-1). \tag{4.2}$$

To evaluate the continuity of the values, we defined the function $cont(\theta)$ as:

$$cont(\theta) = \begin{cases} 1 & \left(\left| \frac{d}{d\theta} v\left(f(\theta)\right) \right| \leq \text{DIFF} \right) \\ 0 & \text{otherwise,} \end{cases} \tag{4.3}$$

where DIFF is a criteria value of continuity between two values. By integrating Eqn. 4.3 along the theta direction, sine curve continuities are quantified. Here, we defined the following evaluation equation:

$$\int_0^{p-1} cont(\theta) d\theta \geq p \times \text{RATIO}, \tag{4.4}$$

where RATIO is a criteria value of a sine curve. By using the above equations, curves are extracted even when there are large local variations in $f(\theta)$. Our value-continuity method exhibits superior performance to simple threshold processing.

4.1.3 Metal reconstruction

The sine curves of metals are readily distinguishable from those of non-metals and can be extracted accurately. Each sine curve corresponds to one pixel on the cross sectional image. Therefore, the easily identifiable metal sine curves yield one pixel in the image (Fig. 4.2). In an iterative procedure we reconstruct the metal region. For reconstruction algorithms, like FBP, metal objects project non-linearly, resulting in artifacts. This problem does not occur in our method.

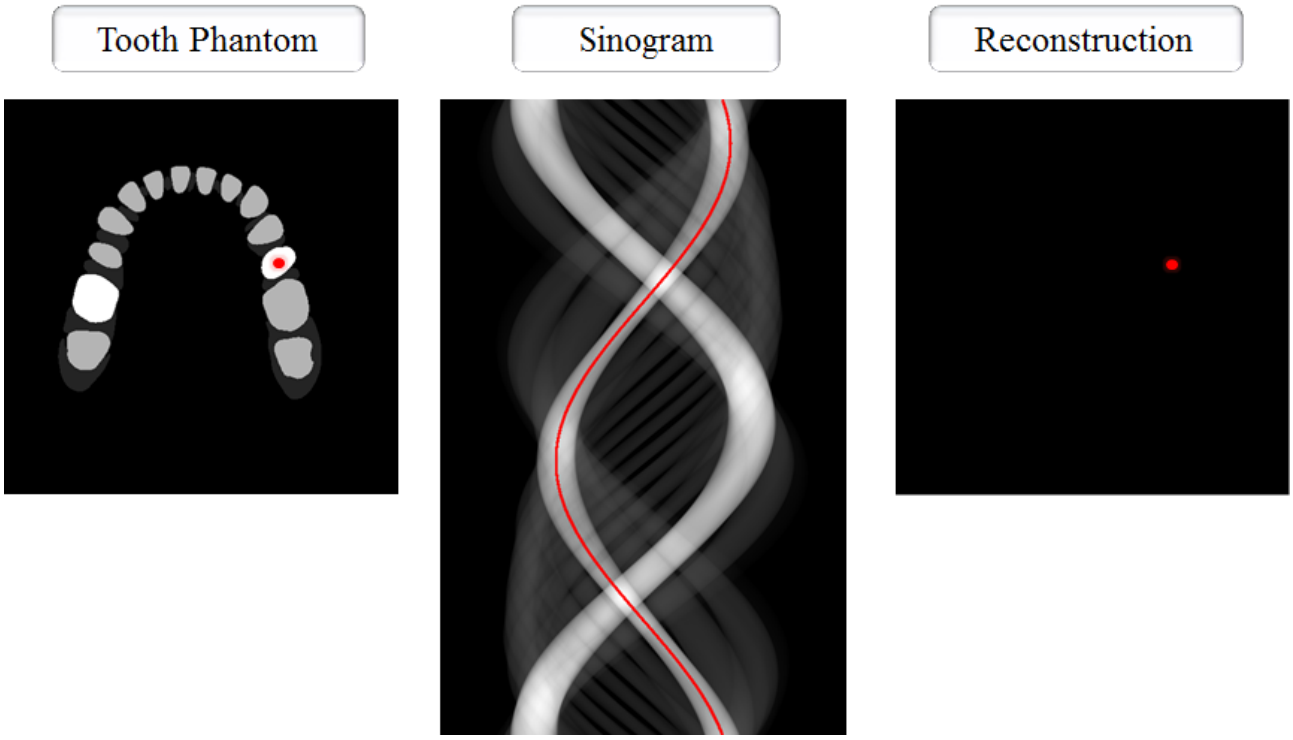

Fig. 4.2 The concept of metal extraction. The left figure shows the tooth numerical phantom with embedded two metal teeth, and the center figure is the sinogram of the tooth phantom. The red point on a metal tooth in the tooth phantom corresponds to a red sine curve on the sinogram. When one sine curve is extracted from the sinogram, it enables one pixel reconstruction as shown in the right figure.

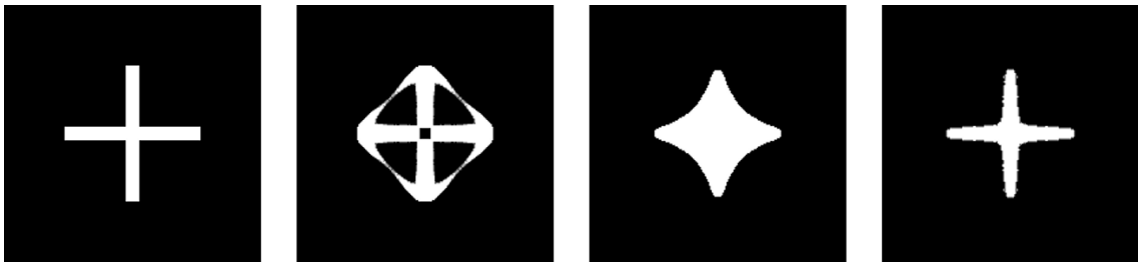

(a) (b) (c) (d)

Simulation conditions	
Component materials	Iron
Number of metallic objects	1
Number of pixels	256×256
Dot pitch [mm]	0.12
Number of projections	800

Fig. 4.3 Comparison of the shape extraction. (a) is the numerical phantom of cross shaped metal, (b) is the threshold processing result after performing FBP, (c) is the reconstruction result using sine curves without continuity information, (d) is the reconstruction result using sine curves with continuity information.

Refer to Fig. 4.3. Fig. 4.3(a) is the numerical phantom of cross shaped iron, and Fig. 4.3(b) is the threshold processing result after performing FBP. It is found that the contour can't be extract using the simple threshold processing. Fig. 4.3(c) is the reconstruction result using sine curves without continuity information. Although the metal artifacts were reduced, the concave portion could not be reconstructed accurately. Fig. 4.3(d) is the reconstruction result using the proposed algorithm. It was confirmed that accurate images could be reconstructed by evaluating continuities of values along sine curves. For reference, parameter conditions in this experiment are:$p = 800,\ \mathrm{DIFF} = 1000,\ \mathrm{RATIO} = 0.95$. Also, the ranges of $v\left(f(\theta)\right)$ and DIFF is $[0, 65535]$.

4.1.4 Non-metal interpolation

The sine curves of non-metal features are not so easily distinguished thus we employ an interpolation in the non-metallic regions. The steps of this procedure are shown in Fig. 4.4. After the metal sine curves are extracted, the sinogram is null padded to filter the non-metal regions. Next, we detect the dominant non-metal sine curves, which are used for interpolation of metal areas. In the region where the metallic and non-metallic sine curves intersect, interpolation is used to smooth the sinogram. When all non-metal areas have been filled the CT image is complete.

In this way, by reconstructing the separate metal and non-metal images then synthesizing them, we eliminate metal artifacts. The overall flow char of the algorithm is shown in Fig. 4.5.

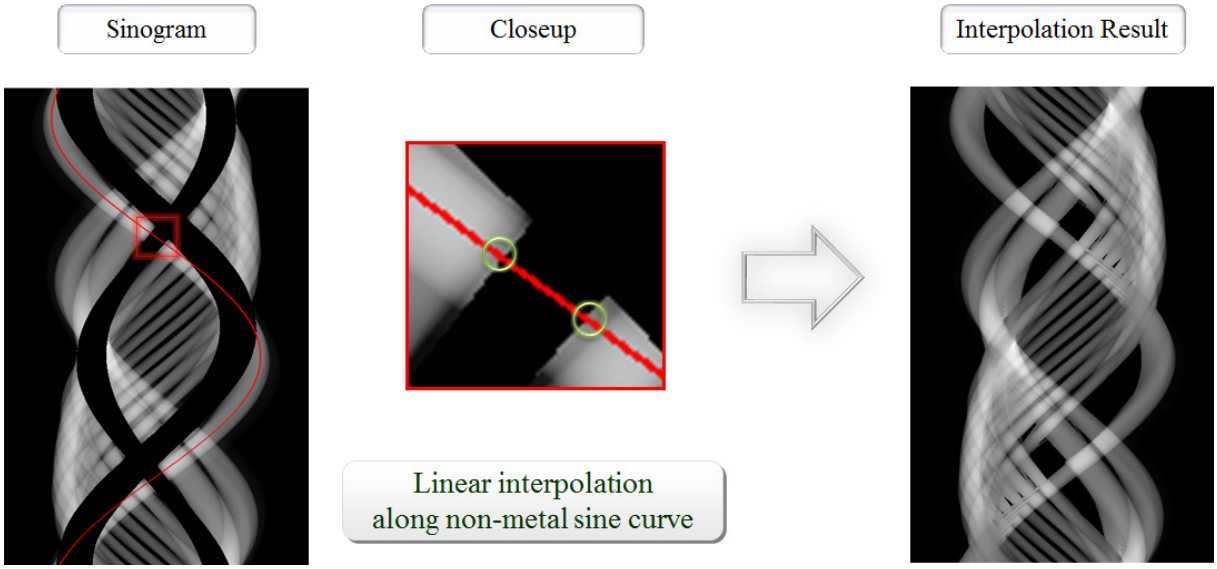

Fig. 4.4 The concept of non-Metal interpolation. The left figure is the sinogram of the tooth numerical phantom shown in Fig. 4.2 that metal sine curves were extracted, and the red sine curve is drawn by a pooint on a tooth. By performing linear interpolation along non-metal sine curves (the center figure), the sinogram is interpolated smoothly (the right figure).

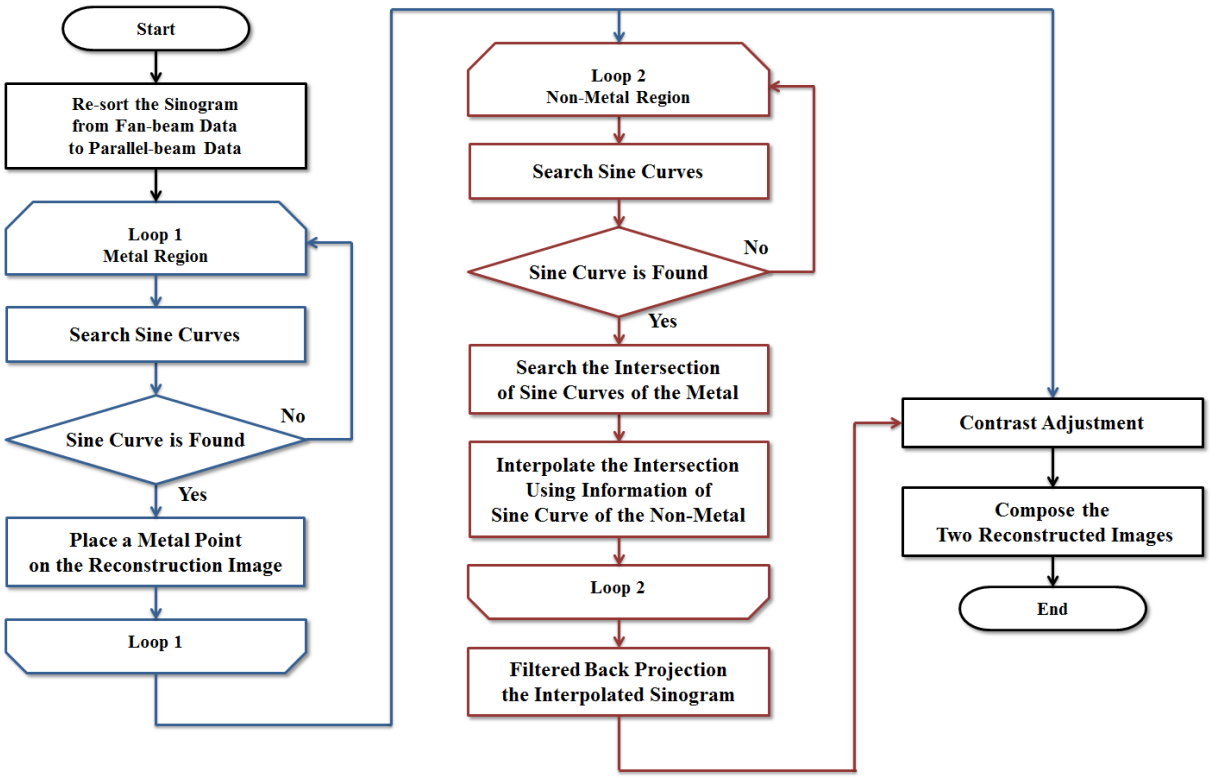

Fig. 4.5 The flow chart of proposed algorithm based on sine curve extraction. The blue charts indicates the process of the metal extraction, and the red charts indicates the process of the non-metal interpolation.

4.2 Application to CT data (MAR1)

The results of applying our algorithm (MAR1) to X-ray CT images of physical objects is shown in this section.

4.2.1 The experimental sample A

The experimental sample A has already been introduced in Fig. 2.8 in Chapter 3. Two iron cylinders and two iron square poles are embedded in this sample. Also, the projection conditions are shown again in Table. 2.1. The metal artifacts generated from metal objects in conventional FBP images are clearly shown in Fig. 4.6. Fig. 4.7(a) is the extraction result of metal regions, and Fig. 4.7(b) is the result of synthesis. Metal artifacts were significantly reduced by applying our new reconstruction algorithm.

Table 4.1: Projection conditions of the experimental sample A.

Component materials	Resin, iron
Number of metallic objects	4
X-ray tube voltage [kV]	81
X-ray tube current [μA]	53
Number of pixels	512×512
Field of view [mm]	ϕ 24.0
Number of projections	800
Each projection time [s]	0.53

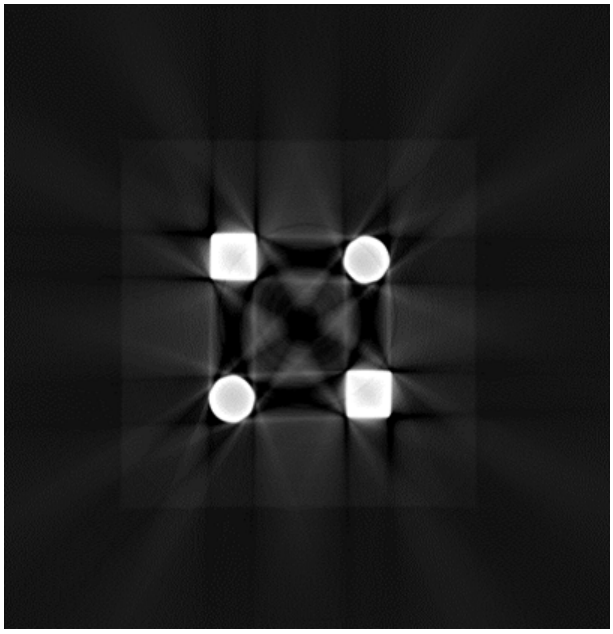

Fig. 4.6: The FBP result of the experimental sample A.

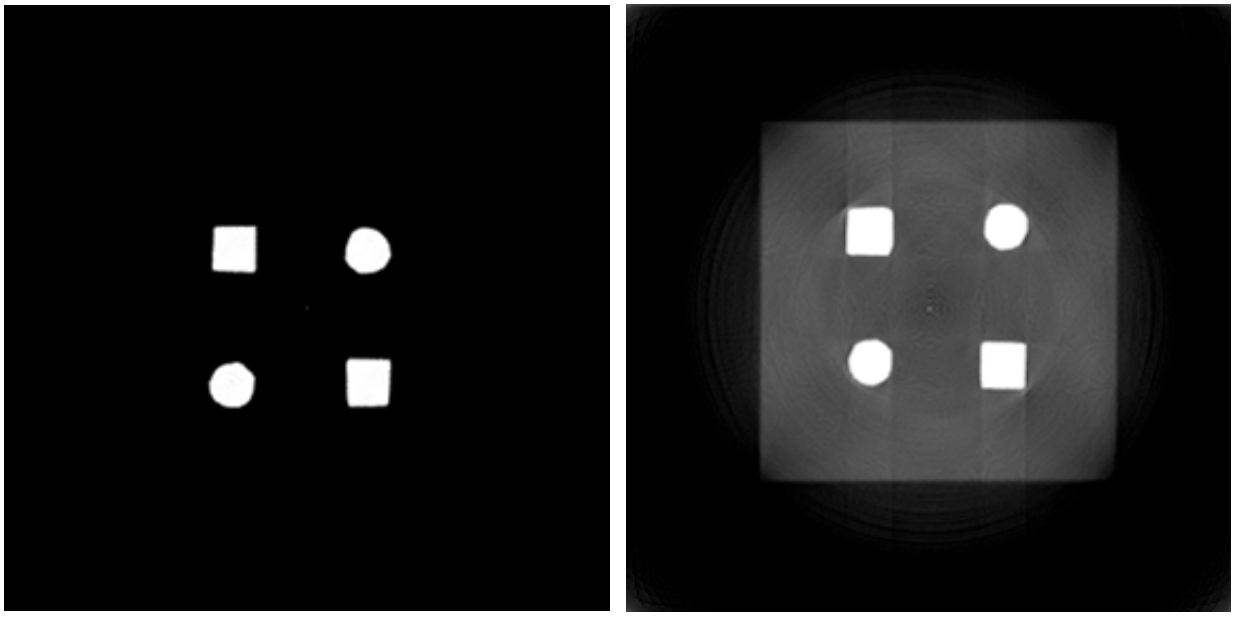

(a) (b)

Fig. 4.7 The results of applying the algorithm to the experimental sample A: (a) is the extraction result of metal regions, and (b) is the result of synthesis.

4.2.2 The experimental sample B

The experimental sample B (Fig. 4.8) is the resin sample in which nine metal cylinders are embedded. The projection conditions are shown in Table. 4.2, and the conventional FBP result is shown in Fig. 4.9. Fig. 4.10(a) is the extraction result of metal regions, and Fig. 4.10(b) is the result of synthesis. Metal artifacts are significantly reduced as with the result of the experimental sample A by applying our reconstruction algorithm.

Table 4.2: Projection conditions of the experimental sample B.

Component materials	Resin, iron
Number of metallic objects	9
X-ray tube voltage [kV]	76
X-ray tube current [μA]	67
Number of pixels	512×512
Field of view [mm]	ϕ 25.0
Number of projections	800
Each projection time [s]	0.53

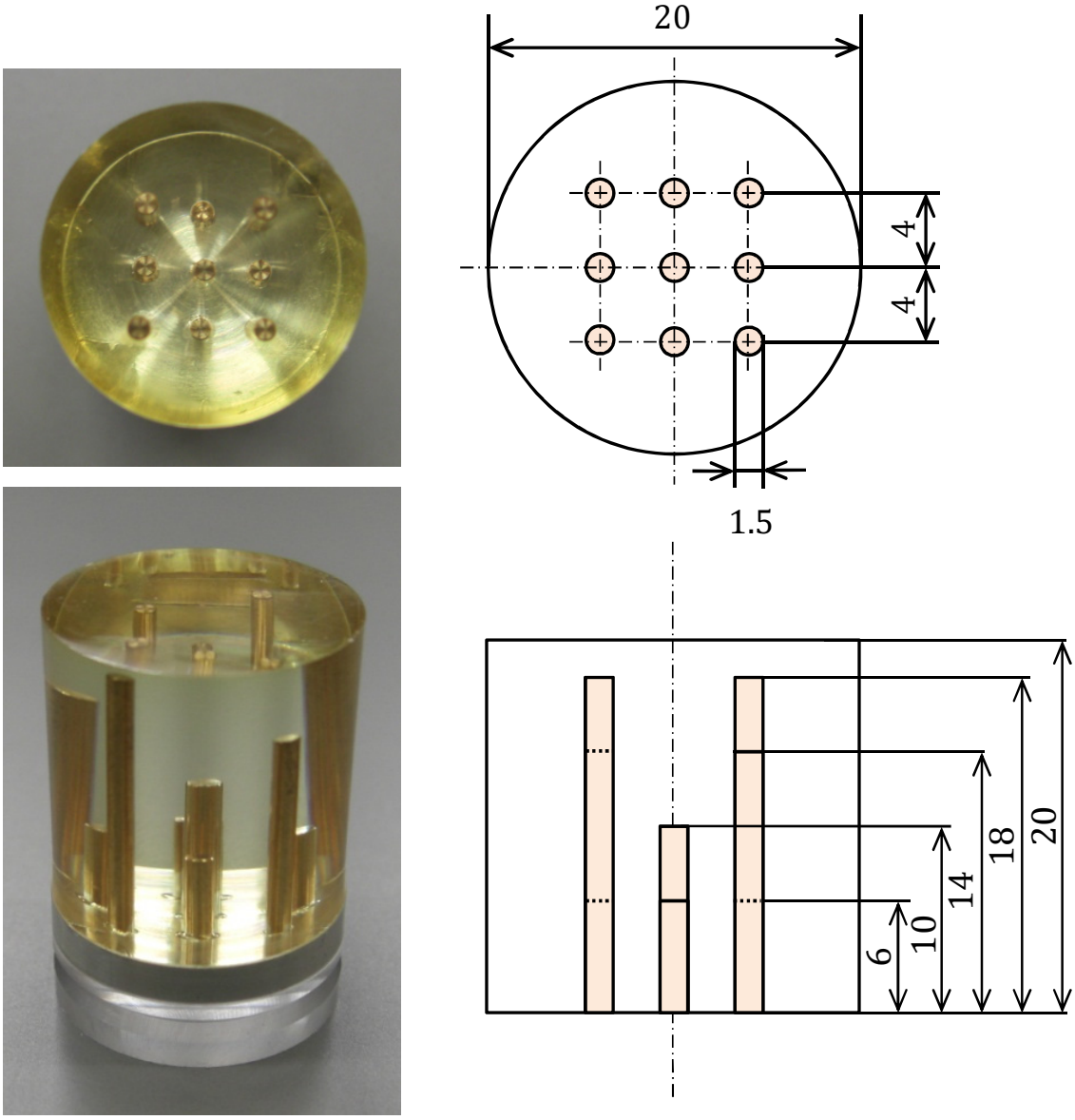

Fig. 4.8: The experimental sample B.

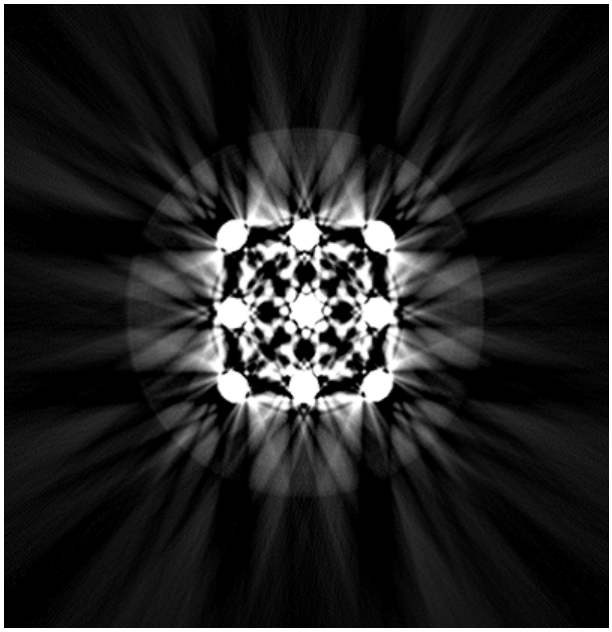

Fig. 4.9: The FBP result of the experimental sample B.

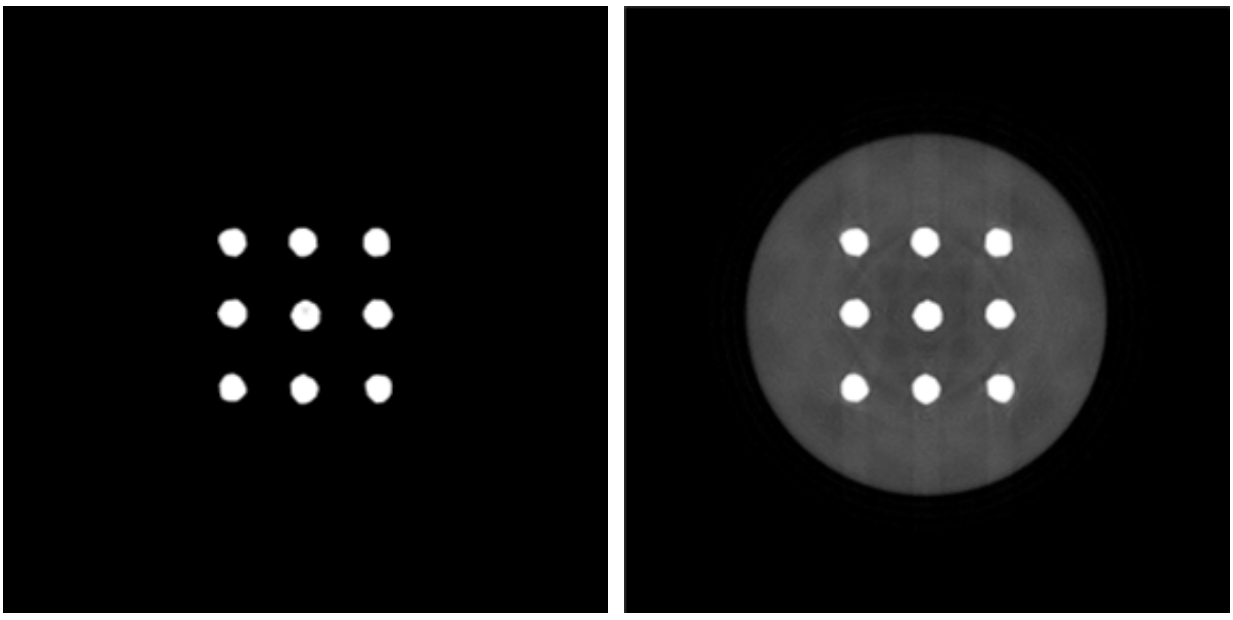

(a) (b)

Fig. 4.10 The results of applying the algorithm to the experimental sample B: (a) is the extraction result of metal regions, and (b) is the result of synthesis.

4.2.3 The experimental sample C

The experimental sample C (Fig. 4.11) is the resin sample in which a cross-shaped copper pole is embedded. The projection conditions are shown in Table. 4.3, and the conventional FBP result is shown in Fig. 4.12. Fig. 4.13(a) is the extraction result of metal regions, and Fig. 4.13(b) is the result of synthesis. Although the corners of metals were rounded, the shape was reconstructed almost exactly. Also, in Fig. 4.13(b), there remains more artifacts than the result of the experimental sample A and B. From this fact, it is expected that applying our algorithm to objects that includes concave portions such as the experimental sample C is relatively difficult.

Table 4.3: Projection conditions of the experimental sample C.

Component materials	Resin, copper
Number of metallic objects	1
X-ray tube voltage [kV]	80
X-ray tube current [μA]	54
Number of pixels	512×512
Field of view [mm]	ϕ 25.8
Number of projections	800
Each projection time [s]	1.07

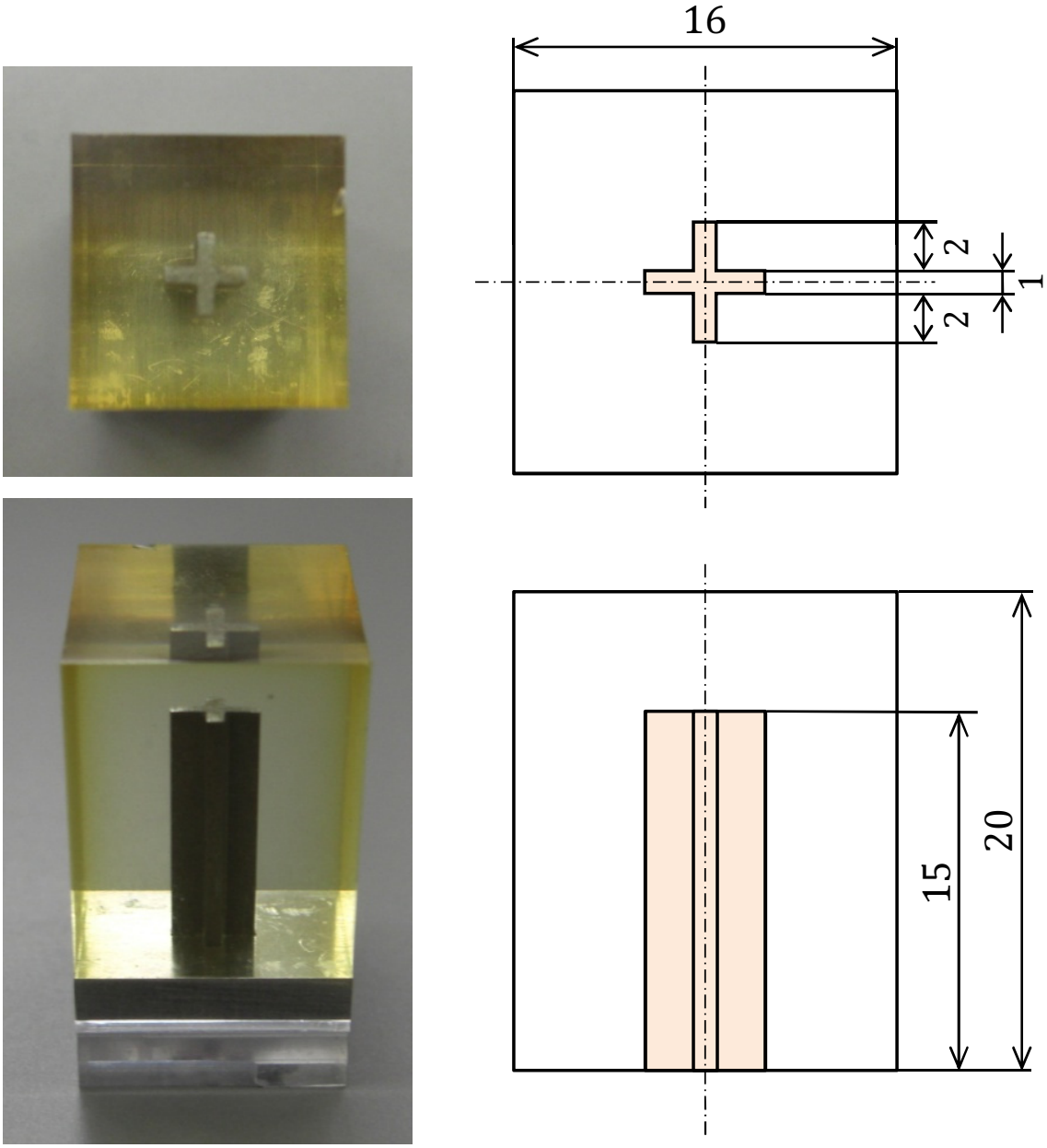

Fig. 4.11: The experimental Sample C.

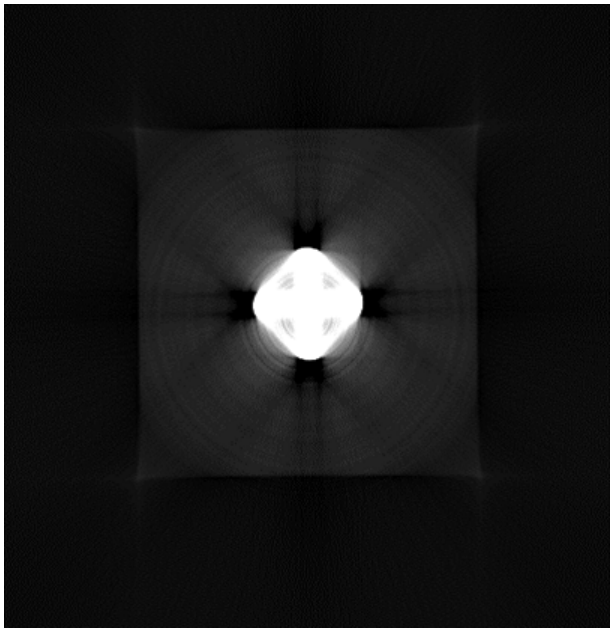

Fig. 4.12: The FBP result of the experimental sample C.

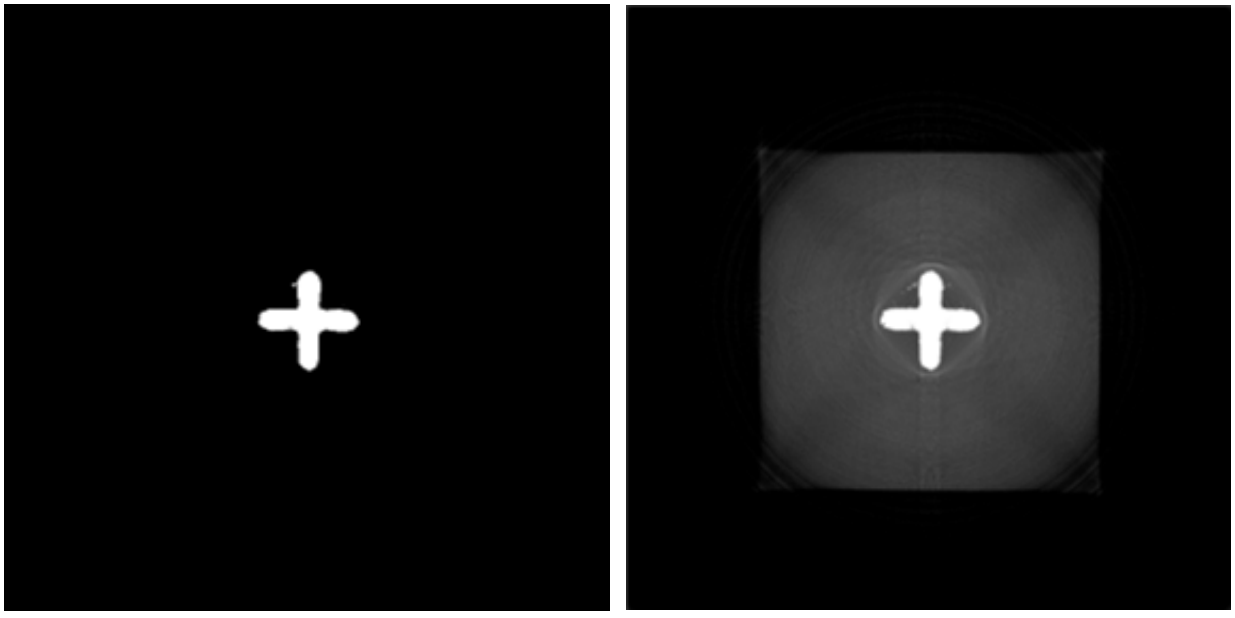

(a) (b)

Fig. 4.13 The results of applying the algorithm to the experimental sample C: (a) is the extraction result of metal regions, and (b) is the result of synthesis.

4.2.4 The experimental sample D

The experimental sample D (Fig. 4.2.4) is composed of a resin container, resin beads, and five iron nails. The projection conditions are shown in Table. 4.4, and the conventional FBP result is shown in Fig. 4.15. Fig. 4.16(a) is the extraction result of metal regions, and Fig. 4.16(b) is the result of synthesis. Metal artifacts were significantly reduced, however, some artifacts remain and the image is slightly blurred especially in peripheral portions of the nails.

Table 4.4: Projection conditions of the experimental sample D.

Component materials	Resin, iron
Number of metallic objects	5
X-ray tube voltage [kV]	70
X-ray tube current [μA]	90
Number of pixels	640×640
Field of view [mm]	ϕ 45.8
Number of projections	800
Each projection time [s]	2.13

Fig. 4.14: The experimental sample D.

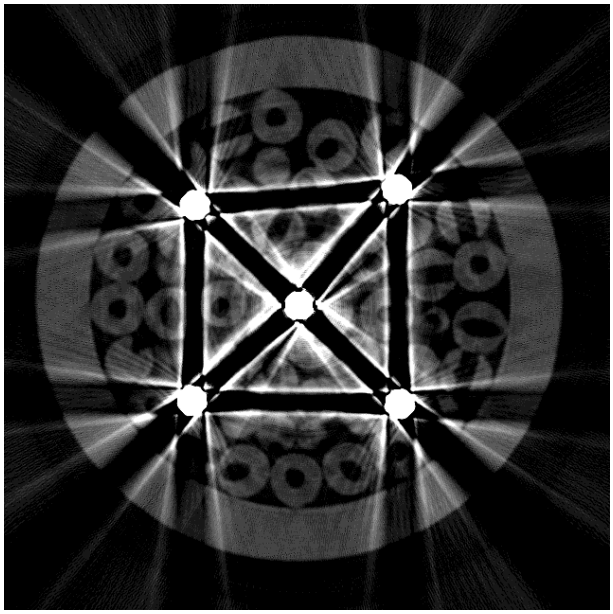

Fig. 4.15: The FBP result of the experimental sample D.

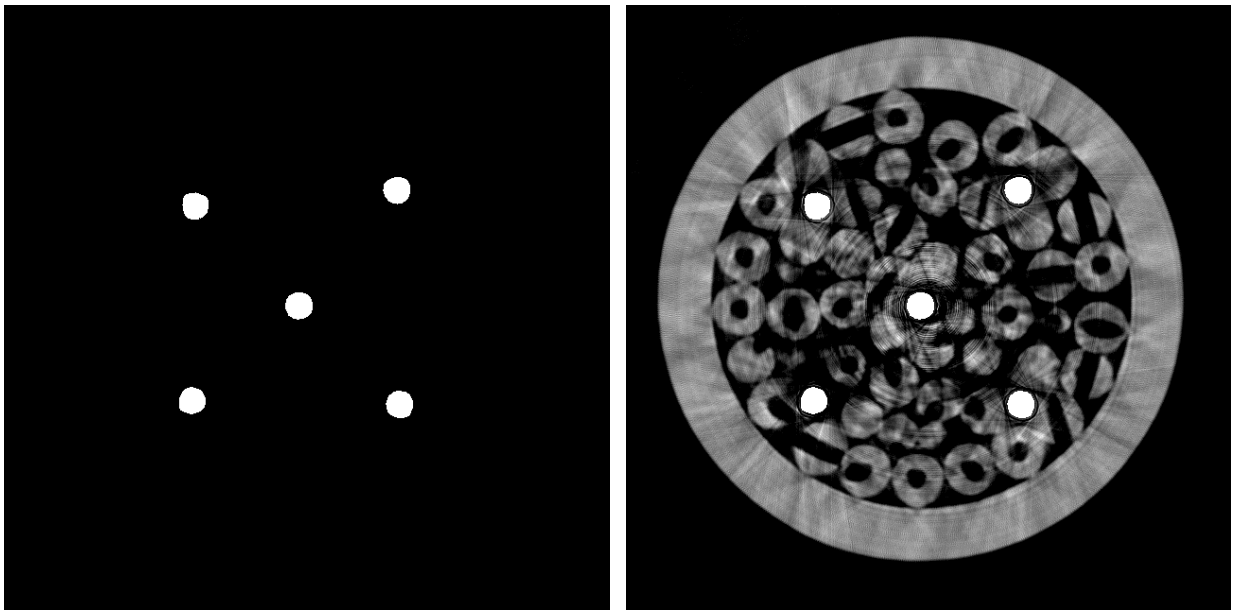

(a) (b)

Fig. 4.16 The results of applying the algorithm to the experimental sample D: (a) is the extraction result of metal regions, and (b) is the result of synthesis.

4.3 Application to simulation data (MAR1)

In the previous section, we prepared simple experimental samples that are composed resins and metals, and confirmed the effects of our algorithm. In this section, more complex situations are prepared assuming actual diagnoses and inspections using simulation techniques. Metal artifacts were generated from metal teeth, and the surrounding area of metals especially gum regions became blurred.

4.3.1 The tooth phantom

We first created the tooth phantom, which is composed of three materials: a gum, teeth, metals (Fig. 4.17). The projection conditions in the simulation are showin in Table. 4.5, and the conventional FBP result is shown in Fig. 4.18. Metal artifacts were generated from metal teeth, and the surrounding area of metals especially gum regions became blurred.

Fig. 4.19 is the raw sinogram of the tooth phantom, and Fig. 4.20 is the interpolated sinogram. We see that the non-metal interpolation was performed naturally. Fig. 4.21(a) is the extraction result of metal regions, and Fig. 4.21(b) is the result of synthesis. Although metal artifacts around tooth regions remained, metal artifacts were significantly reduced. This result implies that our algorithm can be applied complex situations that are composed of three or more materials.

Table 4.5: Simulation conditions of the tooth phantom.

Component materials	Soft tissue, bone, iron
Number of metallic objects	2
Number of pixels	512×512
Field of view [mm]	ϕ 30.7
Number of projections	800

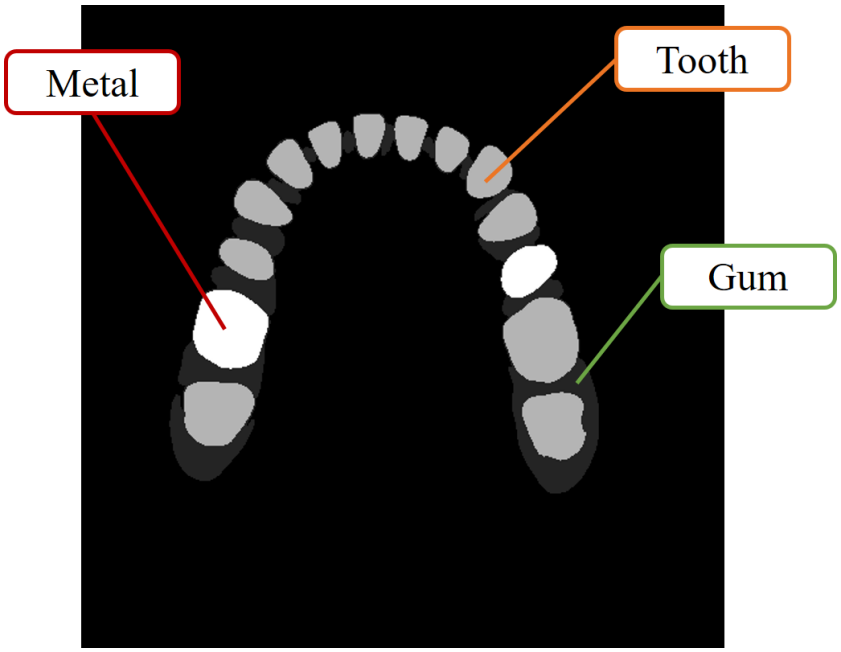

Fig. 4.17: The numerical tooth phantom.

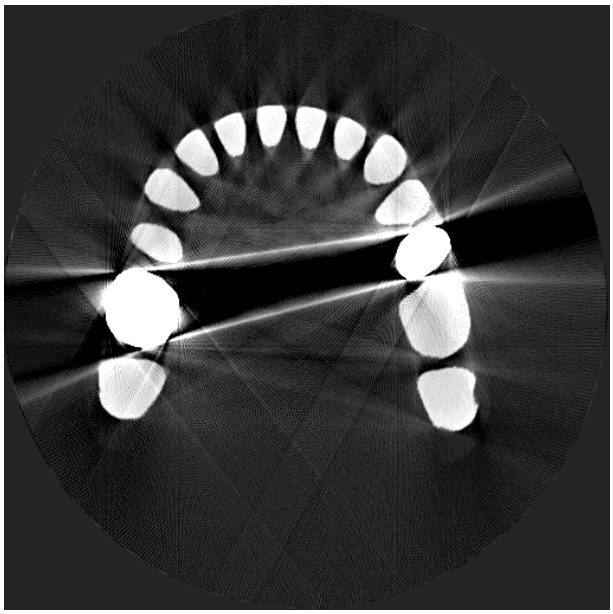

Fig. 4.18 The FBP result of the numerical tooth phantom (RMSE = 52.324, SSIM = 0.71185).

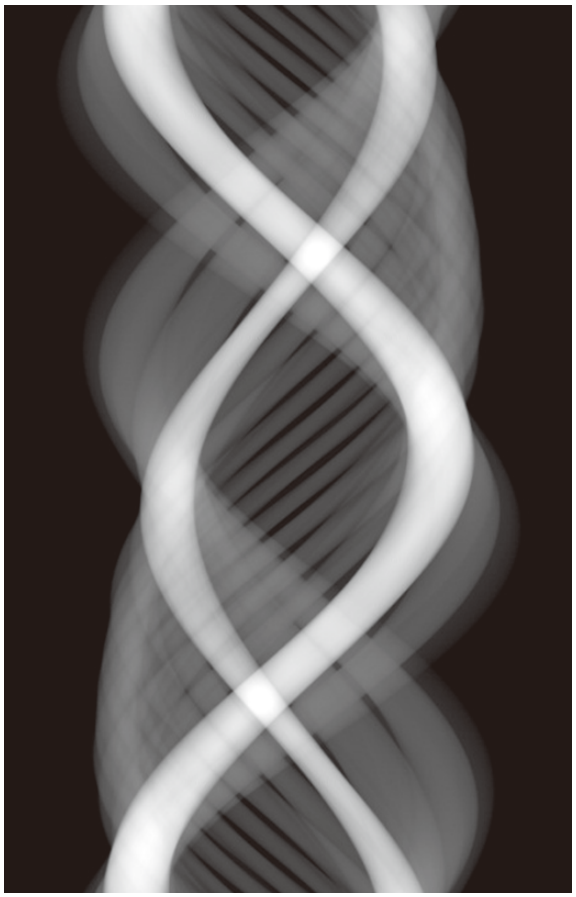

Fig. 4.19: The raw sinogram.

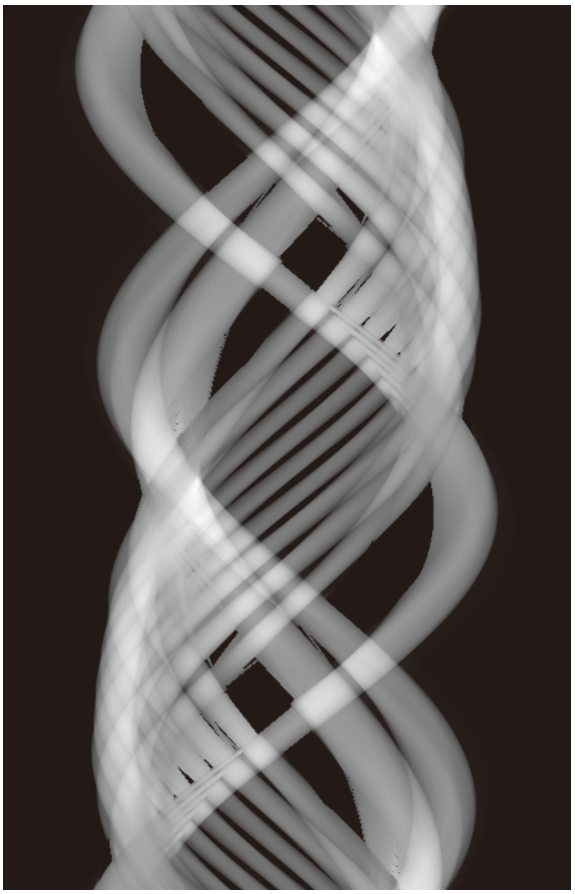

Fig. 4.20: The interpolated sinogram.

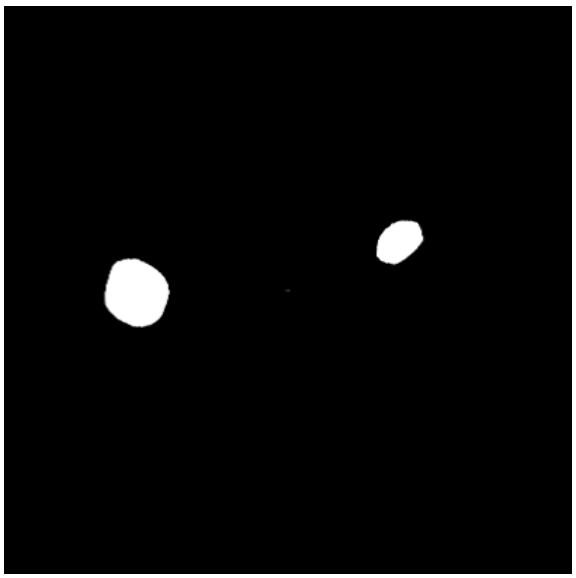

(a)

(b) RMSE = 23.976, SSIM = 0.83303

Fig. 4.21 The results of applying the algorithm to the tooth phantom: (a) is the extraction result of metal regions, and (b) is the result of synthesis.

4.3.2 The head phantom

Next we created the head phantom, which is composed of various materials (Fig. 4.22). Ten iron bolts are assumed as embedded metal materials. A total of ten iron bolts are embedded in this phantom. The projection conditions in the simulation are shown in Table. 4.6, and the conventional FBP result is shown in Fig. 4.23. Strong metal artifacts were generated from metal regions, and the surrounding area of metals became blurred.

Fig. 4.24 is the raw sinogram of the head phantom, and Fig. 4.25 is the interpolated sinogram. The interpolated result looks smooth, but it's also looks unnatural. It can be considered that the naturalness depends on the complexity of the non-metal regions. Fig. 4.26(a) is the extraction result of metal regions, and Fig. 4.26(b) is the result of synthesis. Metal artifacts around metals remained, and some organs became blurred. In fact, although most of the metal artifacts were reduced, it is difficult to confirm the eyeballs and the optic nerves from the result.

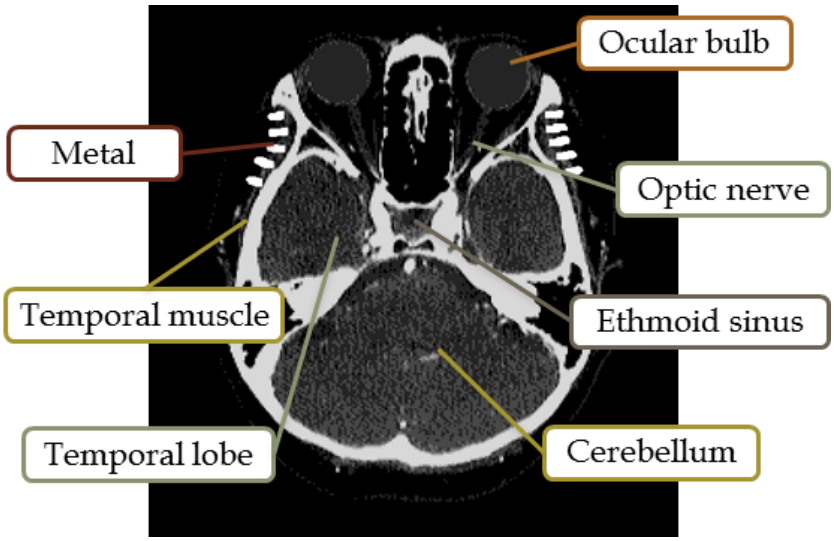

Fig. 4.22: The numerical head phantom.

Table 4.6: Simulation conditions of the head phantom.

Component materials	Soft tissue, hard tissue, bone, iron
Number of metallic objects	2
Number of pixels	512×512
Field of view [mm]	ϕ 30.7
Number of projections	800

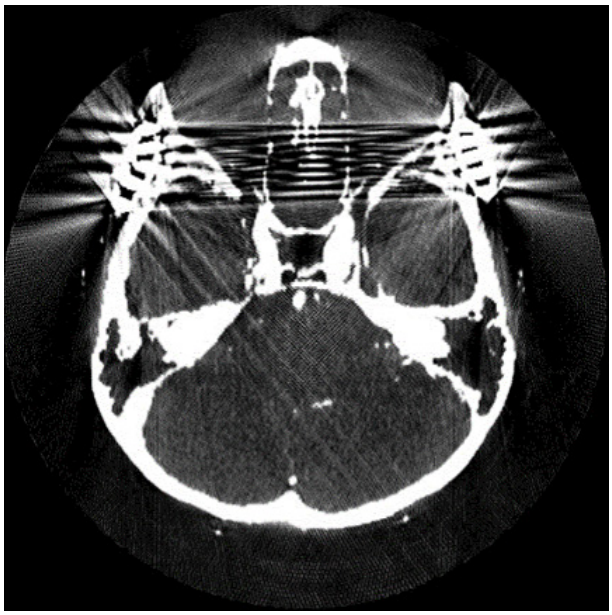

Fig. 4.23 The FBP result of the numerical head phantom (RMSE = 57.686, SSIM = 0.79036).

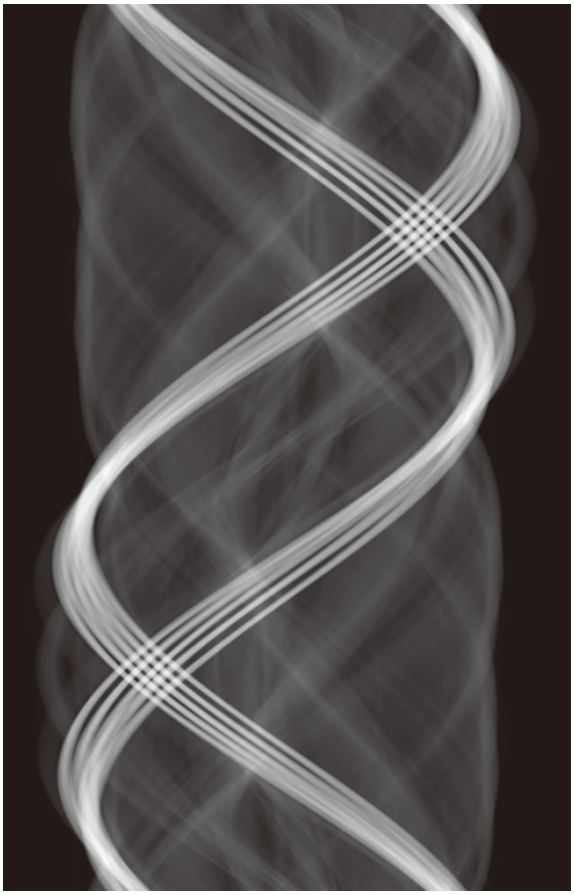

Fig. 4.24: The sinogram.

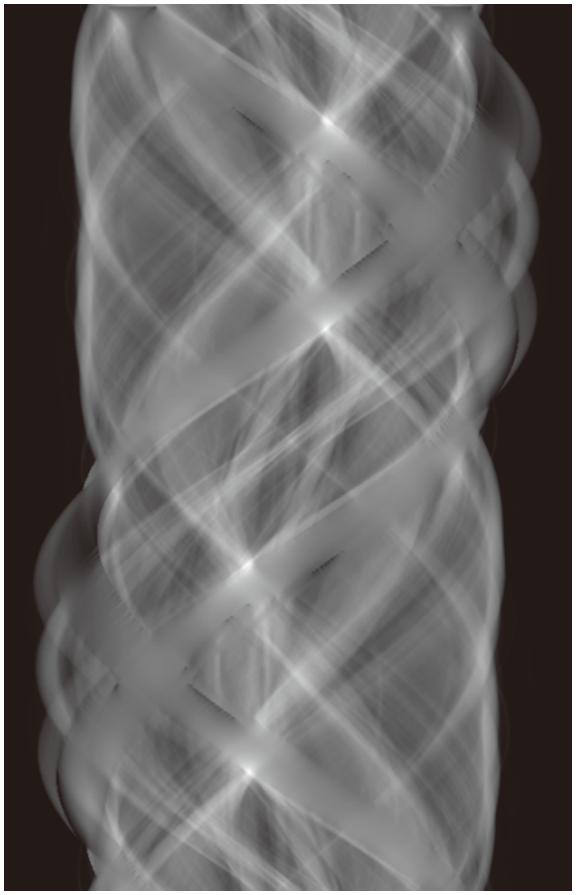

Fig. 4.25: The interpolated sinogram.

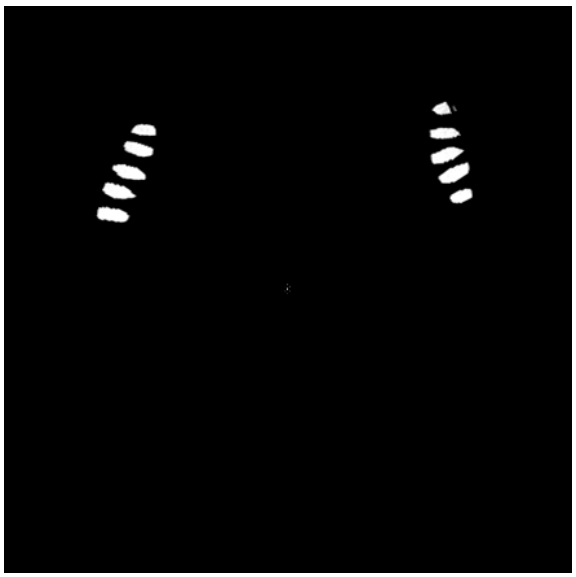

(a)

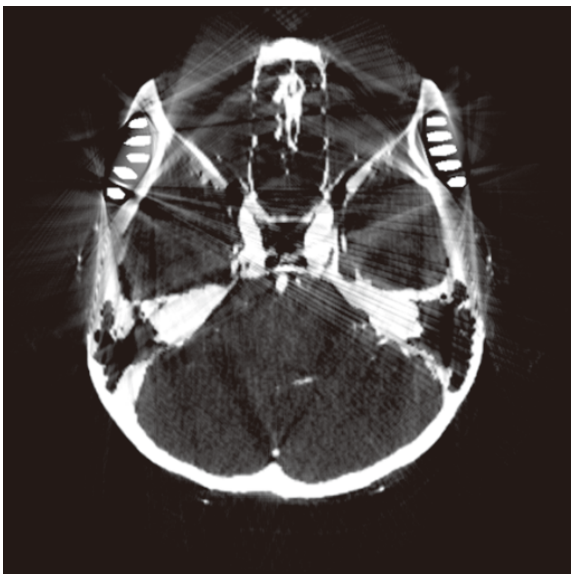

(b) RMSE = 34.920, SSIM = 0.86574

Fig. 4.26 The results of applying the algorithm to the head phantom: (a) is the extraction result of metal regions, and (b) is the result of synthesis.

4.3.3 The stomach phantoms

At the end of this section, we created the stomach phantoms. The basic phantom without metals is shown in Fig.Fig. 4.27. This phantom is composed of several organs, and a lesion part on the liver that is assumed liver abscess. The projection conditions in the simulation are shown in Table. 4.7. In the following, simulation experiments are conducted while adding metals to this phantom.

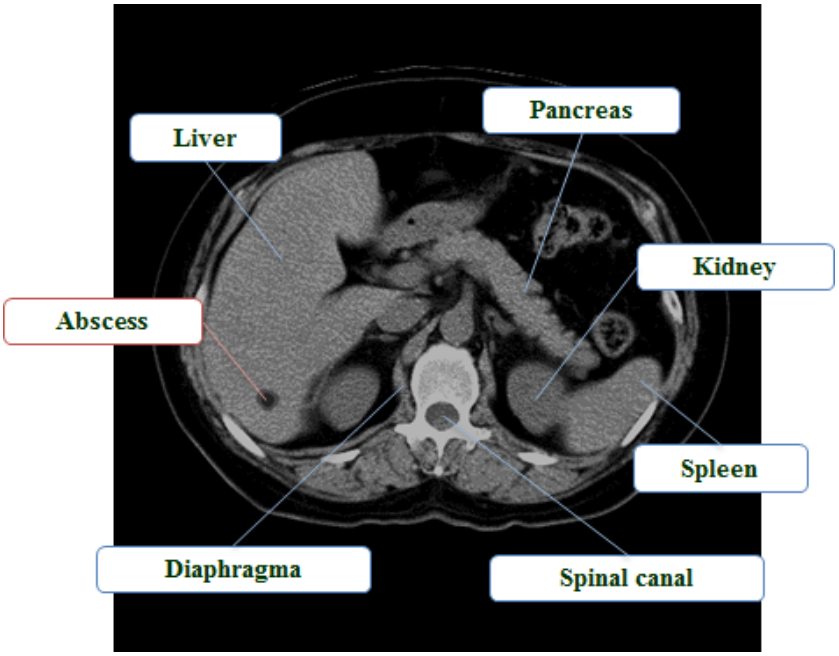

Fig. 4.27: The basic stomach phantom.

Table 4.7: Simulation conditions of the stomach phantoms.

Component materials	Soft tissue, hard tissue, bone, iron
Number of metallic objects	2 to 11
Number of pixels	512×512
Field of view [mm]	ϕ 61.4
Number of projections	800

The stomach phantom A

The stomach phantom A, in which three objects made of iron are embedded, is shown in Fig. 4.28, and the conventional FBP result is shown in Fig. 4.29(a). Metal artifacts were generated, and the lesion part became unclear. The result of applying our algorithm is shown in Fig. 4.29(b). Since metal artifacts were significantly reduced, the lesion part and the cross-sectional shape are observed clearly. Next, to check the performance limit of this method, metals are added.

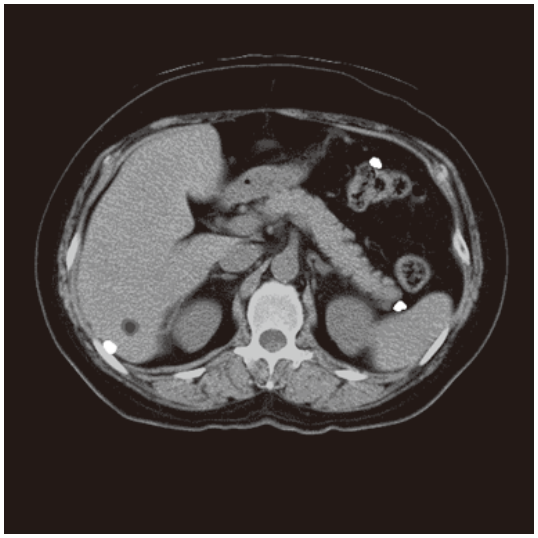

Fig. 4.28: The stomach phantom A.

(a) RMSE = 44.359, SSIM = 0.84765

(b) RMSE = 20.017, SSIM = 0.90395

Fig. 4.29 Application results to the stomach phantom A. (a) is the FBP result, and (b) is the improved result.

The stomach phantom B

The stomach phantom B, in which six objects made of iron are embedded, is shown in Fig. 4.30, the conventional FBP result is shown in Fig. 4.31(a), and the result of applying our algorithm is shown in Fig. 4.31(b). The conventional result shows the generation of strong metal artifacts. By applying out algorithm, metal artifacts were reduced and the cros-sectional shape became clear, but more artifacts remained as compared to Fig. 4.29(b).

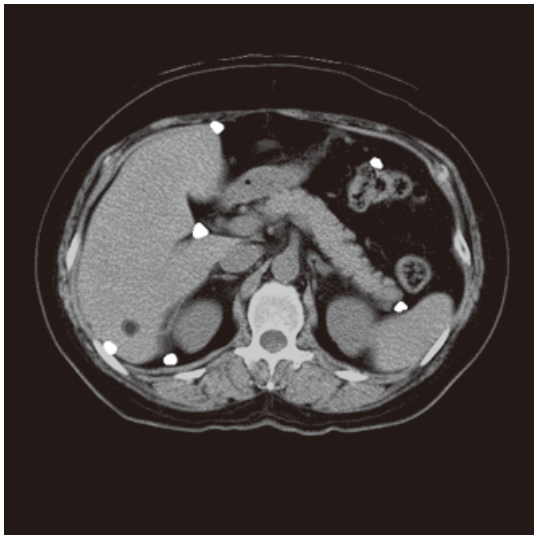

Fig. 4.30: The stomach phantom B.

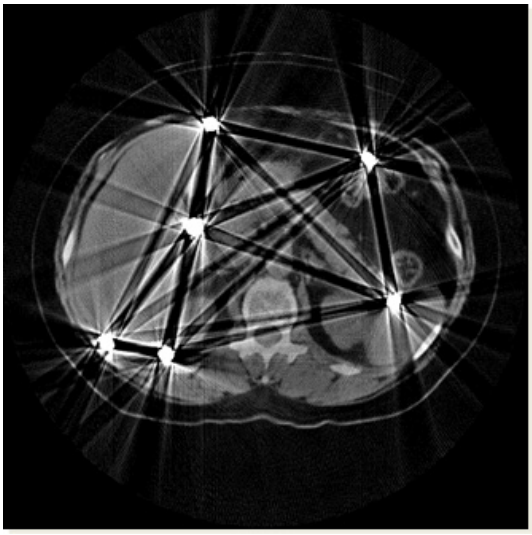

(a) RMSE = 36.63287, 0.77800

(b) RMSE = 20.30449, SSIM = 0.90113

Fig. 4.31 Application results to the stomach phantom B. (a) is the FBP result, and (b) is the improved result.

The stomach phantom C

The stomach phantom C, in which eleven objects made of iron are embedded, is shown in Fig. 4.32, the conventional FBP result is shown in Fig. 4.33(a), and the result of applying our algorithm is shown in Fig. 4.33(b). Terrible metal artifacts were generated in the conventional result. Out algorithm reduced the metal artifact indeed, however, several organs became blurred and it's difficult to observe the lesion part.

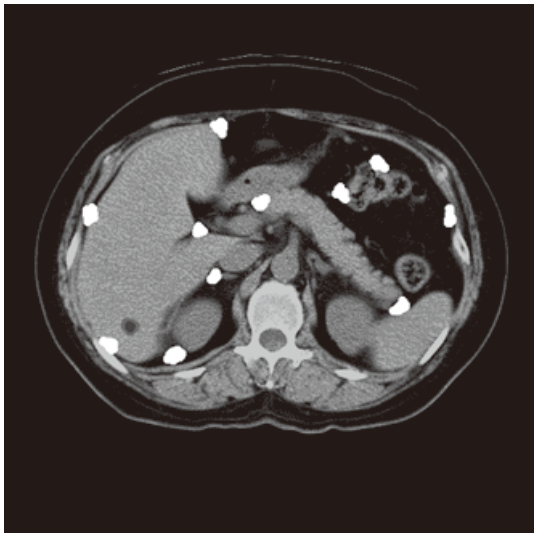

Fig. 4.32: The stomach phantom C.

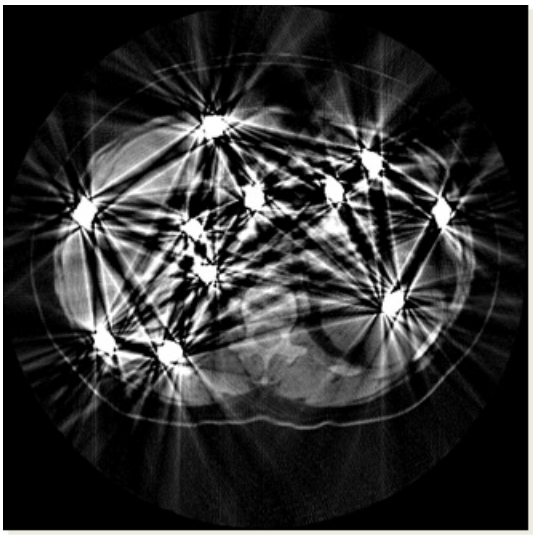

(a) RMSE = 54.884, SSIM = 0.77132

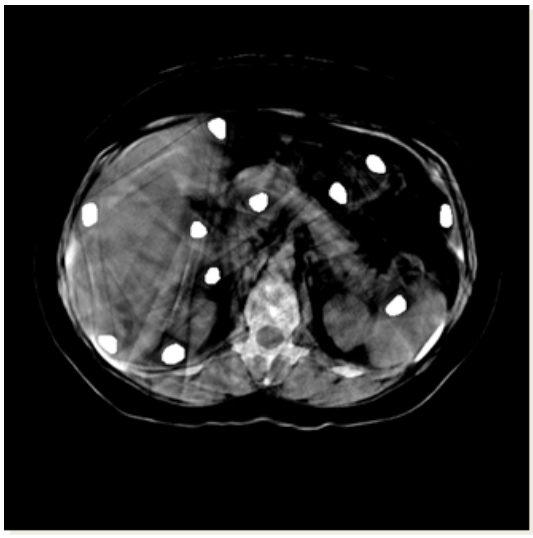

(b) RMSE = 24.241, SSIM = 0.89363

Fig. 4.33 Application results to the stomach phantom C. (a) is the FBP result, and (b) is the improved result.

The stomach phantom D

The stomach phantom D, in which four large objects made of iron are embedded, is shown in Fig. 4.34, the conventional FBP result is shown in Fig. 4.35(a), and the result of applying our algorithm is shown in Fig. 4.35(b). The effect of our algorithm can be confirmed, and the lesion part is barely able to be observed. However, organ shapes became blurred, especially in around the metal regions.

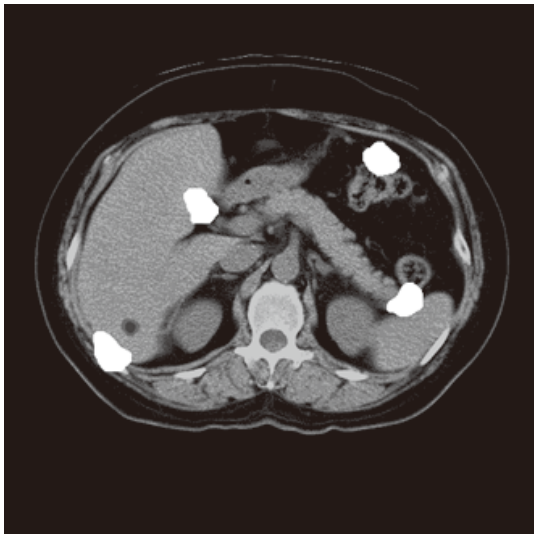

Fig. 4.34: The stomach phantom D.

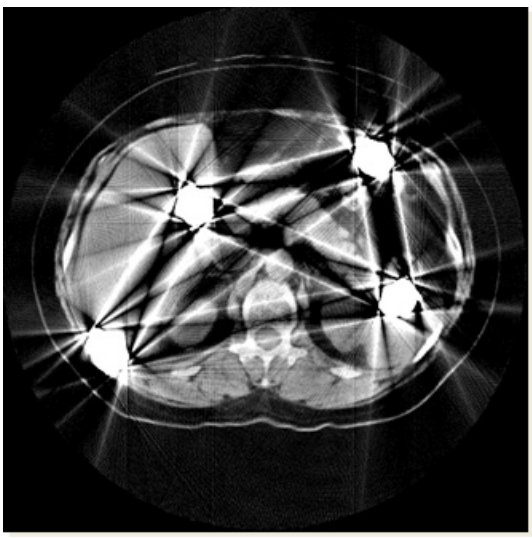

(a) RMSE = 55.203, 0.77932

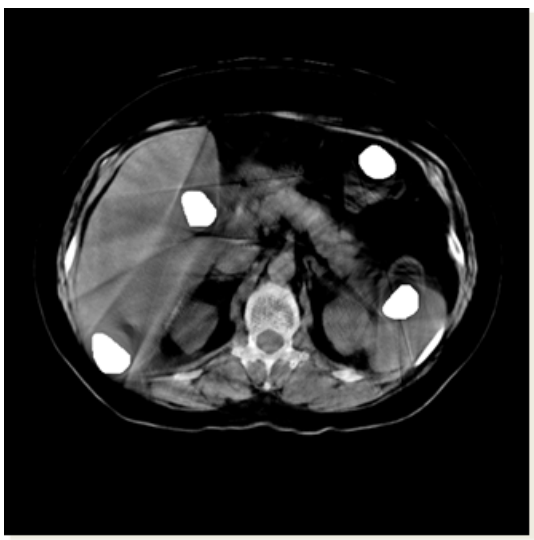

(b) RMSE = 21.108, SSIM = 0.90206

Fig. 4.35 Application results to the stomach phantom D. (a) is the FBP result, and (b) is the improved result.

The stomach phantom E

The stomach phantom E, in which four larger objects made of iron than the stomach phantom D are embedded, is shown in Fig. 4.36, the conventional FBP result is shown in Fig. 4.37(a), and the result of applying our algorithm is shown in Fig. 4.37(b). Metal artifacts were reduced, however, the image became totally blurred, and it's impossible to observe the lesion part. In addition, the corners of the metals are rounded.

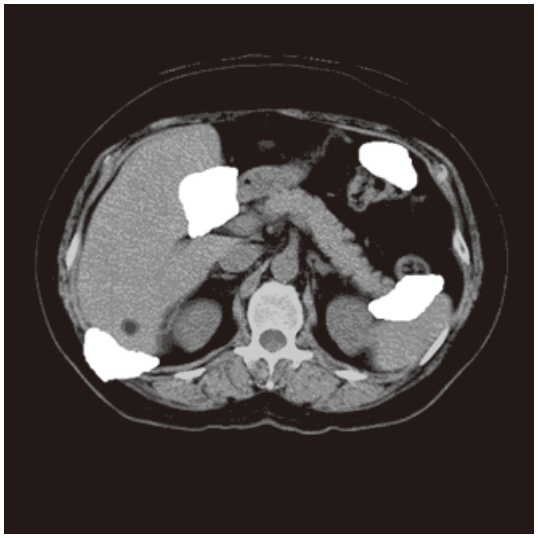

Fig. 4.36: The stomach phantom E.

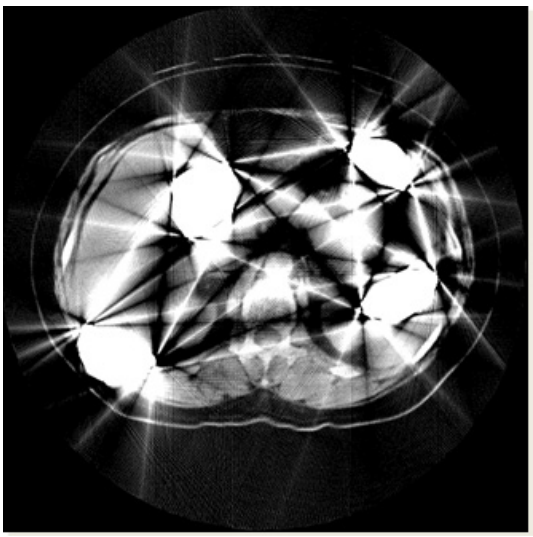

(a) RMSE = 64.848, SSIM = 0.78587

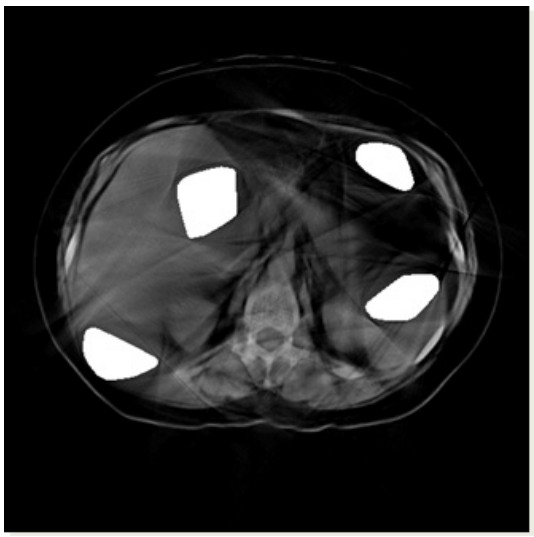

(b) RMSE = 24.060, SSIM = 0.88598

Fig. 4.37 Application results to the stomach phantom E. (a) is the FBP result, and (b) is the improved result.

Chapter 5

Metal artifact reduction based on iterative reconstruction

Chapter 5: Metal artifact reduction based on iterative reconstruction

In Chapter 4, the metal artifact reduction method based on sine curve has been proposed. However, metal artifacts surrounding area of metals were remained, especially in the cases of complex simulation. In this chapter, we propose a novel reconstruction algorithm to reduce metal artifacts based on iterative reconstruction.

5.1 Metal artifact reduction method 2 (MAR2)

In iterative reconstruction, metal artifact factors are not only back projection, but also forward projection calculation that doesn't consider energy spectrum. In order to solve calculation discrepancy, we propose the following method:

1. After FBP is applied, extract metal region from the reconstruction image by using threshold processing or method based on sine curves. Then use the metal image as a initial image in iterative calculations.

2. Prepare a forward projection calculation equation that includes energy dependence, and apply iterative reconstruction.

The flow chart of this method is shown in Fig. 5.1. In the process (1), an extracted metal image is used as a initial image. In most cases, metal regions can be extracted by using thresholding or method based on sine curves. In the process (2), by applying iterative reconstruction that includes energy dependence, it could be solve discrepancies in calculations. The reason why we firstly extract metal regions is to accelerate the convergence of images and to prevent from the divergence. Furthermore, we assumed that metals are reconstructed accurately before iterative calculations, and didn't perform feed back to metal regions during the calculations.

The repetitive equation of ART that includes energy dependence is expressed as follows

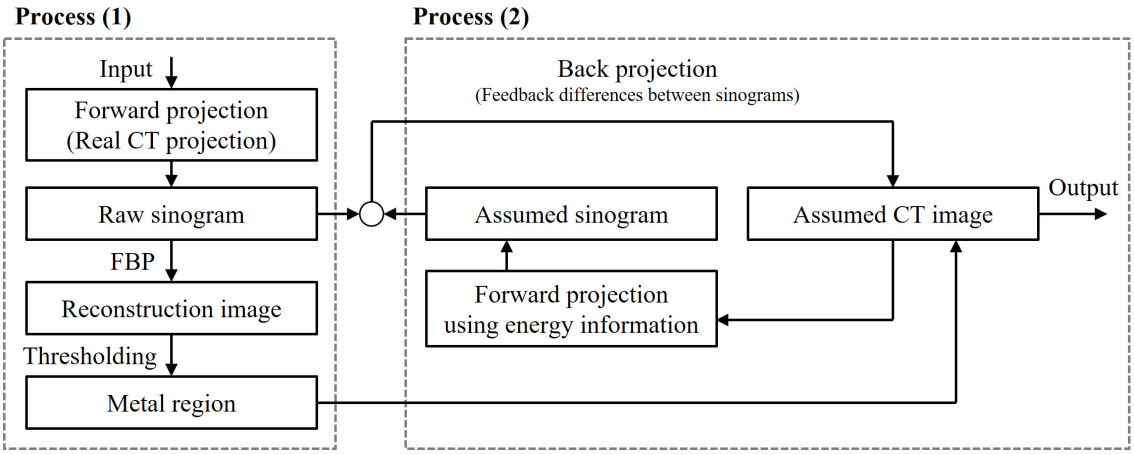

Fig. 5.1: The flow chart of E-ART.

by modifying the Eqn. 2.25.

$$\mu(x,y,E)^{(k+1)} = \mu(x,y,E)^{(k)} + \left\{ p(X,\theta_k) + \ln \frac{\displaystyle\int_E I_{\text{in}}(X,\theta_k,E) \exp\left(-\int_{-\infty}^{\infty} \mu(x,y,E)^{(k)} dY \right) EdE}{\displaystyle\int_E I_{\text{in}}(X,\theta_k,E) EdE} \right\} d\theta. \tag{5.1}$$

In this study, we call ART that includes energy dependence E-ART.

5.1.1 Assumption of X-ray attenuation coefficients

In order to perform forward projection calculation considering energy dependence, X-ray attenuation coefficients $\mu(E)$ corresponding to each energy E of each material are required. X-ray attenuation coefficients of some elements calculated by literature values [23] are shown in Fig. 5.2. In actual iterative calculations, we have to prepare X-ray attenuation coefficients $\mu_v(E)$ corresponding to image densities v. Therefore, we propose an equation that can create X-ray attenuation coefficients assuming the Fig. 5.2 by using only an X-ray attenuation coefficient of a metal $\mu_{\text{Metal}}(E)$.

$$\mu_v(E) = \mu_{\text{Metal}}(E) \times \frac{\alpha^v - 1}{\alpha^{n-1} - 1} \quad (0 \leq v \leq n-1, 1 < \alpha), \tag{5.2}$$

where α is the coefficient corresponding to the dispersion of the density distribution, and n is the number of density gradation. As α becomes larger, the density of X-ray attenuation

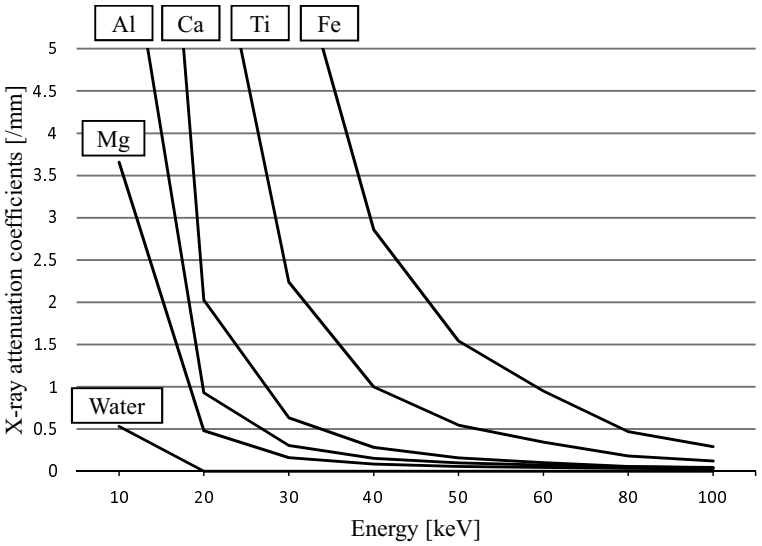

Fig. 5.2: The X-ray attenuation coefficients of the real elements [23].

coefficients around non-metal becomes higher. As α approaches 1, the density of X-ray attenuation coefficients from non-metals through metals becomes uniformly-distributed. Thus, by changing the assigned density of X-ray attenuation coefficients, the iterative calculations could be suitable for the distribution of materials that present in the cross-sectional. For example, when the subject does not contain hard materials except metals, a large amount of X-ray attenuation coefficients of non-metals make the iterative calculations easier to converge.

The results of calculating X-ray attenuation coefficients μ_v $(0 \leq v \leq 255)$ from Eqn. 5.2 in the case of $n = 256$ is shown in Fig. 5.3. These figures show the coefficients of μ_{16i} $(0 \leq i \leq 15)$ and μ_{255} $(= \mu_{\mathrm{Metal}})$. We see that the distribution of X-ray attenuation coefficients slants toward non-metal sides as α becomes larger, while the distribution becomes uniformly-distributed as α approaches 1. This results also show that the X-ray attenuation coefficients assumed by Eqn. 5.2 could simulate actual X-ray attenuation coefficients shown in Fig. 5.2. To find an optimal alpha value, SLP that was introduced in chapter 3 is available. When the SLP value became the highest, α would also become optimal value and metal artifact would be reduced effectively.

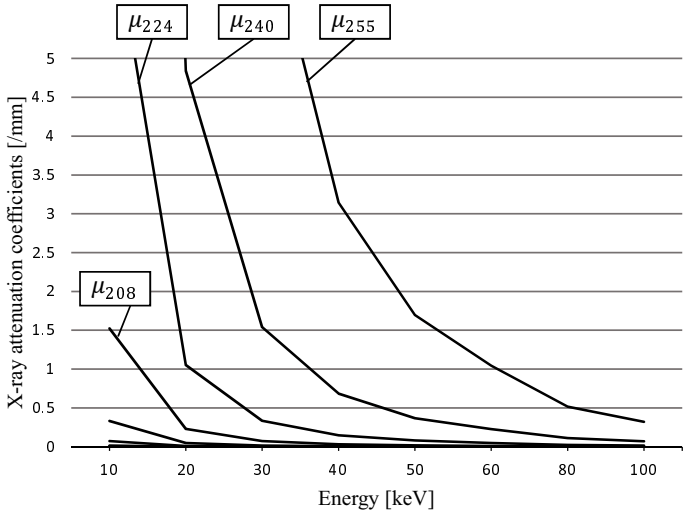

(a) $\alpha = 1.10$

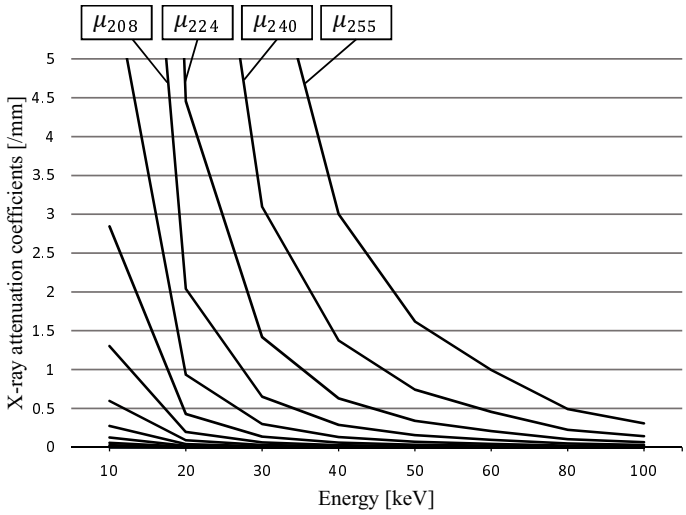

(b) $\alpha = 1.05$

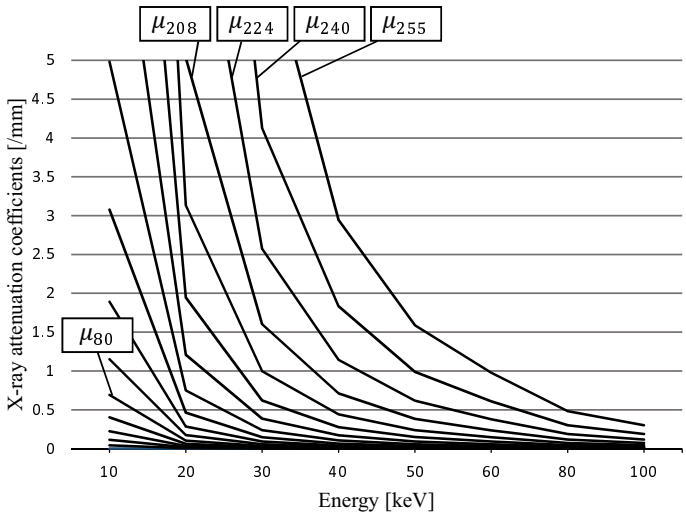

(c) $\alpha = 1.03$

Fig. 5.3: Assumptions of X-ray attenuation coefficients by Eqn. 5.2.

5.2 Application to CT data (MAR2)

Fig. 5.4 shows changes of SLP when applying E-ART to the experimental sample D while changing α values. Since the maximum value of SLP is 8546.8 at $\alpha = 1.036$, this point is considered as the optimal value. The E-ART results for each α are shown in Fig. 5.5 We see that metal artifacts decrease with α changing from 1.010 to 1.036, and metal artifact increase with α changing from 1.036 to 1.100. These results demonstrate that the quantitative evaluation of metal artifacts by using SLP corresponds to qualitative evaluations.

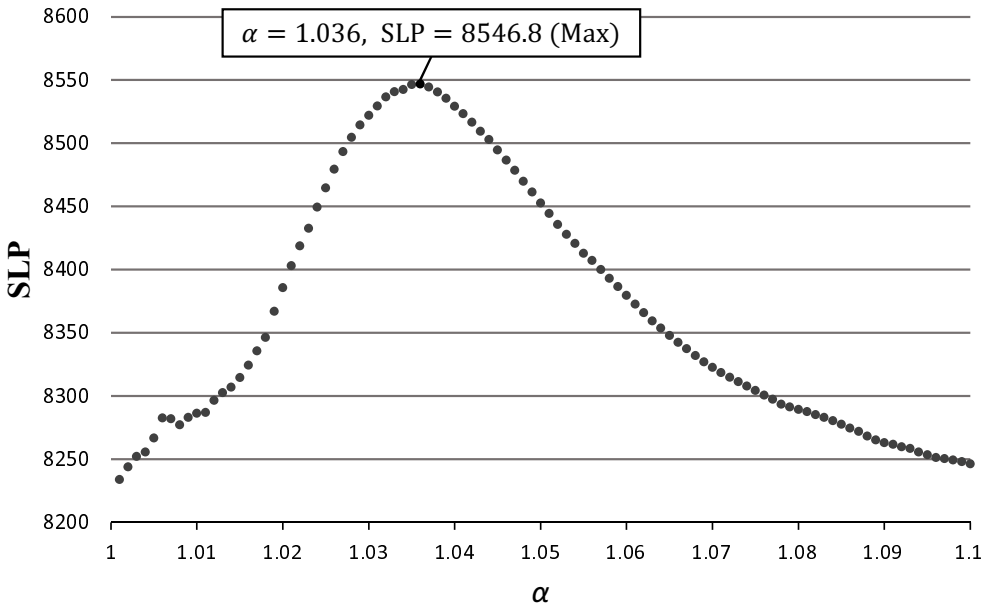

Fig. 5.4: Changes of SLP.

The results shown in Fig. 5.5 were generated by applying E-ART that the iteration number is one. We then applied E-ART five times at $\alpha = 1.036$, which seems the optimal value, and the result is shown in 5.6(a). This result and Fig. 5.5(c) look the same, but the outline of resins were emphasized, and SLP also rose to 8655.8. The result of applying the metal artifact reduction method based on sine curves is shown again in Fig. 5.6(b). Metal artifacts were reduced as well, however, the contrast resolution of non-metal regions became worse. The SLP values is 8414.4, and this implies that the method based on iterative reconstruction is more effective than the one based on sine curves.

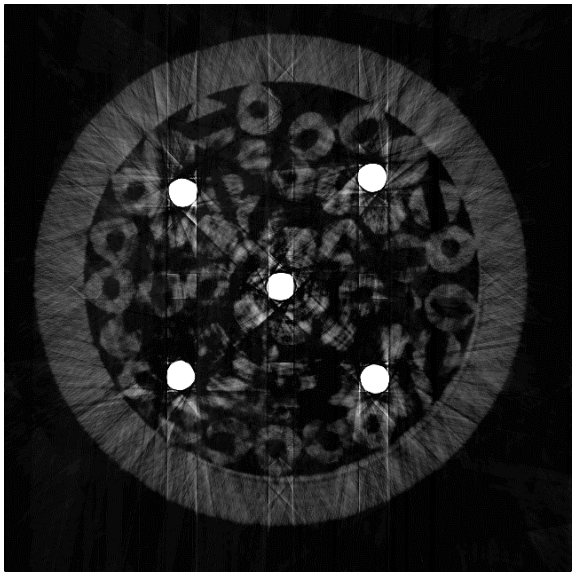

(a) $\alpha = 1.010, \mathrm{SLP} = 8286.3$

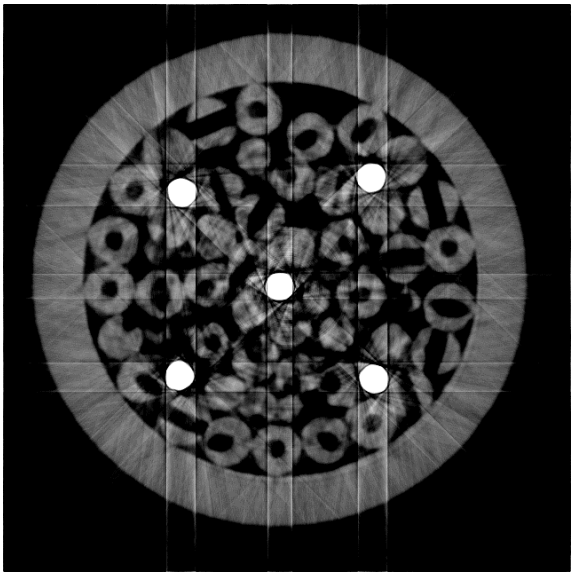

(b) $\alpha = 1.020, \mathrm{SLP} = 8418.8$

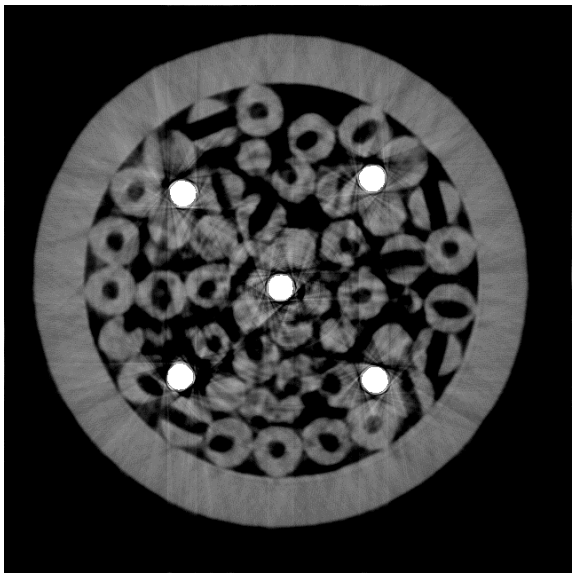

(c) $\alpha = 1.036, \mathrm{SLP} = 8546.8$

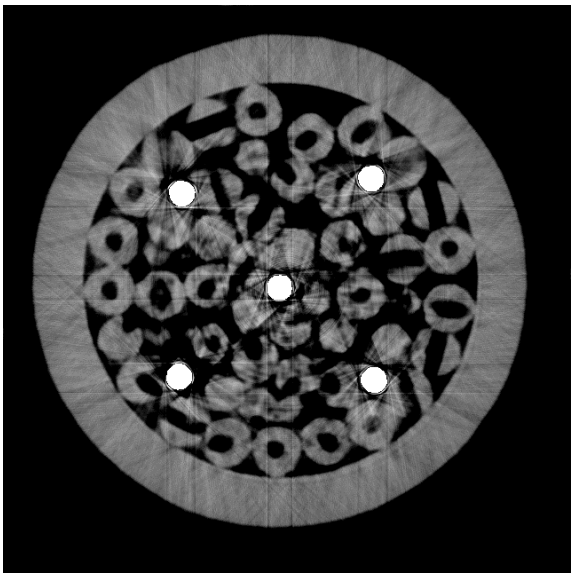

(d) $\alpha = 1.050, \mathrm{SLP} = 8452.7$

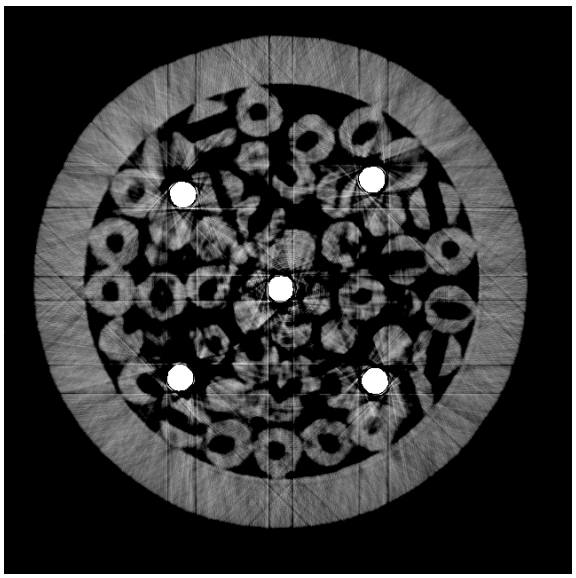

(e) $\alpha = 1.070, \mathrm{SLP} = 8322.6$

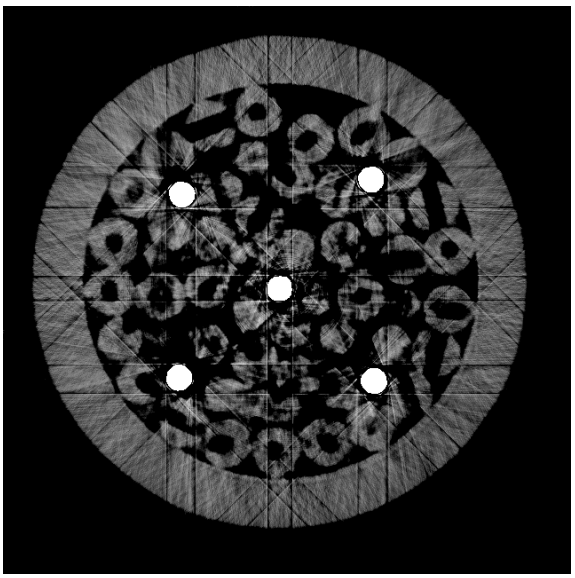

(f) $\alpha = 1.100, \mathrm{SLP} = 8246.3$

Fig. 5.5: The E-ART results (the iteration number : one).

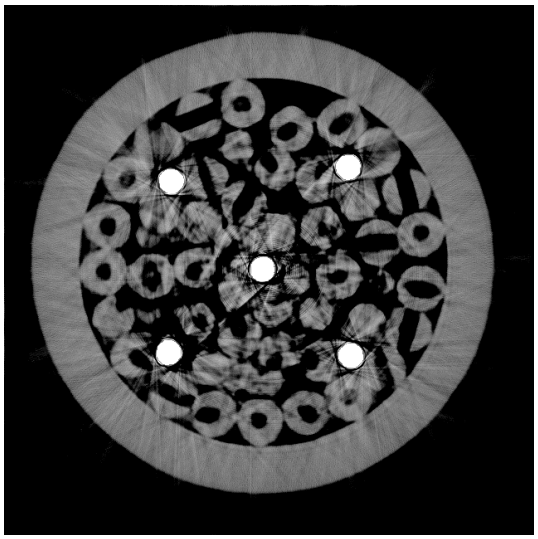

(a) $\alpha = 1.036, \mathrm{SLP} = 8655.8$

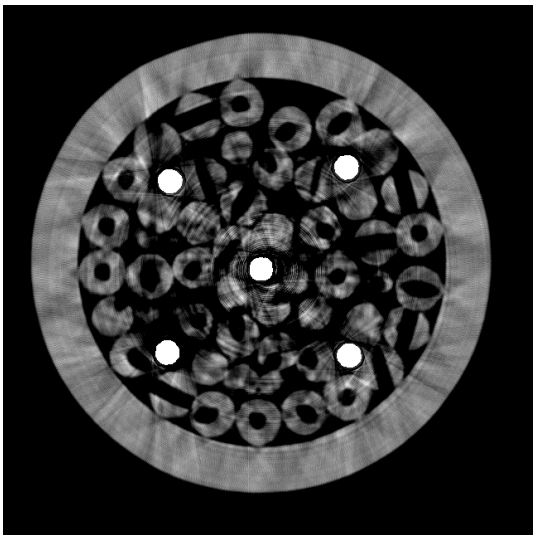

(b) $\mathrm{SLP} = 8414.4$

Fig. 5.6 Results for comparisons. (a) is the E-ART result (the iteration number : five), and (b) is the result using the metal artifact reduction algorithm based on sine curves.

5.3 Application to simulation data (MAR2)

This section shows application results to simulation data that were used in Chapter 4. In the previous section, extracted metal regions were used as initial images in iterative reconstruction to accelerate the convergence of images and to prevent from the divergence. On the other hand, in our simulation experiments, since the projection conditions are completely represented by numerical values, images will not diverge. Therefore, we can skip the metal extraction process in simulation experiments. This fact could lead to accurate reconstruction of metal shapes. The results are shown below.

5.3.1 The tooth phantom

The application result to the tooth phantom of Fig. 4.17 are showin in Fig. 5.7. Fig. 5.7(a) is the conventional FBP result, and Fig. 5.7(b) is the E-ART result. Metal artifacts and the value of RMSE were drastically reduced, and the gum regions can be observed clearly.

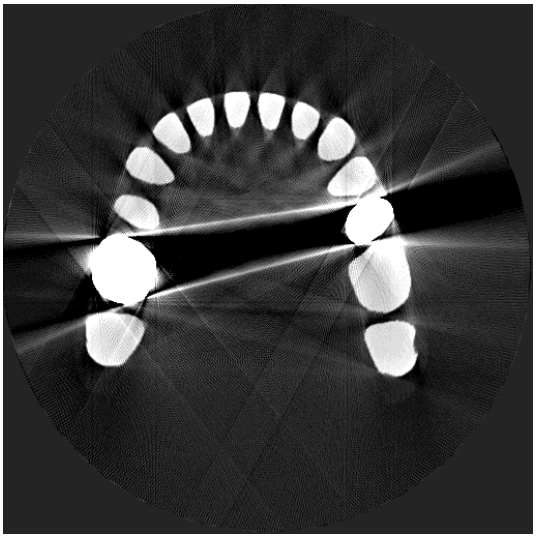

(a) RMSE = 52.324, SSIM = 0.71185

(b) RMSE = 5.1639, SSIM = 0.99160

Fig. 5.7 Application results to the numerical tooth phantom. (a) is the FBP result, and (b) is the E-ART result (the iteration number : five).

5.3.2 The head phantom

The application result to the head phantom of Fig. 4.22 are shown in Fig. 5.7. Fig. 5.8(a) is the conventional FBP result, and Fig. 5.8(b) is the E-ART result. Metal artifacts disappeared almost perfectly. Although the value of RMSE is larger than the case of the tooth phantom, it can be thought there is no influence on diagnoses.

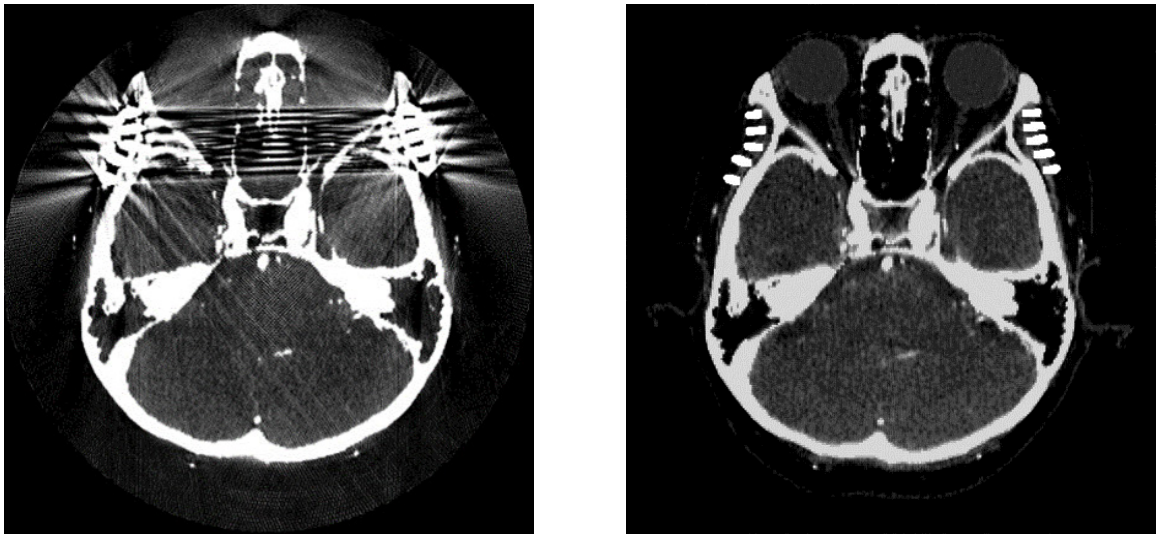

(a) RMSE = 57.686, SSIM = 0.79036 (b) RMSE = 12.823, SSIM = 0.95851

Fig. 5.8 Application results to the numerical head phantom. (a) is the FBP result, and (b) is the E-ART result (the iteration number : five).

5.3.3 The stomach phantoms

The application result to the stomach phantoms in Chapter 4 are shown in Fig. 5.9, Fig. 5.10, Fig. 5.11, Fig. 5.12 and Fig. 5.13. We see that all the E-ART results show dramatic metal artifact reduction, and the lesions became observable clearly in the all cases.. Furthermore, especially in Fig. 5.12 and Fig. 5.13, metal shapes were extracted accurately. Only in Fig, some blurred regions slightly remained between the metals, however, it can be ignored in most cases.

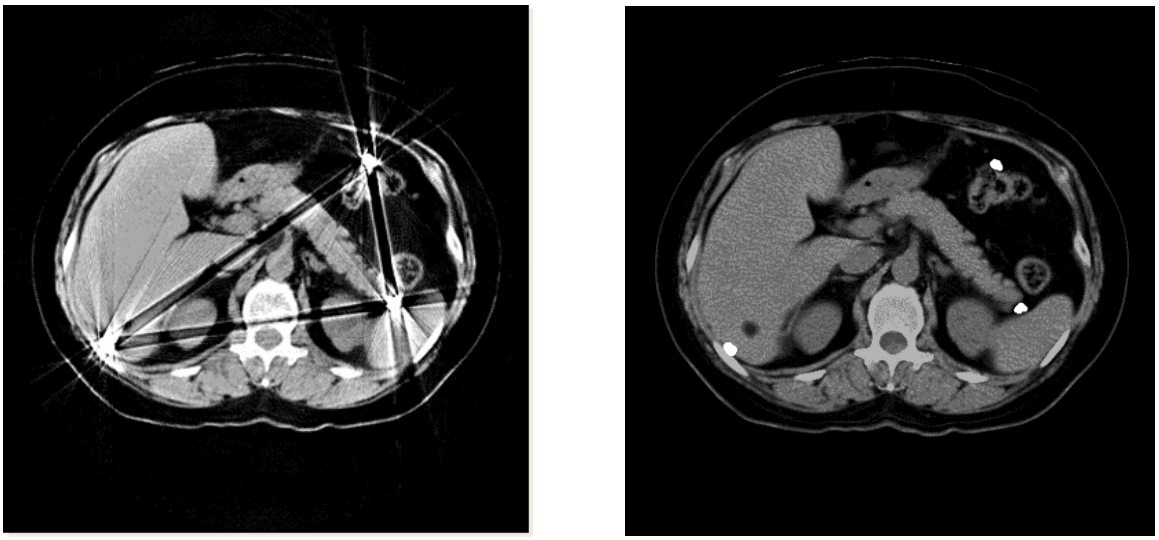

(a) RMSE = 44.359, SSIM = 0.84765 (b) RMSE = 6.6133, SSIM = 0.97577

Fig. 5.9 Application results to the stomach phantom A. (a) is the FBP result, and (b) is the E-ART result (the iteration number : five).

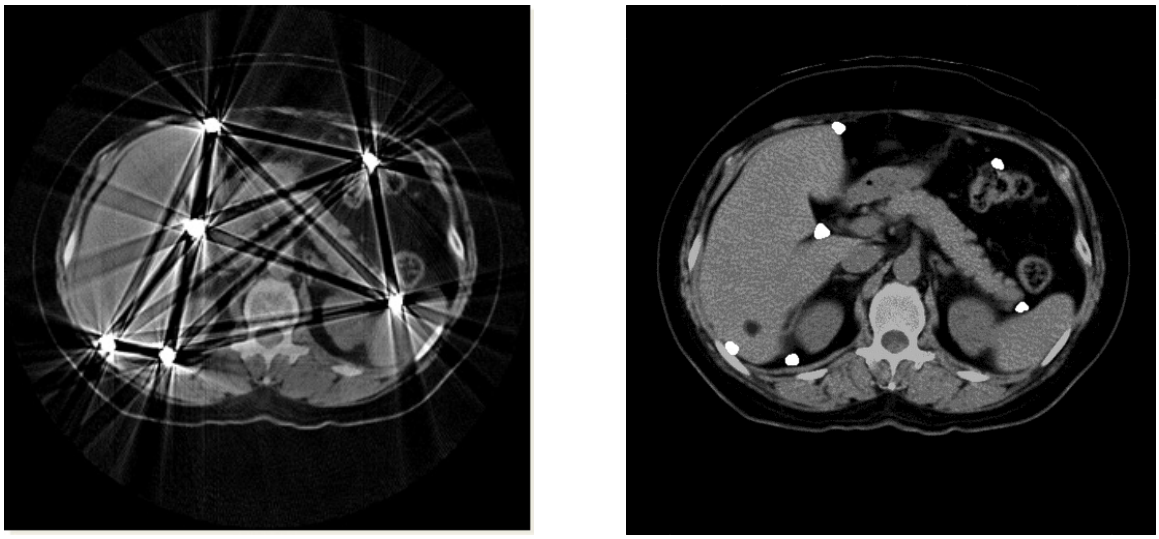

(a) RMSE = 36.633, SSIM = 0.0.77800 (b) RMSE = 6.8924, SSIM = 0.97464

Fig. 5.10 Application results to the stomach phantom B. (a) is the FBP result, and (b) is the E-ART result (the iteration number : five).

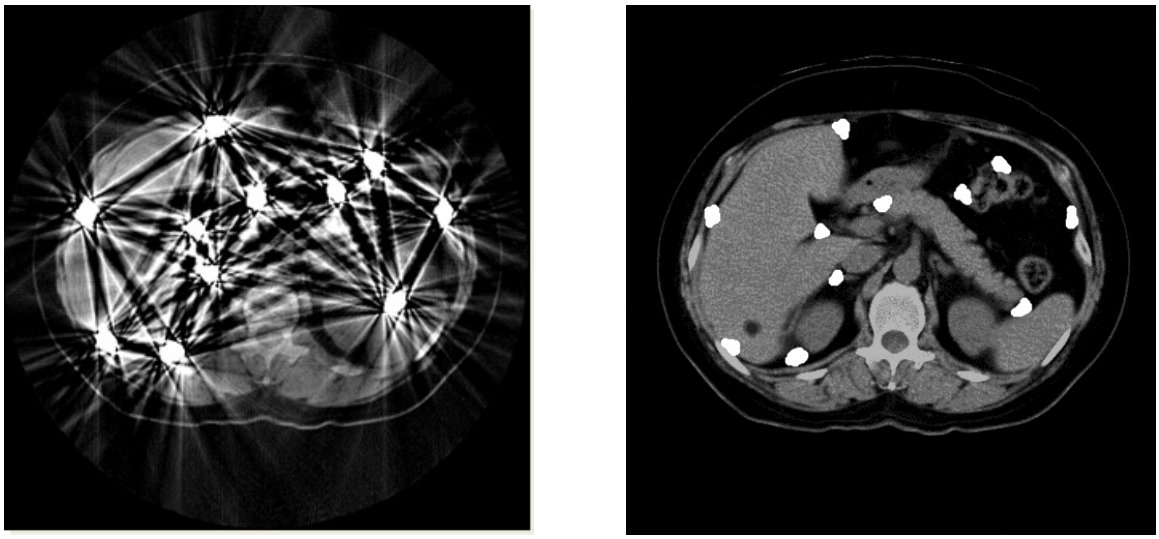

(a) RMSE = 54.884, SSIM = 0.77132 (b) RMSE = 7.7038, SSIM = 0.97071

Fig. 5.11 Application results to the stomach phantom C. (a) is the FBP result, and (b) is the E-ART result (the iteration number : five).

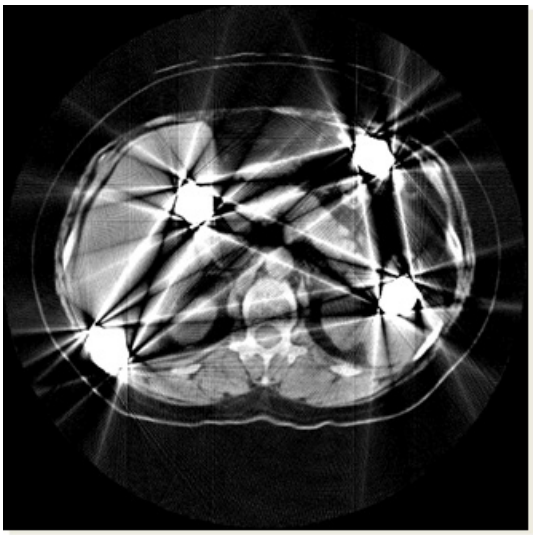

(a) RMSE = 55.203, SSIM = 0.77931

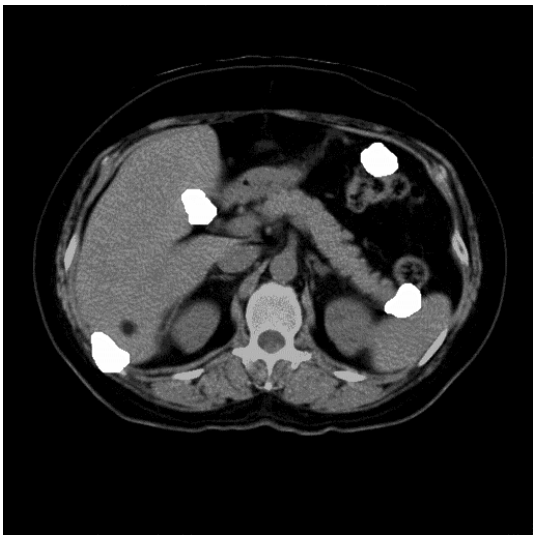

(b) RMSE = 7.5979, SSIM = 0.96974

Fig. 5.12 Application results to the stomach phantom D. (a) is the FBP result, and (b) is the E-ART result (the iteration number : five).

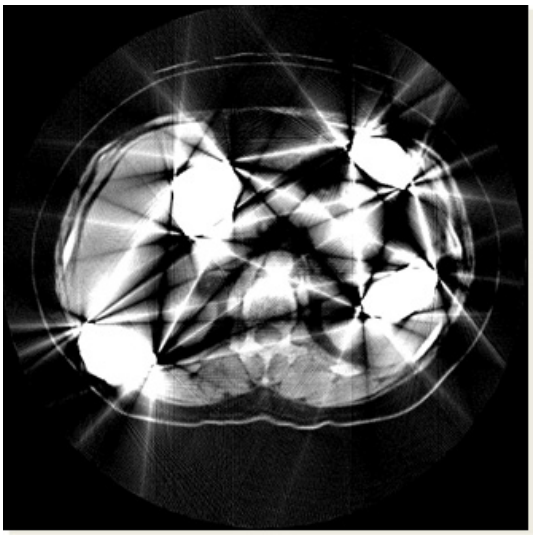

(a) RMSE = 64.848, SSIM = 0.78587

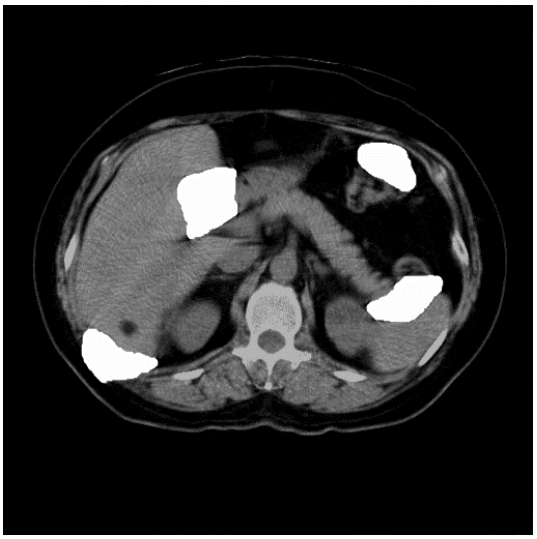

(b) RMSE = 9.1670, SSIM = 0.96092

Fig. 5.13 Application results to the stomach phantom E. (a) is the FBP result, and (b) is the E-ART result (the iteration number : five).

5.4 Discussion

5.4.1 Reconstruction accuracy

The SLP values, the RMSE values, and the SSIM values show that the E-ART can create more accurate images than the FBP. The resulting images also look more accurate qualitatively. Particularly in simulation data, metal regions were extracted accurately, and metal artifact were disappeared almost completely. The reason why is that it became possible to perform iterative calculations including metals in the simulation, while it was necessary to extract metal regions beforehand and ignore iterative calculations of metals in actual CT data. As it stands now, iterative calculations can not be converged stably without setting the metal extraction result as the initial image for actual data. However, if the accuracy of forward projection calculations improve, there will be no need to prepare metal initial images as with simulations.

5.4.2 Reconstruction time

It is also necessary to mention about the time required for reconstructions. All measurements were performed with the same PC, and the experimental sample D (Fig. 4.14) was used for comparison. Also, each average time was calculated from 1000 experiments.

The conventional FBP time for the experimental sample D was an average of 1.60 seconds. In the method based on sine curves, a sine curve extraction and the FBP are performed. Since the sine curve extraction required an average of 36.3 seconds, it takes 37.9 seconds in total. On the other hand, one iteration calculation time in the E-ART was an average of 53.0 seconds. This means that 5 times iteration calculation requires 260 seconds. Therefore, it was confirmed that the E-ART have a disadvantage for reconstruction time.

Since both methods have advantages and disadvantages, it will be better to select either method depending on the observation object or the purpose of the scan.

Chapter 6

Application to three-dimensional data

Chapter 6: Application to three-dimensional data

In the previous chapters, we have proposed metal artifact reduction algorithms assuming two-dimensional images. However, X-ray CT that can acquire three-dimensional data such as cone beam CT or helical scan CT are used in most cases. Therefore, we have to extend our two-dimensional algorithm to three-dimensional one so as to widely disseminate our superior technology. In this Chapter, a metal artifact reduction in cone beam CT is proposed.

6.1 Three-dimensional image reconstruction

If the data is two-dimensional, reconstruction algorithms assuming parallel beam X-rays can be applied by using fan/parallel conversion in any cases. However, it is not possible to convert cone beam data into parallel beam or fan beam data, so there is a need to perform directly three-dimensional reconstruction. Three-dimensional reconstruction algorithms can be derived from directly fan beam reconstruction.

6.1.1 Fan beam reconstruction

We first introduce the concept of a fan beam reconstruction algorithm without fan/parallel conversion. When using parallel beam X-rays, a detector position X where a point $\mu(x, y)$ is projected is readily expressed as:

$$X = x\cos\theta + y\sin\theta, \tag{6.1}$$

where θ is the projection angle. On the other hand, when using fan beam X-rays, the projection position changes depending on SOD (Source to object distance) and SID (Source to image-receptor distance). In order to formulate a fan beam reconstruction, Fig. 6.1 shows geometric arrangements of CT elements. We defined t as the distance of a point $\mu(x, y)$ to the rotation axis O, and ϕ as the angle between a point $\mu(x, y)$ and x-axis. The distance t

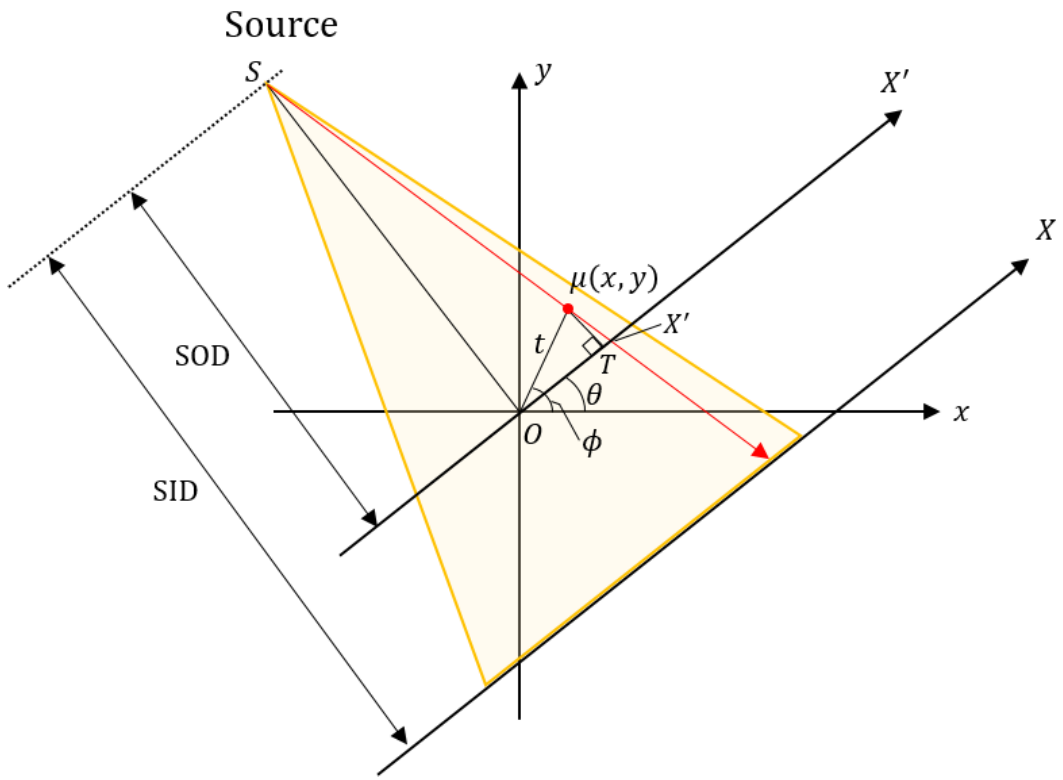

Fig. 6.1: A definition of geometric arrangement.

and the angle ϕ are represented respectively as:

$$t = \sqrt{x^2 + y^2} \tag{6.2}$$

$$\phi = \tan^{-1}\frac{y}{x}. \tag{6.3}$$

We also defined X' as the detector position where a point $\mu(x, y)$ is projected from the projection direction θ, and T as the point at the intersection of the perpendicular line from $\mu(x, y)$ to X'-axis with X'-axis. In this definition, from the similarity relationship of $\triangle\mu OT$ and $\triangle X'SO$, the position X where a point $\mu(x, y)$ is projected is calculated as:

$$X = \frac{t\cos(\phi - \theta) \cdot \mathrm{SID}}{\mathrm{SOD} - t\sin(\phi - \theta)}. \tag{6.4}$$

As compared to the calculation using fan/parallel conversion, such a directly fan beam reconstruction is often regarded as disadvantageous in computation time. The reason is because the calculation amount of trigonometric functions in fan beam is larger than one in parallel beam. This problem can be solved by expanding the formula using addition theorem,

and calculating $\sin\theta$, $\cos\theta$, $\sin\phi$, $\cos\phi$ and t for each (x, y) in advance.

$$X = \frac{t(\cos\phi\cos\theta + \sin\phi\sin\theta)\cdot \mathrm{SID}}{\mathrm{SOD} - t(\sin\phi\cos\theta - \cos\phi\sin\theta)}. \tag{6.5}$$

As just described, the amount of calculations can be similar to parallel beam one by simplifying the formula.

6.1.2 Cone beam reconstruction

Next, we formulate a cone beam reconstruction algorithm. The cone beam reconstruction can be readily derived by considering a directly fan beam reconstruction as described above. Since projection positions in horizontal direction has already been calculated, it is only necessary to calculate projection positions in vertical direction. The height Z where a point $\mu(x, y, z)$ is projected is calculated by considering the geometric arrangements of CT elements as with the fan beam case:

$$Z = \frac{z\cdot \mathrm{SID}}{\mathrm{SOD} + \sqrt{x^2 + y^2}\sin\theta}. \tag{6.6}$$

To verify the above theory, Eqn. 6.5 and Eqn. 6.6 are applied to cone beam data. The experimental tire model without metals is shown in Fig 6.2, and the projection conditions are shown in Table 6.1. Since the detector resolution is 640×480, the resolution of a cross-sectional image become 640×640, and the three-dimensional reconstruction resolution become $640 \times 640 \times 480$. Fig. 6.3(a) shows the cone beam projection data from one direction, Fig. 6.3(b) shows the reconstruction result at the height 195, and Fig. 6.3(c) shows the reconstruction result at the height 275. Both images were accurately reconstructed, and voids in the tire can be observed.

Fig. 6.2: The wheel model.

Table 6.1: Projection conditions of the wheel model.

Component materials	Resin, rubber
X-ray tube voltage [kV]	81
X-ray tube current [μA]	53
Number of voxels	$640 \times 640 \times 480$
Field of view [mm]	ϕ 32.0
Number of projections	800
Each projection time [s]	0.53

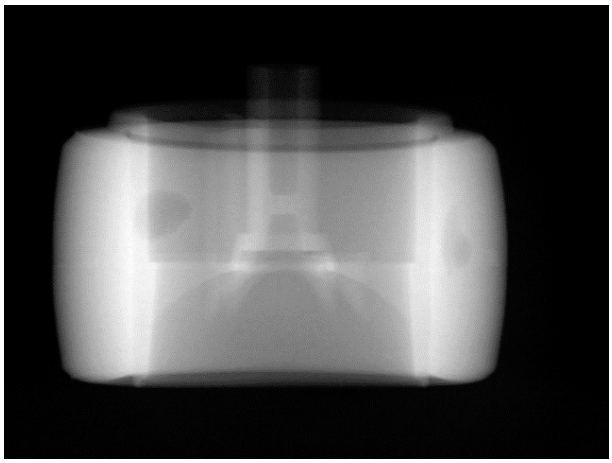

(a)

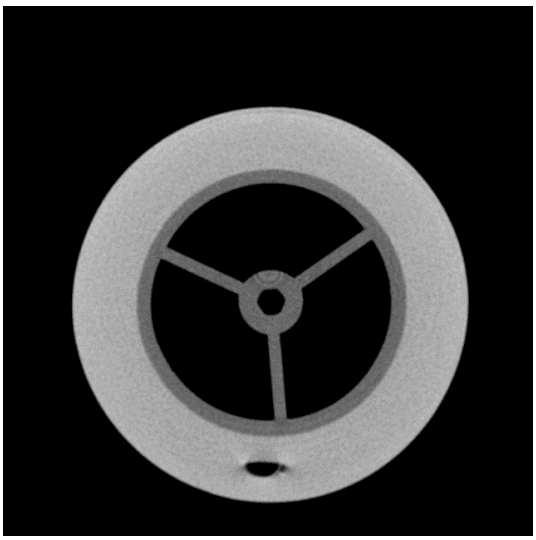

(b)

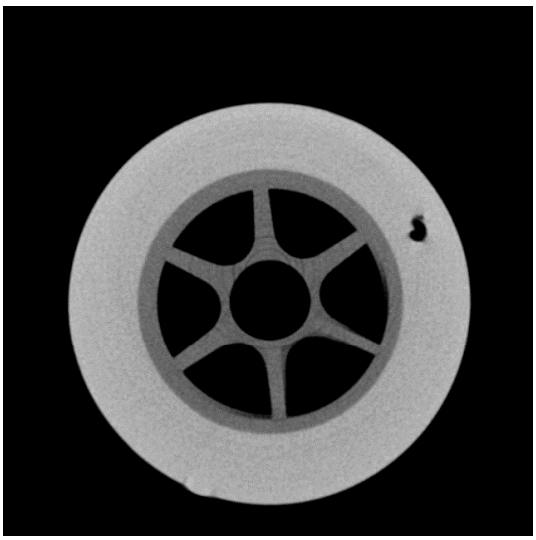

(c)

Fig. 6.3 An X-ray projection and a verification of a back projection. (a) is the cone beam projection data, (b) is the FBP result at the height 195, and (c) is the FBP result at the height 275.

6.2 Extension of the metal artifact reduction based on sine curves

In the previous section, the back projection calculation for cone beam data was formulated. We next consider about a three-dimensional approach for the metal artifact reduction method based on sine curves.

In cases of cone beam CT data, trajectories on sinograms drawn by object areas are not sine curves except for the central section. However, trajectories on projection data drawn by one voxel on a three-dimensional space are given by Eqn. 6.5 and Eqn. 6.6. In order to express this thought visually, we performed a three-dimensional visualization of the projection data of the physical phantom composed of 9 metallic poles shown in Fig. 6.4. The result of three-dimensional visualization is shown in Fig. 6.5. For the sake of practical convenience, we will call such data three-dimensional sinograms below. If you cut horizontally this three-dimensional sinogram in the center, it will be a two dimensional sinogram that is used in the previous chapters. Also, by observing this three-dimensional sinogram, you can see that the trajectories are changing in the vertical direction ($z-axisdirection$). It is thought that metal artifacts can be reduced by extracting continuities of a trajectory from three-dimensional sinograms as in cases of sine curve extractions.

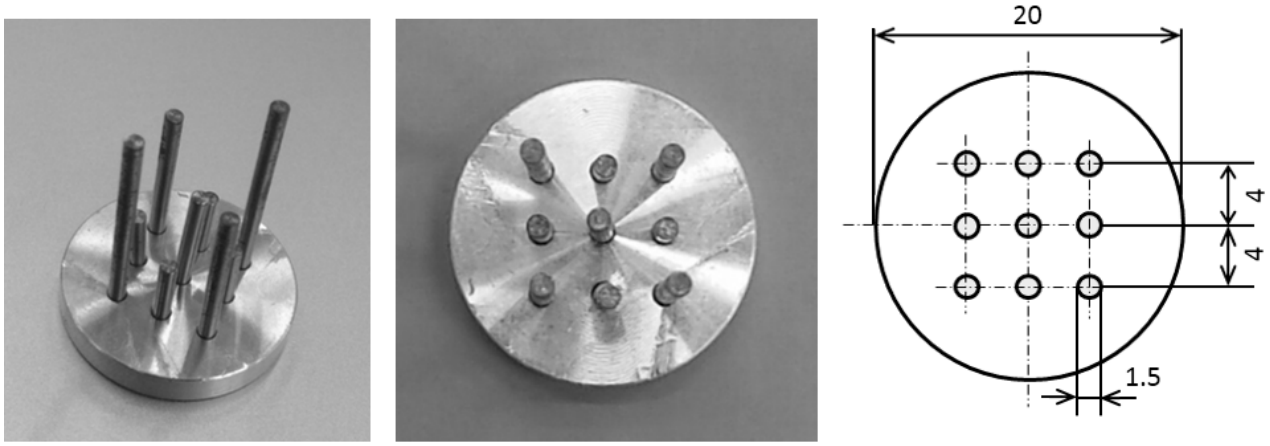

Fig. 6.4: An experimental sample composed of 9 iron poles.

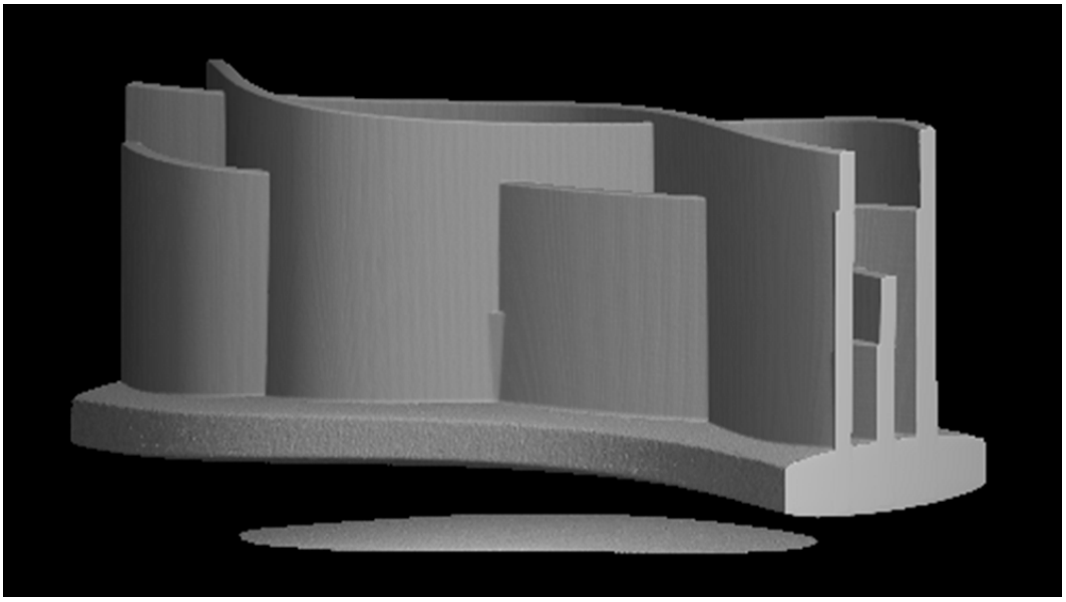

Experimental conditions	
Component materials	Iron
Number of metallic objects	9
Number of voxels	$512 \times 512 \times 512$
X-ray voltage [kV]	40
X-ray current [μA]	200
Number of projections	800

Fig. 6.5: A 3D sinogram generated from Fig. 6.4.

6.2.1 Appliocation to CT data

To confirm the effectiveness of the above thought, we created a program that extracts three-dimensional metallic regions. This extraction experiment used the physical phantom shown in Fig. 6.4. We performed surface rendering to the conventional three-dimensional reconstruction, and cut the center of the model. The result is shown in Fig. **??**. Metal artifacts were generated, and the cross-section and the three-dimensional shape became unclear. Next, we evaluated the continuities of the trajectories of the three-dimensional sinogram. The result of visualization of the three-dimensional metallic regions is shown in Fig. 6.7. Although there are some rough parts on the surface, metal regions could be extracted almost accurately. The main cause of the roughness is probably the binalization of the voxels, which does not consider partial volume effects. In order to solve this problem and establish three-dimensional metal artifact reduction based on trajectories, we have next to conduct sub-voxel rendering at boundary regions of metals and non-metals, or weighting voxels by using continuous/average values along three-dimensional trajectories.

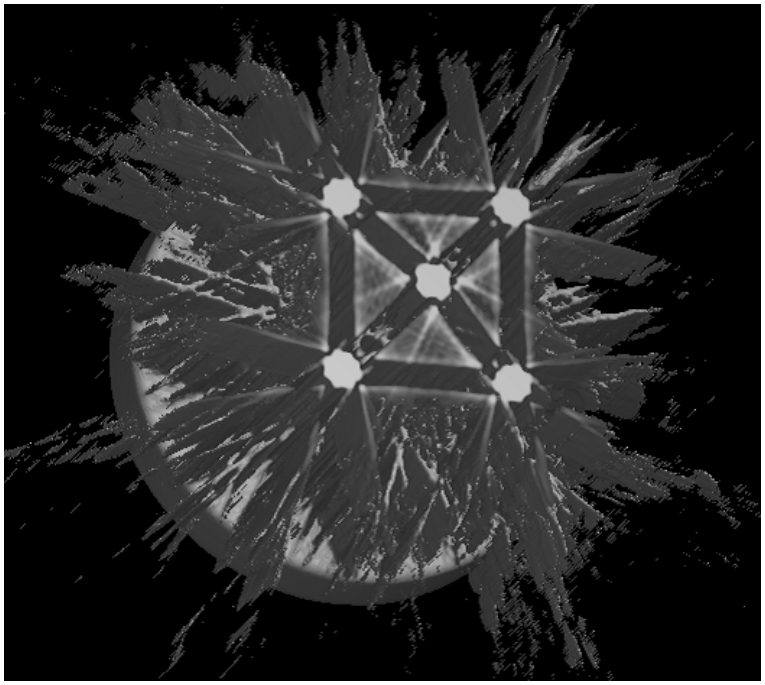

Fig. 6.6 The FBP result of the cone beam data of the experimental sample shown in Fig. 6.4.

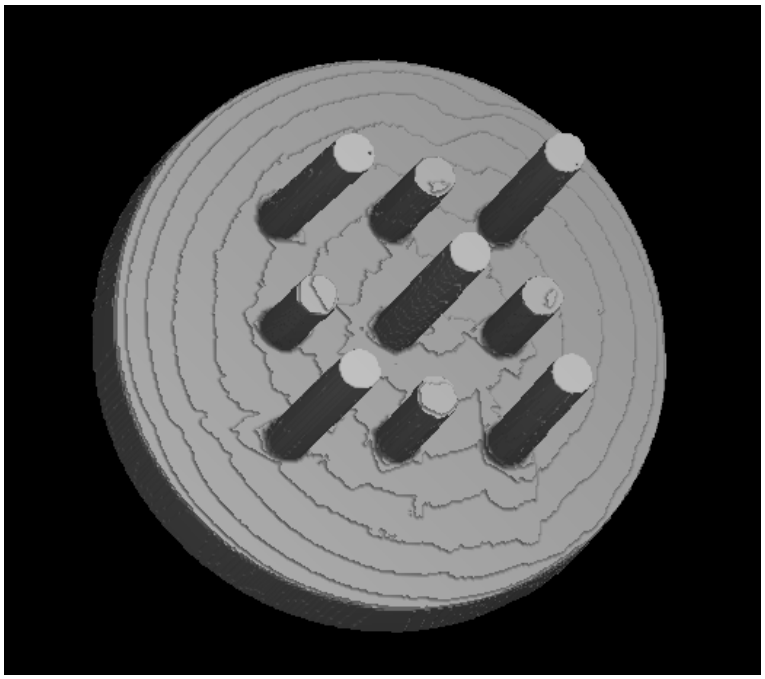

Fig. 6.7: The result of applying the proposed algorithm for cone beam data.

6.3 Extension of the metal artifact reduction based on iterative reconstruction

In this section, we extend the metal artifact reduction method based on iterative reconstruction to three-dimensional one. To implement cone beam iterative reconstruction, it is necessary to prepare a cone beam forward projection calculation (three-dimensional Radon transform). This calculation can readily be obtained through an application of a cone beam reconstruction calculation. Fig. 6.8(a) shows the simulation result of the cone beam forward projection to the three-dimensional voxel data, which was reconstructed in Fig. 6.3. After the forward projection calculation, cone beam reconstruction were performed again, and the results are shown in Fig. 6.8(b) and Fig. 6.8(c). Fig. 6.8(b) shows the reconstruction result at the height 195, and Fig. 6.8(c) shows the reconstruction result at the height 275. From these results, it is verified that the cone beam calculations are performed accurately.

Once the forward projection and the back projection formulated, the metal artifact reduction algorithm proposed in Chapter 5 can be applied by incorporating energy information to the forward projection calculation. The following shows the results of implementing a three-dimensional metal artifact reduction.

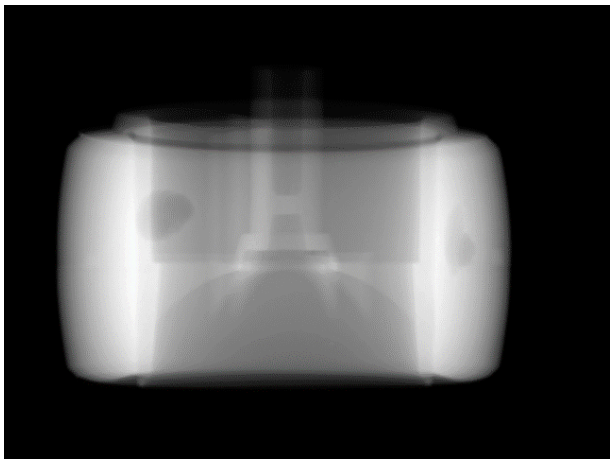

(a)

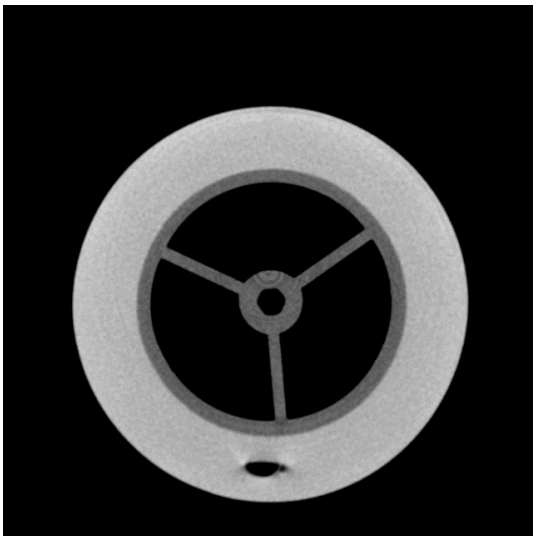

(b)

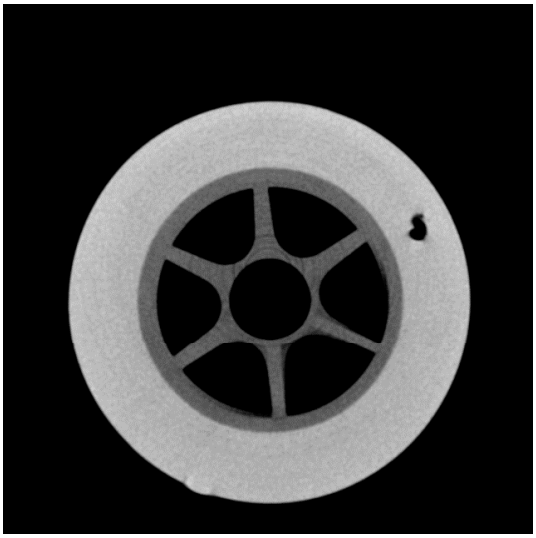

(c)

Simulation conditions	
Component materials	Resin, rubber
Detector resolution	640×480
Dot pitch [mm]	0.05
Number of projections	800

Fig. 6.8 A verification of a forward projection and a back projection on simulation. (a) is the cone beam projection data to the FBP result of Fig. 6.3, (b) is the FBP result at the height 195, and (c) is the FBP result at the height 275.

6.3.1 Application to simulation data

To verify performances of metal artifact reduction for cone beam data, a three-dimensional numerical phantom shown in Fig. 6.9 was created. This phantom is assumed the experimental sample A shown in Fig. 2.8, which is composed of a resin and metals. The resolution is $256 \times 256 \times 256$, and the cross-sectional images at the height 128 and height 64 are shown in Fig. 6.10(a) and Fig. 6.10(b), respectively.

The simulation experiment was performed at the conditions of Table. 6.2. Fig. 6.11 shows reconstruction results at the height 128 and 64, and metal artifacts were generated in both images.

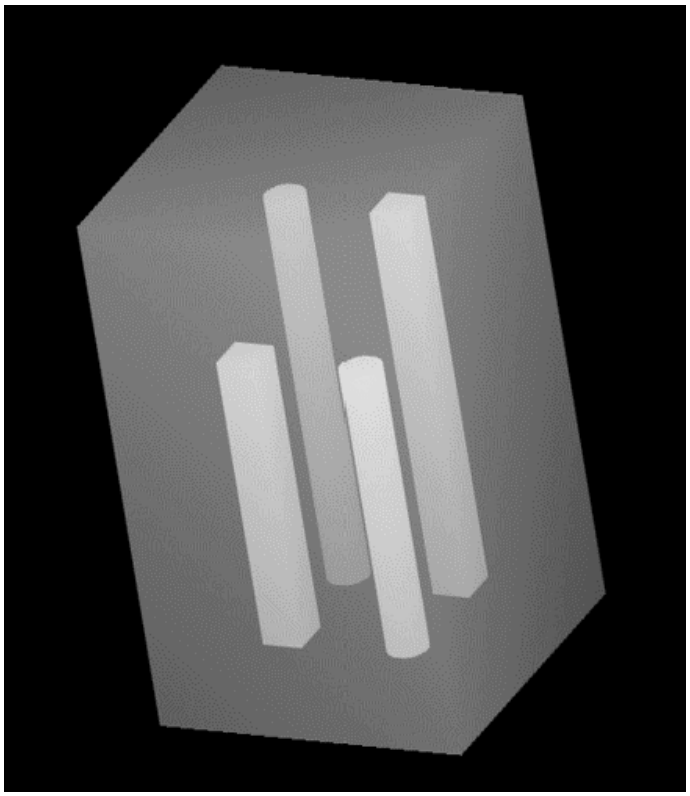

Fig. 6.9 The three-dimensional numerical phantom, which is assumed the experimental sample A.

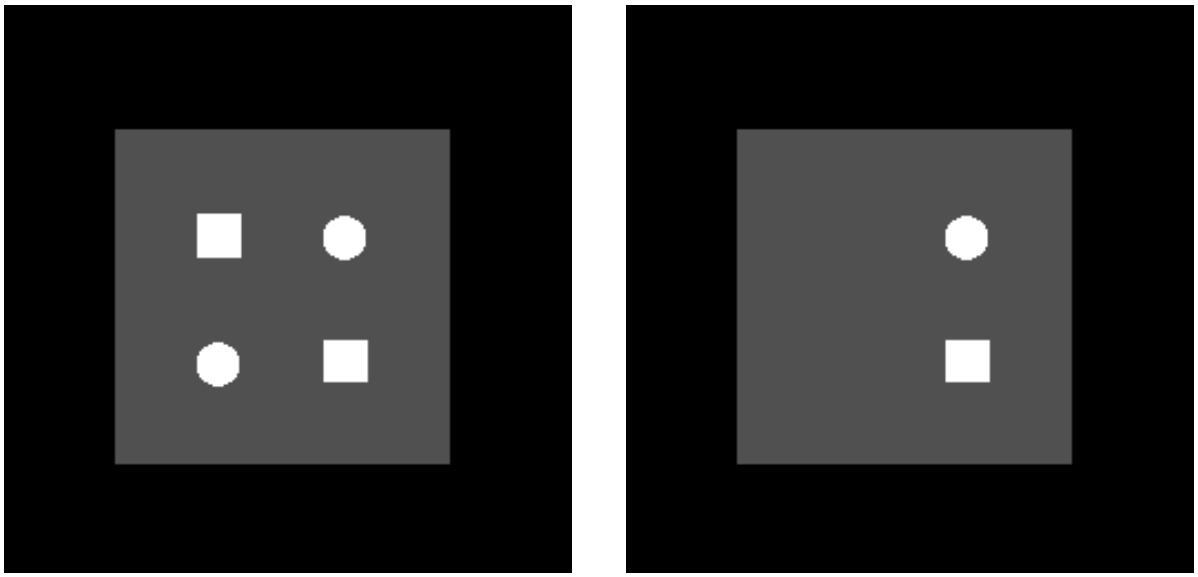

(a) (b)

Fig. 6.10 The cross-sectional images of the three-dimensional phantom shown in Fig. 6.9. The height of; (a) is 128 (center of the phantom) and (b) is 64.

Table 6.2: Simulation conditions of the three-dimensional phantom shown in Fig. 6.9.

Component materials	resin iron
Number of metallic objects	4
Number of voxels	$256 \times 256 \times 256$
Field of view [mm]	ϕ 30.7
SID [mm]	ϕ 1946
Number of projections	256

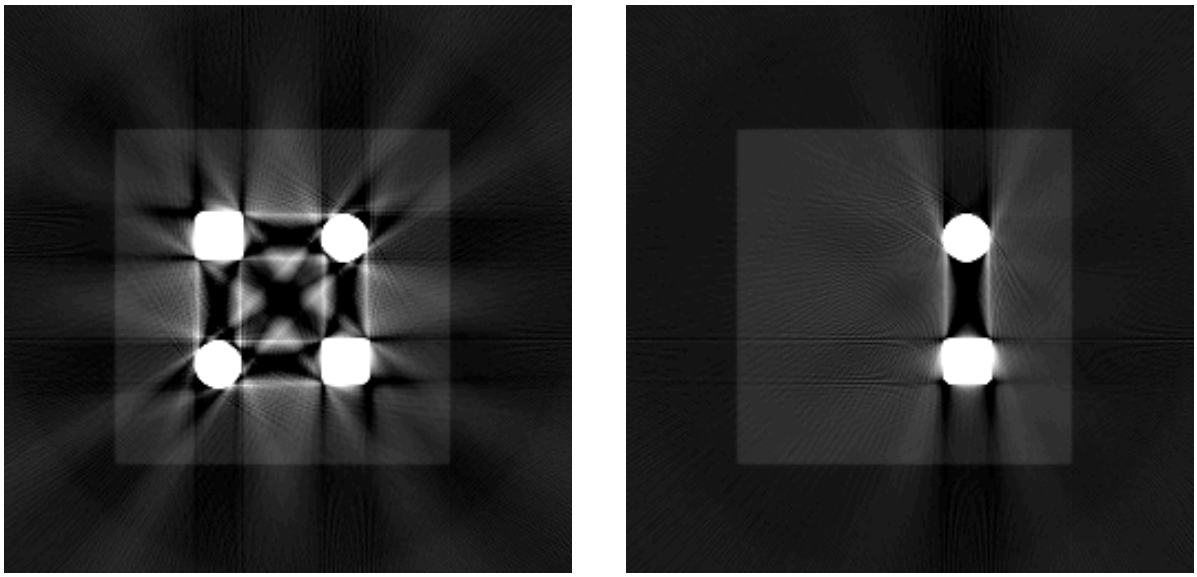

(a) RMSE = 33.5763 (b) RMSE = 28.7450

Fig. 6.11 The FBP result of the three-dimensional phantom. The height of; (a) is 128 (center of the phantom) and (b) is 64.

To complete the implementation of our algorithm, a distribution of X-ray attenuation coefficients that are composed of N kinds of properties was defined as:

- Prepare X-ray attenuation coefficients of iron, resin, and air.
- Divide X-ray attenuation coefficients of between air and resin into M equal parts.
- Divide X-ray attenuation coefficients of between resin and iron into $N - M - 3$ equal parts.

Fig. 6.12 shows the concept of this definition. We first defined that $N = 256, M = 80$, and the results of applying metal artifact reduction algorithm to cone beam data are shown in Fig. 6.13. Fig. 6.13(a) shows the result at the height 128 (center of the phantom), and Fig. 6.13(b) shows the result at the height 64. We see that metal artifacts were effectively reduced in both cases, and it was verified that our algorithm is also available to cone beam data. However, there were also some noises on these images. The reason seems to be because the projection number was limited to 256 to reduce computation time. The relationship between the projection number and the image quality is examined in Appendix A.

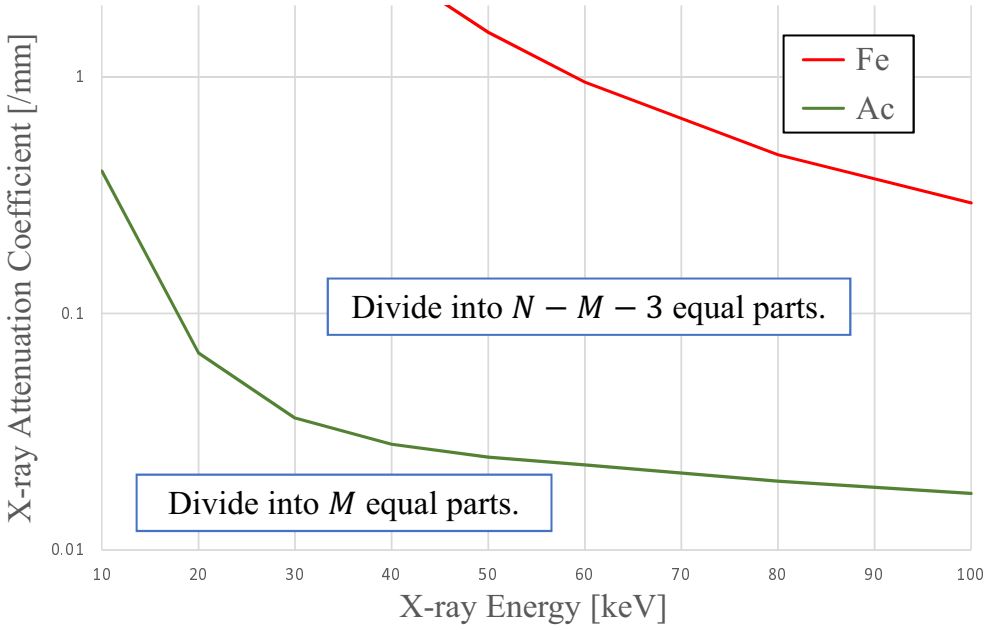

Fig. 6.12: Assumptions of X-ray attenuation coefficients.

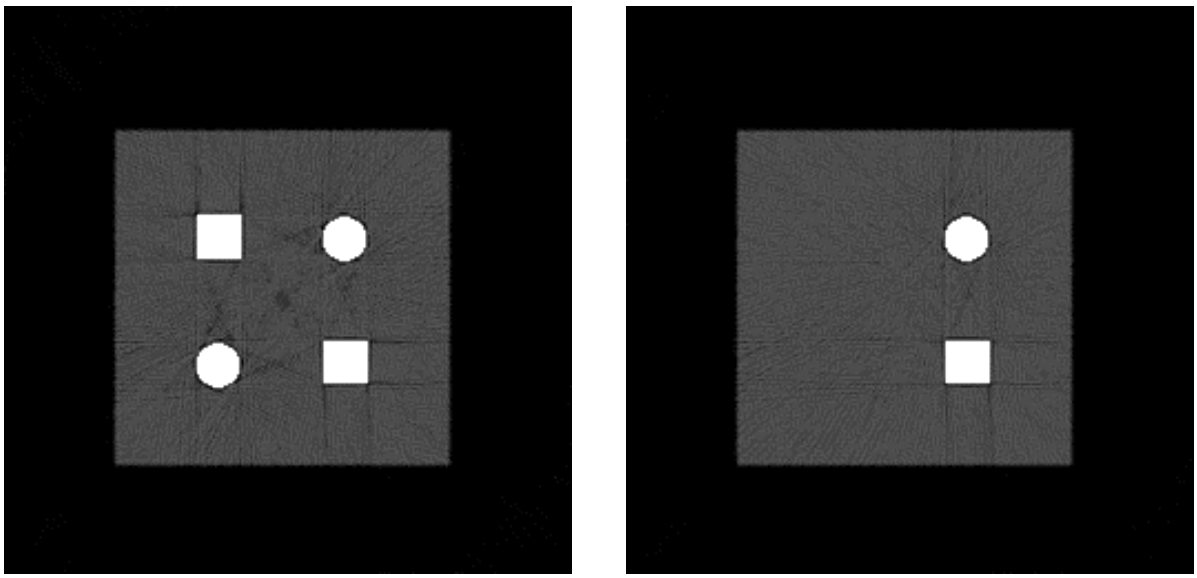

(a) RMSE = 7.3803 (b) RMSE = 6.5164

Fig. 6.13 The E-ART result of the three-dimensional phantom at the condition that $N = 256, M = 80$. The height of; (a) is 128 (center of the phantom) and (b) is 64.

Next, we defined that $N = 256, M = 36$, and the results of applying metal artifact reduction algorithm to the same three-dimensional data are shown in Fig. 6.13. Fig. 6.14(a) shows the result at the height 128 (center of the phantom), and Fig. 6.14(b) shows the result at the height 64. At the height 128, metal artifacts were effectively reduce as well as the case of $M = 80$. However, the values were not converged at the height 64, which has a certain distance from the center, and metal artifacts were emphasized. It was found that the amount of the projected metal greatly changed depending on the projection angle at the heights that images diverged. There seems to be such regions in three-dimensional data, and the calculations seem to become very sensitive to the distribution of X-ray attenuation coefficients in some regions. In order to achieve the stable calculation in three-dimensional data, it is necessary to discuss how to create X-ray attenuation coefficients in greater depth.

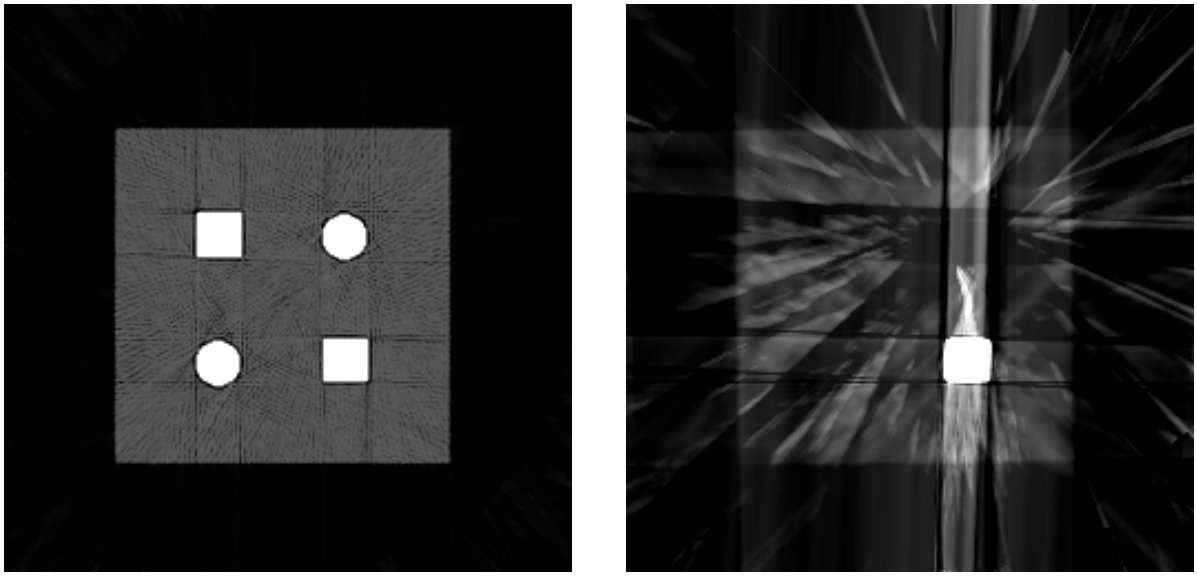

(a) RMSE = 7.4540 (b) RMSE = 34.217

Fig. 6.14 The E-ART result of the three-dimensional phantom at the condition that $N = 256, M = 36$. The height of; (a) is 128 (center of the phantom) and (b) is 64.

Chapter 7

Conclusion

Chapter 7: Conclusion

7.1 General conclusion

In this thesis, novel reconstruction algorithms for metal artifact reduction were proposed.

Chapter 1 mentioned metal artifacts as a problem in CT imaging, and introduced existing researches related to metal artifacts. Then the purpose of this study was indicated.

Chapter 2 explained the principle of X-ray CT, which is the basis of this study. The explanation began with physics of X-ray, and image reconstruction algorithms. As the reconstruction algorithms, back projections and iterative reconstruction were described. Technologies that relate to image reconstructions were also introduced, and the scan and reconstruction results for the actual experimental sample were shown. At the end of this chapter, it was revealed that the main causes of metal artifacts are influence of X-ray energy spectrum.

In Chapter 3, we developed an X-ray CT simulation software, which can inputs/outputs CT data, and computes conventional reconstruction images, as well as images using our reconstruction algorithms. Knowledge and processing about CT simulation were also described. By using our simulation technology, the following two things were confirmed; metal artifacts didn't generate in irradiation of monochromatic X-rays, while metal artifacts generated in irradiation of continuous X-rays. At the end of this chapter, RMSE and SSIM were introduced and SLP was proposed as quantitative evaluation methods. RMSE and SSIM can be used for simulation experiments, while SLP can be used for actual CT data.

Chapter 4 proposed a metal artifact reduction method based on the fact that sinogram (projection data) is composed of sine curves. By extracting sine curve information from sinogram, and reconstructing the separate metal and non-metal images then synthesizing them, we can eliminate metal artifacts. As a result of application to actual CT data and simulation data, metal artifacts were effectively reduced in both cases. In the simulation experiments, the amount of metal on the cross-section was changed to verify the performance

limit of our algorithm. Then it was confirmed that the performance of metal artifact reduction decreased with increased amount of metal on cross-section. The reason is considered that non-metal regions that have to be interpolated increase and available non-metal sine curves decrease along with the increase of metals. Meanwhile, parameters used in sine curve extraction were adjusted manually to enable effective metal artifact reduction. In particular, fine adjustments were essential to extract concave metal portions. Moreover, even though the fine adjustments were performed, it was difficult to extract the concave portions. In fact, peripheral regions of metals tended to become blurred. However, since this algorithm require little time and obtain enough images for diagnoses and inspection in most cases, it is thought that our algorithm is useful.

Chapter 5 proposed a novel metal artifact reduction method based on iterative reconstruction to solve the problem remained in Chapter 4. We first introduced the formula for deriving X-ray attenuation coefficient distributions. Next, by incorporating forward projection calculations that include energy information to iterative reconstruction, a new theory of metal artifact reduction was established. Since the idea is different from interpolations or improvements for projection data, it could reduce metal artifacts primordially. We applied our algorithm to actual CT data, thereby advantages over the technique proposed in Chapter 4 were shown. Additionally in simulation data, precise metal shapes were extracted, and metal artifacts were dramatically reduced. This result implies that actual data also can be significantly reduced by improvements of projection calculations. Besides, our method based on iterative reconstruction requires more calculation time than the method based on sine curves. However, this is not really a big problem, and it is also possible to be solved by using GPGPU.

These technologies that proposed in the previous sections were targeted at a two-dimensional image. In Chapter 6, our metal artifact reduction algorithm was extended to three-dimensional one so as to widely disseminate our superior technology. First, calculations of three-dimensional back projection was formulated, and the metal artifact reduction for cone beam data based on trajectories was established by extending MAR1. The efficacy of the three-dimensional

metal extraction was confirmed for the physical phantom. To apply this algorithm to three-dimensional non-metallic regions, there is a need for further improvements. Next, three-dimensional forward projection was formulated, then the theory of metal artifact reduction for cone beam data based on iterative reconstruction was established by combining energy information to the forward projection calculation. Validation was performed using a three-dimensional numerical phantom, and the availability for cone beam data was demonstrated. At the same time, it was found that it was difficult to apply the algorithm to some regions for three-dimensional data. The necessary to consider about creation of X-ray attenuation coefficients in greater depth was indicated.

7.2 Future plans

In this thesis, although it was succeeded to significantly reduce metal artifacts, some technical challenges remain. The details are described below.

7.2.1 Sine curve extraction algorithm

The performance of the metal artifact reduction method based on sine curves, which was proposed in Chapter 4, depends on user's experience especially in determinations of the sine curve extraction parameters. Therefore, we are planning to consider a method for selecting optimal parameters based on quantitative evaluations such as SLP. Meanwhile, a geometric fitting algorithm was used as the sine curve extraction in this thesis. For the future, Fourier transform or wavelet transform will be used to extract potential sine curves on sinograms. It is thought that frequency characteristics on sinograms provide us with more information.

7.2.2 Iterative reconstruction algorithm

The metal artifact reduction method based on iterative reconstruction, which was proposed in Chapter 5, showed fantastic performance in simulation experiments. Although the method also showed good performance for actual CT data, there is need to prepare extracted metal

region as the initial image, and the calculation convergence is unstable. Furthermore, the calculation convergence became more sensitive to the distribution of X-ray attenuation coefficients in the application to three-dimensional data. In order to solve these problems, procedures for accurately simulating the projection environments such as an energy distribution of the incident X-ray are required. The energy distribution is able to be obtained by using equipment like a spectrum analyzer. However, such equipment are expensive, and they require a modification of hardware, so it is difficult to integrate them into existing X-ray CT. Therefore, it is planned to consider a procedure that estimates X-ray energy distributions by using standard samples.

7.2.3 Qualitative evaluation

As quantitative evaluation methods, we have used RMSE, SSIM, and SLP. However, it is difficult to determine whether the metal artifact reduction for the actual diagnosis/inspection is enough or not only by using these indicators. In order to indicate qualitative performances, it's thought that ROC (Receiver operating characteristic) analysis is effective. In the ROC analysis, by classifying the correctness of subjective diagnoses/inspections, you can estimate statistically the efficacy. For example, consider a trial that asks an existence of a lesion for two reconstruction results (or result of applying metal artifact reduction methods). Here, one of them is generated from a phantom that includes organs, metals and a lesion (positive phantom), and the other is generated from a phantom that includes organs and metals (negative phantom). The trial result is able to classified to four groups; true positive, false negative, false positive and true negative. Then, by collecting several trial data from several observers, and confirming the distribution of their responses to each image, it is able to be express the qualitative effectiveness. We are going to compare and fusion the ROC analysis and quantitative methods so as to evaluate the sufficiency of metal artifact reduction.

7.2.4 Application to clinical data

In this study, we proposed the metal artifact reduction methods and applied them to various data. Nevertheless, the application targets were only simple experimental samples and simulation data. To verify the usefulness in actual fields, it is necessary to apply our methods to much more CT data such as clinical data. In the future, we will cooperate with hospitals and companies that are troubled by metal artifacts, and expand the application range.

7.3 Further advancement

This study and the future plans were one of the basic researches in X-ray CT. In the future, we should apply the basic study to new research areas. The examples of the ideas are introduced in the following.

7.3.1 Surgery simulation using AR

In recent years, applying AR (Augmented reality) techniques to medical fields has attracted attention. In fact, there are some AR techniques that have been put to practical use, such as a technology that can display a surgery guide on a space through a PC monitor or a head-mounted display. However, almost all of the AR techniques as applications to medical fields are simple guides that supports doctors. On the other hand, since the AR is excellent with X-ray CT that obtains three-dimensional data, a variety of application cases can be thought. For example, if it become possible to observe any cross-sections and internal structures, or to make organs and blood vessels transparent by combining the AR and X-ray CT, it will lead to an efficacy and a reduction of risks at the time of surgery. More specifically, we are paying attention to Haptic AR, and planning to develop new technologies, such as an elaborate catheter surgical simulation, and a control mechanism of dangerous movements in surgeries. These technologies will contribute greatly to success rates for surgery. Although technologies that combine the AR and CT have hardly put to practical use, it's sure that they are effective to various situations in medical fields.

7.3.2 Expansion into CAD technologies

As a new challenge, we are also considering an expansion into computer-aided diagnosis (CAD). CAD is a technique to support decisions and to exclude oversights of lesions when physicians give a diagnose using CT, MRI, and PET/SPECT images. One of the biggest problem in CAD is an influence caused by individual differences. In actual cases, this problem is usually solved by physicians' experience, while in CAD, it has been attempted to solve the problem by using machine learning or data mining technologies to accumulated medical images. However, the accuracy and the reliability of CAD are still insufficient. On the other hand, we established the artifact reduction algorithms, the unique feature extraction technique, and the original image evaluation index in this thesis. By fusing these techniques and machine learning or data mining technologies, important information will be made a choice from big data efficiently and accurately, then a new CAD techniques will be established.

Appendix A

A relationship between projection numbers and reconstruction accuracy

As the number of projections increases, the accuracy is improved, while the radiation exposure and the calculation time also increase. Therefore, we have to choose the number of projections which can create enough reconstruction images. In this Appendix, a relationship between projection numbers and reconstruction accuracy is verified.

A.1 Observation of accuracy

To conduct the verification, the numerical phantom shown in Fig A.1, which assumes the experimental sample A, was prepared. Then we applied forward projection calculations while changing projection numbers on simulations, and observed the reconstruction accuracy. However, monochromatic X-rays were used as the incident X-ray, in order to prevent the metal artifact generation, and to facilitate the evaluation of accuracy.

The FBP results are shown in Fig. A.3. Fig. A.3(a) and Fig. A.3(b) show the result at $p = 4, p = 10$, respectively. Since the number of projections was not enough, both images could not be reconstructed accurately. Meanwhile, these images can help you to understand how back projection is performed. Fig. A.3(c) and Fig. A.3(d) show the result at $p = 100, p = 200$, respectively. We see that there are moire-shaped artifacts on these

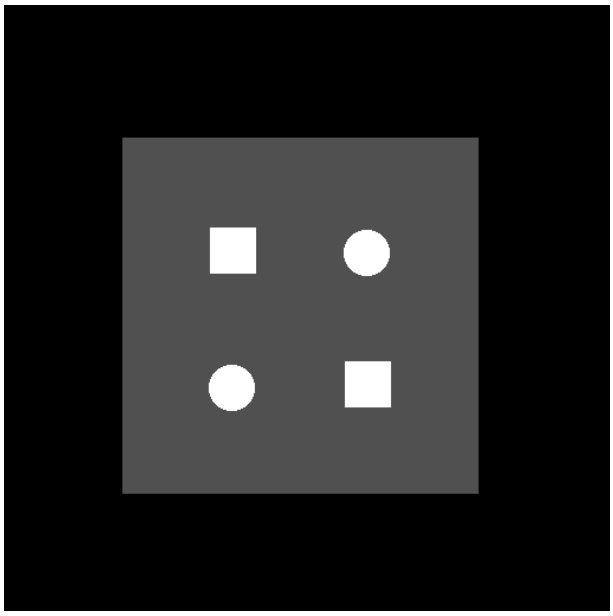

Fig. A.1: Phantom

images, and it indicates that the number of projections is still not enough. Fig. A.3(e) and Fig. A.3(f) show the result at $p = 400, p = 800$, respectively. There are almost no artifacts on these images, and their RMSE value also indicates good values. There are also remained some line-shaped artifacts, but it is thought that the effect on inspections is little. Fig. A.3(g) and Fig. A.3(h) show the result at $p = 1600, p = 3200$, respectively. Compared to Fig. A.3(f), more artifacts were reduced and the RMSE values also became better. However, the accuracy was not changed much, and it is difficult to confirm the qualitative differences. Fig. A.3 shows the relationship between projection numbers and RMSE. As the number of projections increases, the accuracy approaches a constant value. This result indicates there is no need to project from many directions. Therefore, we decided to use 512 or 800 as the number of projections in this study.

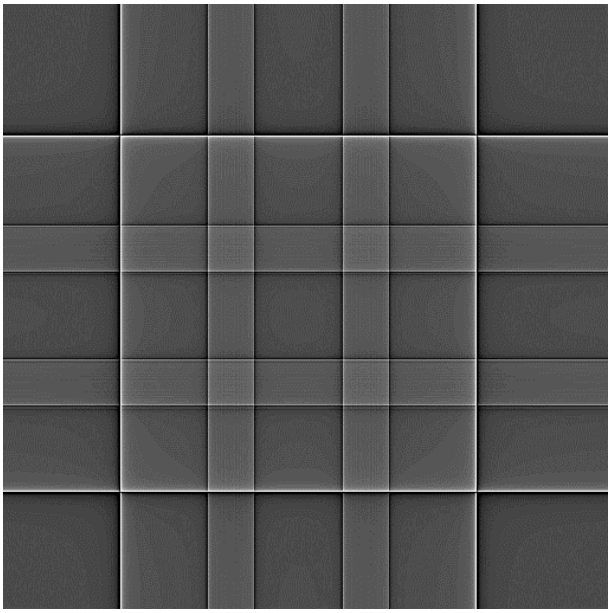

(a) $p = 4, \mathrm{RMSE} = 69.853$

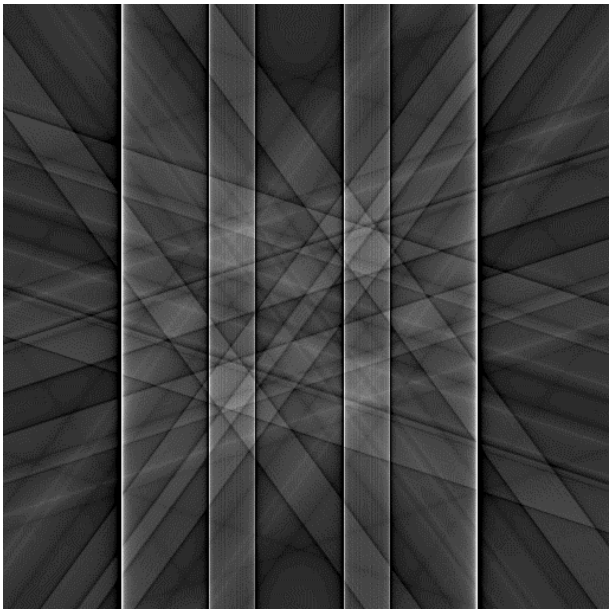

(b) $p = 10, \mathrm{RMSE} = 52.758$

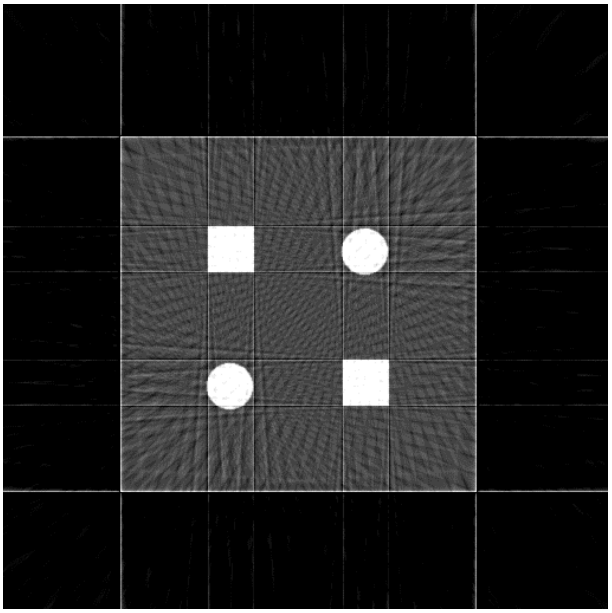

(c) $p = 100, \mathrm{RMSE} = 16.092$

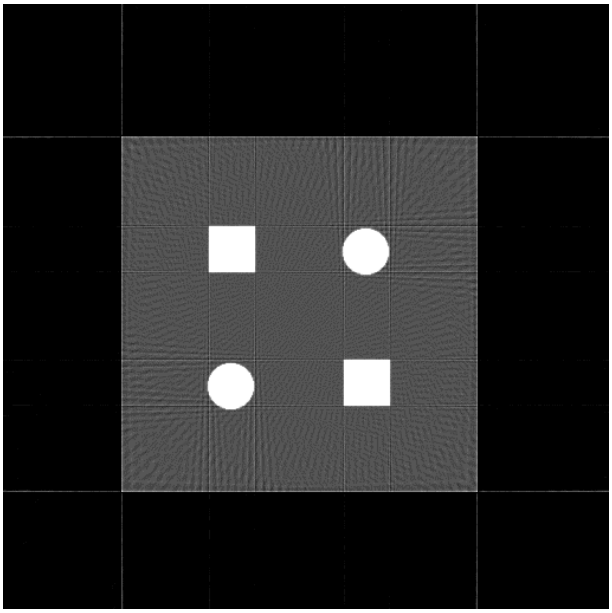

(d) $p = 200, \mathrm{RMSE} = 7.6674$

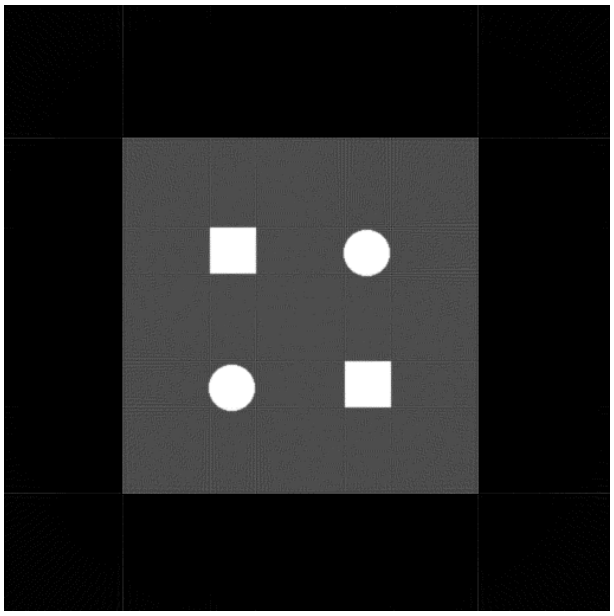

(e) $p = 400, \mathrm{RMSE} = 3.6279$

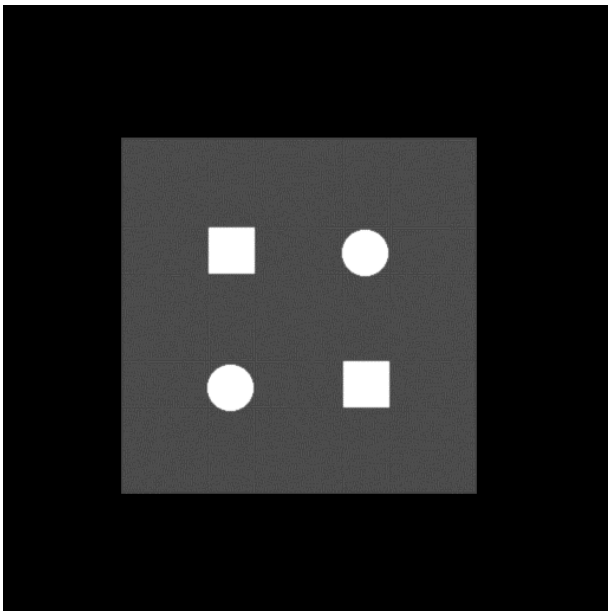

(f) $p = 800, \mathrm{RMSE} = 3.2295$

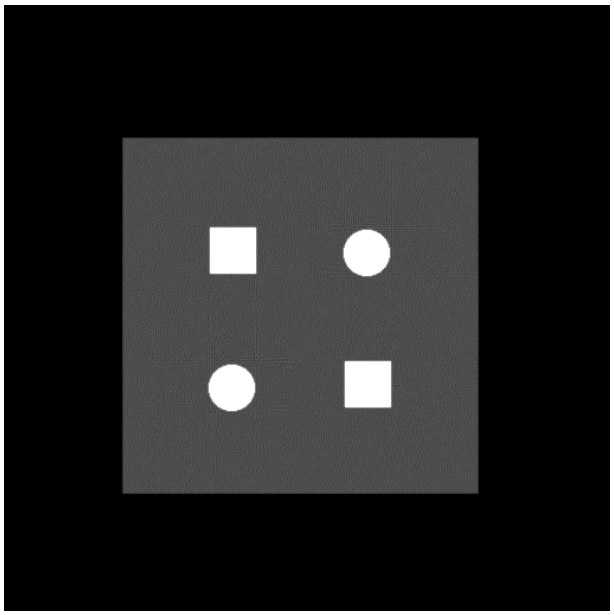

(g) $p = 1600, \mathrm{RMSE} = 2.6711$

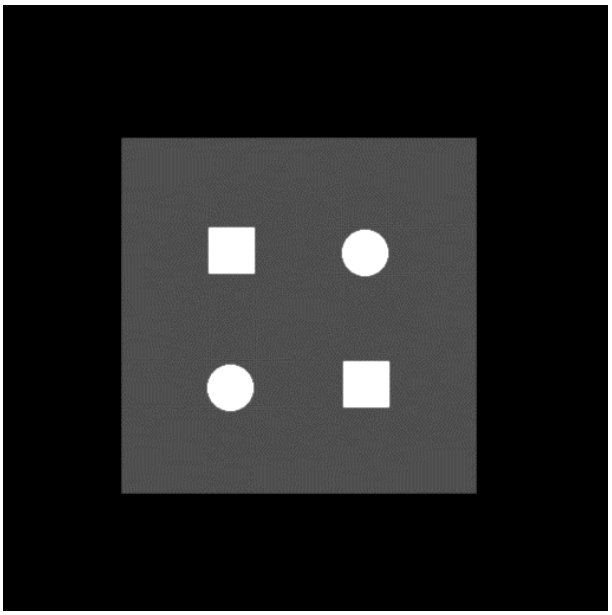

(h) $p = 3200, \mathrm{RMSE} = 2.5001$

Fig. A.2: The FBP results.

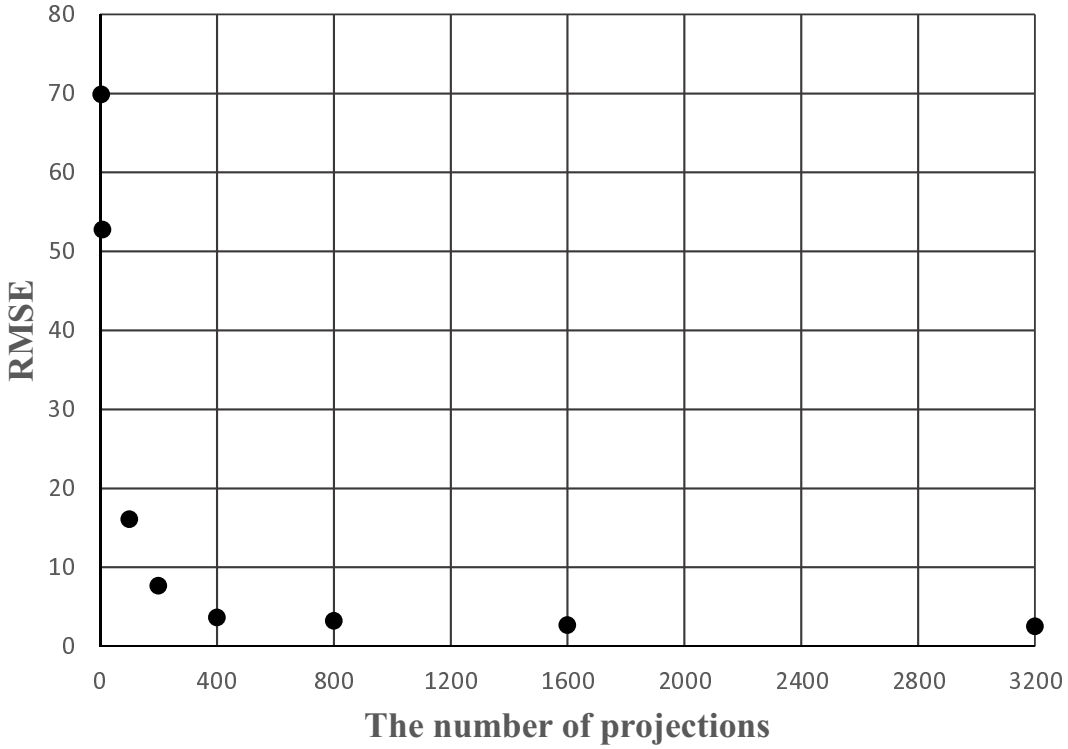

Fig. A.3: The relationship between projection numbers and RMSE.

Appendix B

Bilinear algorithm

In forward projection and back projection calculations, detector positions that pixels are projected are calculated. However, although the detector positions are represented by integer, the calculated positions usually are given by decimal. In such cases, the nearest neighbor algorithm or the bilinear algorithm are often used as a interpolation calculation. In this Appendix, these algorithms are introduced, and the importance is mentioned.

B.1 Nearest neighbor algorithm

In the nearest neighbor algorithm, when decimal coordinates are given, the decimal values will be rounded, and become integer (Fig. B.1). This means that one pixel is corresponding to one detector position. It is easy to code the nearest neighbor algorithm, but this algorithm involves quantization errors.

Fig. B.2 shows the FBP results to the numerical phantom shown in Fig. A.1 using the nearest neighbor algorithm. Fig. B.2 (a) shows the normal FBP result, and there are some moire-shaped artifacts. It seems a good result, and the RMSE value also shows a good value. However, when performing a windows adjustment to focus on objects that have low X-ray attenuation coefficients, the FBP result become Fig. B.2 (b). Artifacts caused by the nearest neighbor algorithm are emphasized, and such artifacts could make difficult to evaluate images. Next, as a solution of this problem, the bilinear algorithm is introduced.

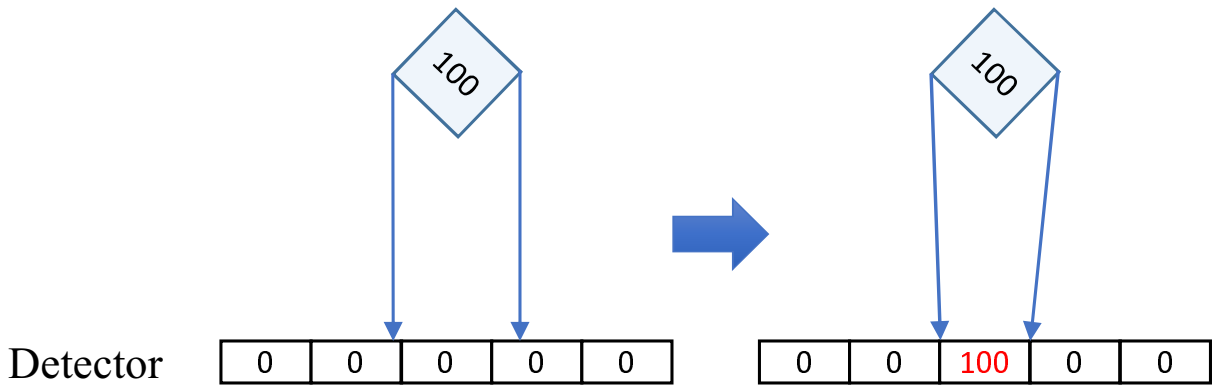

Fig. B.1: Nearest neighbor algorithm.

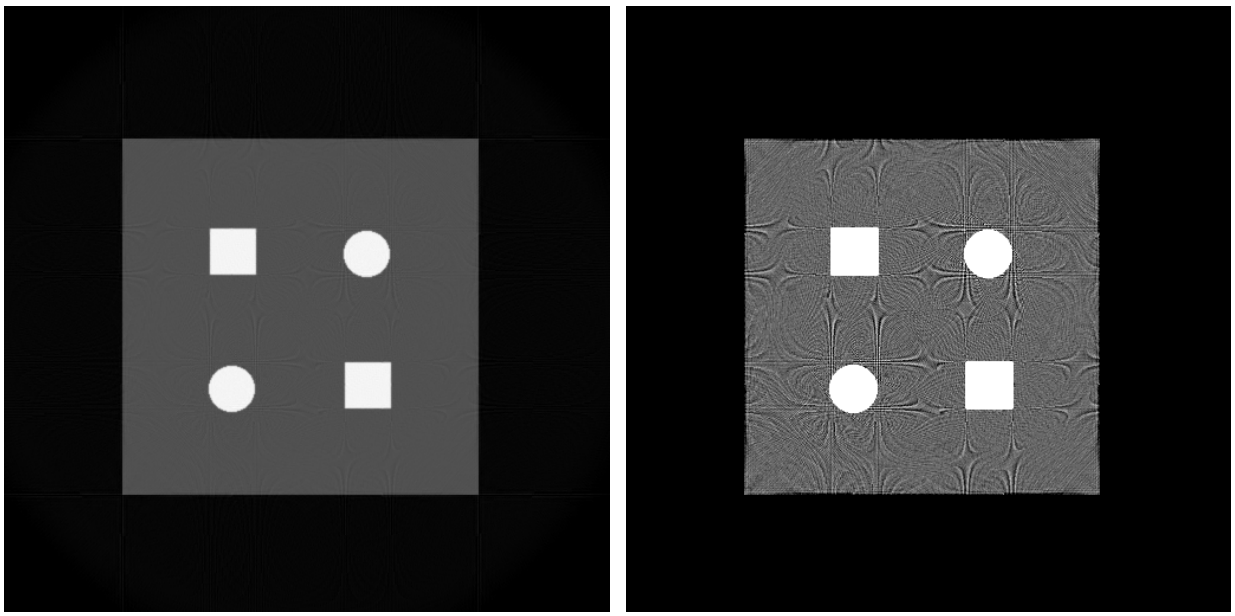

(a) RMSE = 3.7825 (b) RMSE = 20.227

Fig. B.2 The FBP results using the nearest neighbor algorithm. (a) is the normal FBP result, and (b) is the result of adjusting the focus on objects that have low X-ray attenuation coefficients.

B.2 Bilinear algorithm

In the bilinear algorithm, when decimal coordinates are given, the pixel will be divided into maximum three portions, and values weighted by the divided areas will be assigned to detectors (Fig. B.3). This way can generate more accurate reconstruction images than the nearest neighbor algorithm.

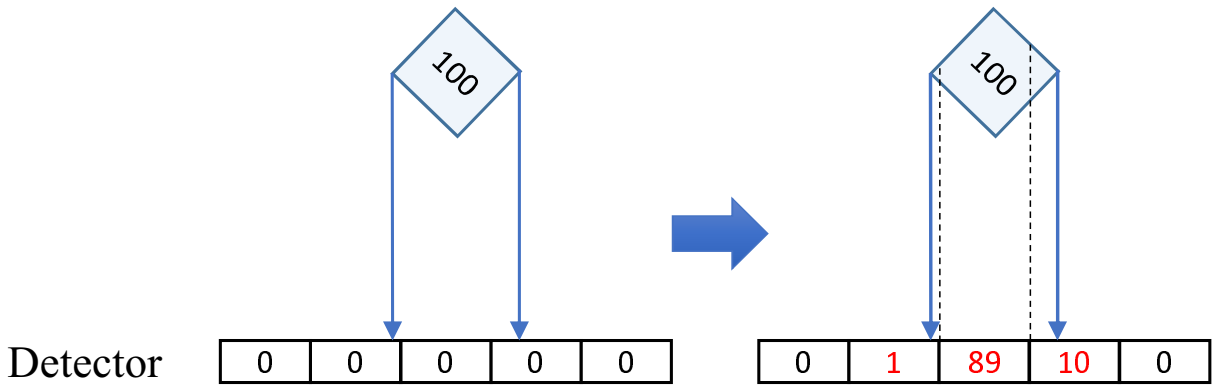

Fig. B.3: Bilinear algorithm.

Fig. B.4 shows the FBP results using the bilinear neighbor algorithm. Fig. B.4 (a) shows the normal FBP result, and there is almost no artifacts. When performing a windows adjustment to focus on objects that have low X-ray attenuation coefficients, the FBP result become Fig. B.3 (b). Although line-shaped artifacts are emphasized, the negative effect is obviously smaller than the result of the nearest neighbor algorithm. Therefore, the bilinear algorithm is applied to all calculation in this thesis except this appendix.

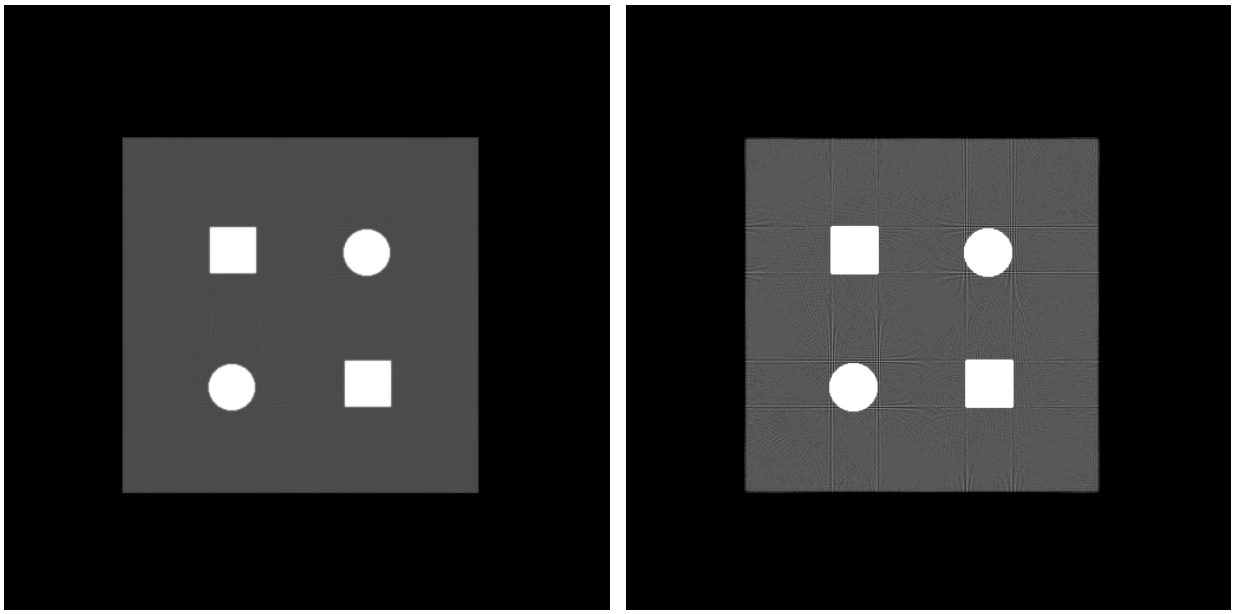

(a) RMSE = 3.2295 (b) RMSE = 11.433

Fig. B.4 The FBP results using the bilinear algorithm. (a) is the normal FBP result, and (b) is the result of adjusting the focus on objects that have low X-ray attenuation coefficients.

Appendix C

Derivation of FBP

In Chapter 2, the FBP method was introduced using intuitive description, however, theoretical explanations were insufficient. The reason why blurred images become improved by filtering on the two-dimensional Fourier plane will be mathematically demonstrated below.

When $M(u, v)$ is defined as a result of applying the two-dimensional Fourier transform to a cross-sectional image $\mu(x, y)$, by thinking that $\mu(x, y)$ is reproducible from $M(u, v)$ using the inverse Fourier transform, the following relationship is able to be derived.

$$\begin{aligned}\mu(x,y) &= \mathcal{F}^{-1}[M(u,v)] \\ &= \int_{-\infty}^{\infty}\left\{\int_{-\infty}^{\infty} M(u,v)\exp(2\pi iux)du\right\}\exp(2\pi ivy)dv \\ &= \int_{-\infty}^{\infty}\int_{-\infty}^{\infty} M(u,v)\exp(2\pi i(ux+vy))dudv. \end{aligned} \tag{C.1}$$

Consider deformations of this equation. First, when a surface integral on a uv plane is performed on a polar coordinate system, $dudv$ is rewritten as $Rdrd\theta$. Where R is a radius vector, and θ is a deflection angle. Here, the following relationships are established.

$$u = R\cos\theta \tag{C.2}$$

$$v = R\sin\theta \tag{C.3}$$

$$R = \sqrt{u^2+v^2}. \tag{C.4}$$

Therefore, Eqn. C.1 is able to be rewritten as the following:

$$\mu(x,y) = \int_0^{2\pi}\int_0^{\infty} M(u,v)\exp(2\pi i(Rx\cos\theta + Ry\sin\theta))\cdot RdRd\theta. \tag{C.5}$$

Also, when the one-dimensional Fourier transform is performed to projection data $p(r,\theta)$ from an angle θ about r, the result $P(R,\theta)$ becomes $M(R\cos\theta, R\sin\theta)$ by the projection-slice theorem. Thus, Eqn. C.5 is expressed as:

$$\mu(x,y) = \int_0^{2\pi} \left[\int_0^{\infty} P(R,\theta) \exp(2\pi i R(x\cos\theta + y\sin\theta)) \cdot R dR \right] d\theta. \tag{C.6}$$

In order to reduce the integral interval to $[0,\pi]$ of this equation, we divide it as the following:

$$\begin{aligned} \mu(x,y) &= \int_0^{\pi} \left[\int_0^{\infty} P(R,\theta) \exp(2\pi i R(x\cos\theta + y\sin\theta)) \cdot R dR \right] d\theta \\ &\quad + \int_{\pi}^{2\pi} \left[\int_0^{\infty} P(R,\theta+\pi) \exp(2\pi i R(x\cos\theta + y\sin\theta)) \cdot R dR \right] d\theta \end{aligned} \tag{C.7}$$

where by using the fact $r = x\cos\theta + y\sin\theta$,

$$\begin{aligned} \mu(x,y) &= \int_0^{\pi} \left[\int_0^{\infty} P(R,\theta) \exp(2\pi i R r) \cdot R dR \right] d\theta \\ &\quad + \int_0^{\pi} \left[\int_0^{\infty} P(R,\theta+\pi) \exp[2\pi i R(x\cos(\theta+\pi) + y\sin(\theta+\pi))] \cdot R dR \right] d\theta \\ &= \int_0^{\pi} \left[\int_0^{\infty} P(R,\theta) \exp(2\pi i R r) \cdot R dR \right] d\theta \\ &\quad + \int_0^{\pi} \left[\int_0^{\infty} P(R,\theta+\pi) \exp(-2\pi i R(x\cos\theta + y\sin\theta)) \cdot R dR \right] d\theta \\ &= \int_0^{\pi} \left[\int_0^{\infty} P(R,\theta) \exp(2\pi i R r) \cdot R dR \right] d\theta \\ &\quad + \int_0^{\pi} \left[\int_0^{\infty} P(R,\theta+\pi) \exp(-2\pi i R r) \cdot R dR \right] d\theta. \end{aligned} \tag{C.8}$$

Meanwhile, since projection data from a direction and an opposite direction are substantially the same,

$$P(R,\theta+\pi) = P(-R,\theta). \tag{C.9}$$

Therefore,

$$\begin{aligned} \mu(x,y) &= \int_0^{\pi} \left[\int_0^{\infty} P(R,\theta) \exp(2\pi i R r) \cdot R dR \right] d\theta \\ &\quad + \int_0^{\pi} \left[\int_0^{\infty} P(-R,\theta) \exp(-2\pi i R r) \cdot R dR \right] d\theta. \end{aligned} \tag{C.10}$$

Furthermore, by substituting -R for R on the second term of the right side, and flipping the

integration period,

$$\begin{aligned}
\mu(x,y) &= \int_0^{\pi}\left[\int_0^{\infty} P(R,\theta)\exp(2\pi iRr)\cdot RdR\right]d\theta \\
&\quad + \int_0^{\pi}\left[\int_0^{\infty} P(-(-R),\theta)\exp(-2\pi i(-R)r)\cdot(-R)\cdot(-dR)\right]d\theta \\
&= \int_0^{\pi}\left[\int_0^{\infty} P(R,\theta)\exp(2\pi iRr)\cdot RdR\right]d\theta \\
&\quad + \int_0^{\pi}\left[\int_{-\infty}^{0} P(R,\theta)\exp(2\pi iRr)\cdot(-R)dR\right]d\theta \\
&= \int_0^{\pi}\left[\int_{-\infty}^{\infty} \{P(R,\theta)\cdot|R|\}\exp(2\pi iRr)\cdot RdR\right]d\theta. \qquad \text{(C.11)}
\end{aligned}$$

Finally, we can see that the inside integral became the result of performing the inverse Fourier transform to $P(R,\theta)\cdot|R|$, and it is equivalent to the equation of FBP, which is introduced in Chapter 2.

Bibliography

[1] G. Hounsfield: Computerized transverse axial scanning (tomography), Part I. Description of system, Br. J. Radiol., **45**-552, 1016/1022 (1973)

[2] A.M. Cormak: Representation of a Function by Its Line Integrals, with Some Radiological Applications, Journal of Applied Physics, **34**-9, 2722/2727 (1963)

[3] A.M. Cormak: Representation of a Function by Its Line Integrals, with Some Radiological Applications. II, Journal of Applied Physics, **35**-10, 2908/2913 (1964)

[4] W.C. Röntgen: Üeber eine neue Art von Strahlen, Sitzb. Würzburger Phys. Med. Ges., **9**, 132/141 (1895)

[5] Centers for Disease Control and Prevention, Inpatient Surgery, http://www.cdc.gov/nchs/fastats/inpatient-surgery.htm (2015)

[6] S. Kim: Changes in surgical loads and economic burden of hip and knee replacements in the US: 1997-2004, Arthritis & Rheumatology, **59**-4, 481/488 (2008)

[7] S. Kurtz, K. Ong, E. Lau, F. Mowat and M. Halpern: Projections of primary and revision hip and knee arthroplasty in the United States from 2005 to 2030, J Bone Joint Surg Am, **89**-4, 780/785 (2007)

[8] F. Toyofuku and K. fukumori: Monochromatic X-ray CT Using Synchrotron Radiation (in Japanese), Japanese journal of Radiological Technology, **56**-6, 792/797 (2000)

[9] W.A. Kalender, R. Hebel and J. Ebersberger: Reduction of CT artifacts Caused by Metallic Implants, Radiology, **164**, 576/577 (1987)

[10] S. Zhao, K.T. Bae, B. Whiting and G. Wang: A wavelet method for metal artifact reduction with multiple metallic objects in the field of view, Journal of X-ray Science and Technology, **10**-1-2, 67/76 (2002)

[11] Y. Zhang, L. Zhang, X.R. Zhu, A.K. Lee, M. Chambers and L. Dong: Reducing metal artifacts in cone-beam CT images by preprocessing projection data, International Journal of Radiation Oncology Biology Physics, **67**-3, 924/932 (2007)

[12] M. Yazdi and L. Beaulieu: A novel approach for reducing metal artifacts due to metallic dental implants, IEEE Nuclear Science Symposium Conference Record, **4** 2260/2263 (2006)

[13] M. Abdoli, M. R. Ay, A. Ahmadian, R. A. Dierckx and H. Zaidi: Reduction of dental filling metallic artifacts in CT-based attenuation correction of PET data using weighted virtual sinograms optimized by a genetic algorithm, Medical Physics **37**-12 6166/6177 (2010)

[14] M. Koseki, S. Hashimoto, S. Sato, H. Kimura and N. Inou: CT Image Reconstruction Algorithm to Reduce Metal Artifact, Transactions of the Japan Society of Mechanical Engineers. A, **72**-724, 1888/1894 (2006)

[15] B. De Man, J. Nuyts, P. Dupont, G. Marchal and P. Suetens: An iterative maximum-likelihood polychromatic algorithm for CT, IEEE Transactions on Medical Imaging, **20**-10, 999/1008 (2001)

[16] G. Wang, T. Frei and M.W. Vannier: Fast iterative algorithm for metal artifact reduction in X-ray CT, Acad Radiol **7**, 607/614 (2000)

[17] R.E. Alvarez and A. Macovski: Energy-selective Reconstructions in X-ray Computerized Tomography, Physics in Medicine and Biology, **21**-5, 733/744 (1976)

[18] Y. Yamazaki and N. Toda: A Use of the Energy Information in X-Ray CT with an Asymmetric Filter (in Japanese), The IEICE transactions on information and systems (Japanese edition), **J99-D**-3, 956/966 (2007)

[19] F. Bamberg, A. Dierks, K. Nikolaou, M.F. Reiser, C.R. Becker and T.R. Johnson: Metal artifact reduction by dual energy computed tomography using monoenergetic extrapolation, Eur. Radiol., **21**-7, 1424/1429 (2011)

[20] P. Gilbert: Iterative methods for the three-dimensional reconstruction of an object from projections, Journal of Theoretical Biology, **36**-1, 105/117 (1972)

[21] Z. Wang, A. C. Bovik, H. R. Sheikh and E. P. Simincelli: Image quality assessment: from error visibility to structural similarity, IEEE Transactions on Image Processing, **13**-4, 600/612 (2004)

[22] R. Gordon, R. Bender and G.T. Herman: Algebraic Reconstruction Techniques (ART) for three-dimensional electron microscopy and X-ray photography, Journal of Theoretical Biology, **29**-3, 471/481 (1971)

[23] J. H. Hubbell and S. M. Seltzer, "Tables of X-Ray Mass Attenuation Coefficients and Mass Energy-Absorption Coefficients from 1 keV to 20 MeV for Elements Z = 1 to 92 and 48 Additional Substances of Dosimetric Interest," NIST, http://www.nist.gov/pml/data/ (2014)

Publications

Refereed Articles

[1] **T. Kano** and M. Koseki: Two Dimensional Metal Artifact Reduction Algorithm in CT and Its Application to Three Dimensional Data (in Japanese), Transactions of the Society of Instrument and Control Engineers, **50**-9, 633/639 (2014)

[2] **T. Kano** and M. Koseki: Metal Artifact Reduction using Iterative Reconstruction Algorithm (in Japanese), Transactions of the Society of Instrument and Control Engineers, **51**-12, 836-844 (2015)

Refereed Proceedings

[1] **T. Kano** and M. Koseki: CT Image Reconstruction Algorithm to Reduce Metal Artifact, IFMBE Proceedings **43**, 140/143, (2013)

Non-refereed publications

[1] **T. Kano** and M. Koseki: CT Image Reconstruction Algorithm to Reduce Metal Artifact (in Japanese), Proceedings of JSME Hokuriku Shin-etsu branch 40th Graduation Research Presentation, 1108(CD-ROM), (2011)

[2] **T. Kano** and M. Koseki: CT Image Reconstruction Algorithm to Reduce Metal Artifact (Metal Extraction and Non-Metal Interpolation of Sinogram) (in Japanese), Proceedings of SICE 28th Sensing Forum, 197/201, (2011)

[3] **T. Kano** and M. Koseki: Metal artifact reduction for individual stress analysis based on X-ray CT images (in Japanese), Proceedings of JSME Hokuriku Shin-etsu branch 40th General Meeting and Presentation, OS101419(USB), (2012)

[4] **T. Kano** and M. Koseki: A Study of X-ray CT Images Quality Improvement (Cone Beam CT Metal Artifact Reduction) (in Japanese), Proceedings of SICE 30th Sensing Forum, 11/15, (2013)

[5] **T. Kano** and M. Koseki: Metal Artifact Reduction using Iterative Reconstruction Algorithm (in Japanese), Proceedings of SICE 31th Sensing Forum, 181/186, (2014)

[6] **T. Kano** and M. Koseki: X-ray CT Metal Artifact Reduction for Accurate Non-destructive Inspection; ISF2014, Poster presentation, (2014) (in Japanese), Proceedings of SICE 52th Sensing Forum, 813(USB), (2015)

[7] **T. Kano** and M. Koseki: A three dimensional X-ray CT reconstruction algorithm using successive approximation (Application of metal artifact reduction) (in Japanese), Proceedings of SICE 32nd Sensing Forum, 319/324, (2015)

Acknowledgments

I gratefully acknowledge Dr Michihiko Koseki, Associate Professor of Shinshu University, for his guidance and support as a mentor. Without his persistent help this thesis would not have been possible. I also would like acknowledge valuable discussions with Dr. Pataky Todd Colin, Associate Professor of Shinshu University, Dr. Shunichi Kobayashi, Professor of Shinshu University, Mr. Kazuo Kikuchi and Mr. Takashi Tomitsuka of Com-scantecno Co., Ltd, and Dr. Tomohiro Iwashita of White Rabbit Co.